Electrostatic energy of a disordered system of metallic granules

D. A. Zakgeĭm,*) I. V. Rozhanskiĭ, and S. A. Gurevich
A. F. Ioffe Physicotechnical Institute, Russian Academy of Sciences, 194021 St. Petersburg, Russia

(Submitted 9 June 1999)
Pis'ma Zh. Éksp. Teor. Fiz. **70**, No. 2, 100–105 (25 July 1999)

Electrostatic interaction energies in a disordered monodisperse system of metallic granules are calculated. The calculation is performed in the dipole approximation for particles that cannot be regarded as point charges. The dependences of the charging energies of the particles on the concentration of the metallic phase as well as the dependences of the interaction energy of the charged particles on the distances between them are obtained. © *1999 American Institute of Physics.* [S0021-3640(99)00714-8]

PACS numbers: 41.20.Cv, 72.80.Tm, 81.05.Rm

A great deal of attention has been devoted in recent years to studying composite materials (or granular media) containing small metallic particles distributed randomly in a dielectric matrix. The description of the electric properties of such structures is based on the concept of charging energy, i.e., the electrostatic energy required to charge an individual metal particle with a certain charge Q, usually equal to the charge of a single electron. If this energy is high compared with the thermal energy kT, then it will determine the temperature and field dependences of the electric conductivity of a granular medium.[1–3]

To give a quantitative description of the conductivity it is necessary to determine the ground state of a system of metallic particles and to find the spectrum of its excitations involving transitions of electrons between particles.[2] In turn, this requires the matrix C_{ij}[4] of the capacitance and electrostatic inductance coefficients which relates the energy of the system with its charge state:

$$E=\frac{1}{2}\sum_{i,j} C_{ij}^{-1}Q_iQ_j\,. \tag{1}$$

To calculate the diagonal elements of this matrix (the capacitance coefficients) it is sufficient to calculate the charging energy E_{ci} of each particle in a neutral environment, while the off-diagonal elements (the electrostatic inductance coefficients) are determined from the charging energy V_{ij} of a pair of particles in a neutral environment.

In existing theoretical works the mean-field approximation[1] is ordinarily used to estimate the energies E_{ci} and V_{ij}, or the Coulomb interaction is calculated using formulas for point charges and an effective permittivity.[2,5] However, neither approximation is

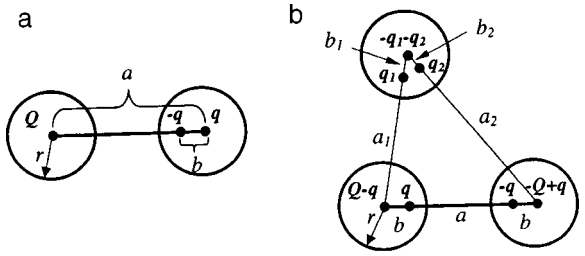

FIG. 1. Method of images for two (a) and three (b) spheres: $b=r^2/a$, $b_1=r^2/a_1$, $b_2=r^2/a_2$, $q=Qb/r$, $q_1=Qb_1/r$, and $q_2=Qb_2/r$.

adequately substantiated, specifically, the concept of effective permittivity itself is applicable only at distances that are large compared with the scale of nonuniformity of the medium. Moreover, both approaches completely ignore the rms deviation of E_{ci} and V_{ij} due to the randomness of the relative arrangement of the metallic particles in the medium.

In the present letter we endeavor to calculate more accurately the electrostatic interaction energies in a system of charged metallic particles in the case that the particle sizes are comparable to the interparticle distances, and therefore the particles cannot be regarded as point charges.

In the numerical model employed the granular medium is a collection of metallic spheres which have a fixed radius r and are randomly arranged in a fixed volume. The parameter of such an arrangement is the minimum admissible distance $\Delta_{\min}$ between neighboring spheres. The following method was used to implement the quasirandom arrangement numerically: Initially the spheres were arranged in a regular cubic lattice, after which an initial velocity was assigned to each sphere according to a random law and the motion of all spheres was calculated with their collisions taken into account. The effective radius of the spheres was taken to be $r^{\text{eff}}=r+\Delta_{\min}/2$. This guaranteed that the distance between the spheres cannot be less than $\Delta_{\min}$. In addition, all collisions were assumed to be completely inelastic, i.e., after each collision the velocity of a sphere was once again considered to be random. The calculation was terminated after each sphere had undergone a large number (several tens) of collisions, and the arrangement obtained was used later as a random realization.

In the zeroth approximation the charging energy of a metallic sphere is $E_{c0}=Q^2/2\epsilon r$, where Q is the charge on the sphere, r is the radius of the sphere, and ϵ is the permittivity of the surrounding medium. The coefficient $1/\epsilon r$ is the reciprocal C^{-1} of the electric capacitance of the sphere. In first order of the dipole expansion, the polarization of neutral spheres surrounding a given charge sphere must be taken into account. For this, we shall consider first the existing analytical solution of the problem of the interaction energy of two metallic spheres, of which one is charged to a charge Q while the other is neutral. To a first approximation we shall assume that the charge distribution in the charged sphere is uniform, and we shall construct the polarization of the neutral sphere by the method of images[4] (Fig. 1a). We shall calculate the electrostatic energy of such a system as the energy of the electric field in all space outside the spheres:

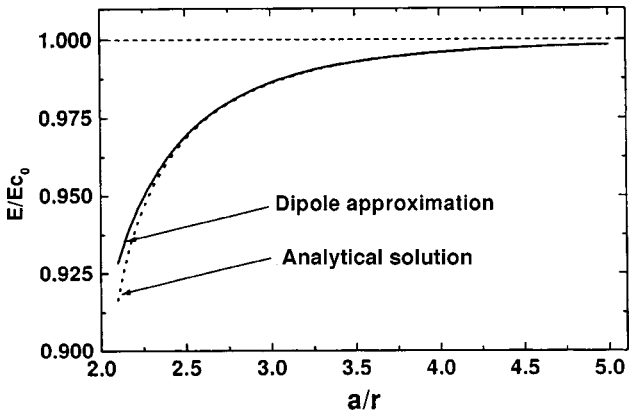

FIG. 2. Energy of a system of two spheres (charged and neutral), calculated in the dipole approximation (solid curve) and using to the exact analytical formula (dashed curve).

$$E = \int \frac{F(\mathbf{R})^2}{8\pi\epsilon} d^3\mathbf{R}, \tag{2}$$

where $F(\mathbf{R})$ is the electric field of the charges Q, q, and $-q$ in vacuum (see Fig. 1a). The integration in Eq. (2) was performed numerically by the Monte Carlo method, and the result was compared with the exact analytical solution (see, for example, Ref. 6). The result of this comparison is displayed in Fig. 2. It is evident from the figure that for intersphere distances $a > 2r + r/4$ the discrepancy between the first dipole approximation and the exact solution is less than 5%.

To find the total energy E_{ci} of a system of one charged sphere i in an environment of neutral spheres all pairwise dipole corrections to the energy of a charged sphere from each of the neutral spheres were calculated and summed. The dipole–dipole interaction of neutral spheres with one another was neglected, since it is of the next order of smallness. The calculations were performed for a system of 1000 spheres arranged by the method described above and averaged over all spheres located at distances greater than $L/4$, where L is the size of the system, from the boundaries of the system. In addition, averaging over 100 realizations of random arrangements was performed.

The average charging energy $\overline{E_c}$ computed in this manner is presented in Fig. 3 as a function of the density of metallic spheres for various values of the parameter $\Delta_{\min}$ of the random arrangement. The dashed curve shows the same dependence for spheres arranged in a simple cubic lattice. In addition, the same figure shows the curves of the rms deviation of E_c from the average value of $\overline{E_c}$ for the same parameters. The inset in Fig. 3 shows as an example the distribution of the charging energies of spheres for a particular case. It is evident that for sufficiently high densities of the metallic phase the rms deviation of the values of E_c can be a substantial fraction of the average value $\overline{E_c}$, and together with the random potential[2] it serves as a source of diagonal disorder in the granular medium.

To calculate in the same approximation the energy of a system of two charged spheres surrounded by neutral spheres, it is necessary to find in the dipole approximation

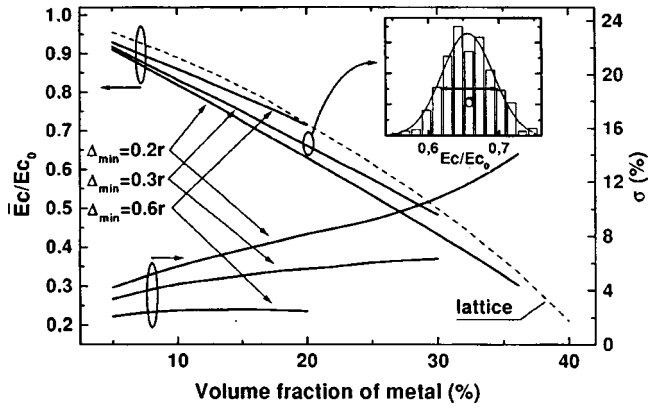

FIG. 3. Average charging energy of a sphere and its rms deviation σ as a function of the concentration of the metallic phase for various values of the parameter $\Delta_{\min}$ of the arrangement and for a cubic lattice of granules (dashed curve).

the energy of a system of three spheres, one of which is neutral while the two others are charged, for example, with charges Q and $-Q$. Just as in preceding analysis, we shall use the method of images (Fig. 1b) to take account of the polarization of the spheres, and we shall calculate the energy of such a system using Eq. (2), where the integration extends over the entire space outside all three spheres. Subtracting from the energy obtained in this manner the energy of a system consisting of two isolated charged spheres (setting $q_1=0$, $q_2=0$), we obtain a correction due to the polarization of a neutral sphere. To calculate the total energy of a system consisting of two charged spheres in an environment of neutral spheres, we shall sum the corrections due to all neutral spheres, once again neglecting the dipole–dipole interaction of the neutral spheres with one another.

The dependence of the interaction energy of charged spheres, computed in this manner, on the intersphere distance is presented in Fig. 4 for the cases of attraction (charges with different signs) and (charges with like signs). The curves presented in the figure were averaged just as in the case of the charging energies.

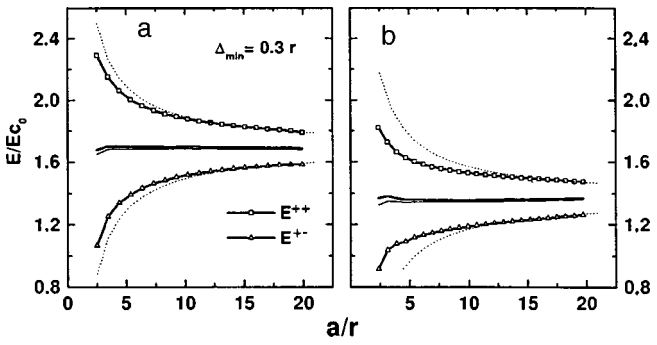

FIG. 4. Electrostatic energy of a system of two charged spheres with charges with the same (E^{++}) and different (E^{+-}) signs surrounded by neutral spheres as a function of the intersphere distance for volume concentrations of the metallic phase 10% (a) and 20% (b).

The elements of the inverse matrix C_{ij}^{-1} can be obtained from the charging energies of an arbitrary pair of spheres i and j with charges of like (E^{++}) or different (E^{+-}) signs according to the formulas[4]

$$E^{++}=\left(\frac{C_{ii}^{-1}}{2}+\frac{C_{jj}^{-1}}{2}+C_{ij}^{-1}\right)Q^2 \quad \text{and} \quad E^{+-}=\left(\frac{C_{ii}^{-1}}{2}+\frac{C_{jj}^{-1}}{2}-C_{ij}^{-1}\right)Q^2, \tag{3}$$

while the half sum of the energies E^{++} and E^{+-} should equal the sum of the charging energies of the spheres i and j. Thus we can calculate the same quantity — the sum of charging energies (or the diagonal elements of the inverse matrix of capacitance coefficients) — for any pair of spheres by two independent methods. The computational accuracy can be estimated by comparing the results of these calculations. The thick solid line in Fig. 4 shows the half sum $(E^{++}+E^{+-})/2$ and the fine line shows the half sum $(E_{ci}+E_{cj})/2$ of the charging energies. As one can see from the figure, the discrepancy between these curves is $\sim 1\%$ for a 10% concentration and $\sim 2\%$ for a 20% concentration. In order of magnitude this discrepancy is the maximum accuracy that can be obtained in the dipole approximation. As the concentration of spheres increases, this accuracy decreases, because on the average more spheres are located at a short distance from one another, where the error of the dipole approximation is large (see Fig. 2).

The dashed curves in Fig. 4 the distance dependence of the average energy of a system of two charged spheres for the case that the electrostatic interaction of these spheres is treated as the interaction of point charges:

$$V^{\text{point}}=2E_{c0}\left(\frac{\overline{E_c}}{E_{c0}}\pm\frac{1}{a}\right). \tag{4}$$

It is evident that for sufficiently large intersphere distances ($a>15\cdot r$) expression (4) describes the computed dependences well. An important feature of the asymptotic expression (4) is that the part describing the intersphere interaction does not contain a concentration-dependent effective permittivity, i.e., the Coulomb interaction at large distances drops off just as in a pure dielectric with no metallic inclusions.

In summary, in the present letter we have obtained the dependence of the basic electrostatic energy parameters of a disordered granular medium on the concentration of the metallic phase. The calculation was performed in the dipole approximation neglecting the dipole–dipole interaction. The energy parameters, such as the charging energy of an individual granule and the electrostatic interaction energy of a pair of charged granules, obtained make it possible to find the matrix of capacitances and electrostatic inductances of the system, which in turn makes it possible to determine the electrostatic energy of an arbitrary distribution of charges over the granules using Eq. (1).

The computational results showed that the average charging energy of a granule for a fixed concentration of the metallic phase depends on the geometric parameters of the distribution of granules in the dielectric matrix and that for sufficiently high concentrations the rms deviation of this energy can be several tens of percent of its magnitude. It was also shown that the Coulomb interaction between two charged granules at large distances is insensitive to the existence of the other granules and thereby does not depend

on the concentration of the metallic phase. However, at short distances the Coulomb interaction is screened, the screening being progressively stronger the higher the concentration of the metallic phase.

We thank the Russian Fund for Fundamental Research (Grant 98-02-18210), the program ''Physics of Solid-State Nanostructures'' of the Ministry of Science of the Russian Federation (Grants 97-2014 and 97-1035), and the European Research Office of the US Army under Contract 68171-98-M-5654 for financial support.

*)e-mail: mitya@quantum.ioffe.rssi.ru

[1] B. Abeles, P. Sheng, M. D. Coutts, and Y. Arie, Adv. Phys. **24**, 407 (1975).
[2] E. Cuevas, M. Ortuno, J. Ruiz, Phys. Rev. Lett. **71**, 1871 (1993).
[3] P. Sheng, Philos. Mag. B **65**, 357 (1992).
[4] L. D. Landau and E. M. Lifshitz, *Electrodynamics of Continuous Media* (Pergamon Press, New York) [Russian original, Nauka, Moscow, 1982].
[5] L. C. Shen, C. Liu, J. Korringa, and K. J. Dunn, J. Appl. Phys. **67**, 7071 (1990).
[6] V. V. Batygin and I. N. Toptygin, *Problems in Electrodynamics* (Academic Press, London, 1964) [cited Russian original, Nauka, Moscow, 1970, p. 53].

Translated by M. E. Alferieff

Two energy scales and breakdown of renormalizability in the Kondo problem

Yu. N. Ovchinnikov and A. M. Dyugaev

Max Planck Institute for Physics of Complex Systems, D-01187 Dresden, Germany; L. D. Landau Institute of Theoretical Physics, Russian Academy of Sciences, 117940 Moscow, Russia

(Submitted 10 June 1999)
Pis'ma Zh. Éksp. Teor. Fiz. **70**, No. 2, 106–111 (25 July 1999)

It is shown that a second energy scale $T_0 \gg T_k$ arises in the Kondo problem. Perturbation theory is valid only in the region $T > T_0$. For this reason, the transition from weak to strong coupling occurs at temperatures much higher than the Kondo temperature T_k. © *1999 American Institute of Physics.* [S0021-3640(99)00814-2]

PACS numbers: 75.20.Hr, 72.10.Fk, 72.15.Qm

In investigations of the Kondo problem it is ordinarily assumed that there is only one energy scale and that the theory is renormalizable.[1–3] Investigation of the dependence of the average electron spin of an impurity atom at $T=0$ as a function of the magnetic field strength[4] has shown that perturbation theory is inapplicable even for strong magnetic fields $\mu H > T_k$, where μ is the Bohr magneton and T_k is the Kondo temperature. For this reason it is a good idea that the hypothesis that there is only one energy scale and the renormalizability of the exchange interaction be checked using finite-temperature perturbation theory. The investigation is complicated by the fact that, as will be shown below, in the Kondo problem the free energy F is not a sum of irreducible diagrams.

We shall assume that the interaction of a magnetic impurity with the conduction electrons is described by the exchange Hamiltonian

$$\hat{H} = \hat{H}_0 + \int d^3r_1 d^3r_2 V(r_1 - r_2) \chi_\alpha^+(r_1) \varphi_\beta^+(r_2) \chi_\beta(r_2) \varphi_\alpha(r_1) - \frac{\mu H}{2} \int (\varphi_\uparrow^+(r_1)\varphi_\uparrow(r_1) - \varphi_\downarrow^+(r_1)\varphi_\downarrow(r_1)) d^3r_1. \tag{1}$$

Here the operators φ_α^+ and χ_α^+ create an electron in a state localized on an impurity and in the continuous spectrum, respectively. The partition function Z at finite temperature can be written as[5]

$$Z = \mathrm{Tr}\exp(-\hat{H}/T) = \mathrm{Tr}\left\{ e^{-\hat{H}_0/T}\left[1 - \int_0^{1/T} d\tau\, \hat{V}(\tau) + \int_0^{1/T} d\tau_1 \int_0^{\tau_1} d\tau_2 \hat{V}(\tau_1)\hat{V}(\tau_2) - \ldots \right] \right\}, \tag{2}$$

where

$$\hat{V}(\tau)=e^{\hat{H}_0\tau}V(r)e^{-\hat{H}_0\tau}. \tag{3}$$

We shall employ the symmetric model to cut off the matrix elements with cutoff energy D.[3] For $T=0$ we showed that the dependence of the ground-state energy on the magnetic field strength is insensitive to the form of the cutoff. In perturbation theory there arises the quantity

$$\Phi(\tau)=\sum_k (1-n_k)e^{-\tau\varepsilon_k}=\int_{-D}^{D} d\xi\, e^{-\tau\xi}\left(1-\frac{1}{1+\exp(\xi/T)}\right), \tag{4}$$

where n_k is the Fermi distribution function of the electrons, and the energy ε_k is measured from the Fermi surface. It is easy to verify that

$$\sum_k n_k e^{\tau\varepsilon_k}=\int_{-D}^{D} d\xi\, e^{\tau\xi}(1+\exp(\xi/T))^{-1}=\Phi(\tau). \tag{5}$$

The function $\Phi(\tau)$ satisfies

$$\Phi(\tau)=\Phi(1/T-\tau). \tag{6}$$

Equations (4), (5), and (6) greatly simplify the calculation of the perturbation series. From Eqs. (4) and (5) we find

$$\Phi(\tau)=\frac{1}{\tau}(1-e^{-D\tau})+\left(\frac{1-e^{-D(1/T-\tau)}}{1/T-\tau}-\frac{1}{1/T+\tau}\right)-2\tau\sum_{n=2}^{\infty}\frac{(-)^n}{(n/T)^2-\tau^2}. \tag{7}$$

It is easy to check that near a singularity ($\tau T\ll 1$) the function $\Phi(\tau)$ can be represented as

$$\Phi(\tau)=\frac{1}{\tau}(1-e^{-D\tau})+\frac{\pi^2}{6}T^2\tau+0(T(T\tau)^3). \tag{8}$$

In the second order of perturbation theory we find from Eqs. (2), (4), and (5)

$$Z_2=Z_0^eZ_0^ig^2(J_0+J_H), \tag{9}$$

where

$$J_H=\int_0^{1/T}d\tau_1\int_0^{\tau_1}\Phi^2(\tau_1-\tau_2)\frac{\exp(-\mu H(\tau_1-\tau_2))+\exp(-\mu H/T+\mu H(\tau_1-\tau_2))}{1+e^{-\mu H/T}}, \tag{10}$$

$J_0=J_{H=0}$, $Z_0^i=2\cosh(\mu H/2T)$, and Z_0^e is the partition function of a free electron gas. In Eq. (9) g is a dimensionless coupling constant, defined by the relation

$$\sum_k \langle V\rangle(\ldots)\to g\int_{-D}^{D} d\xi(\ldots).$$

Expression (9) and (10) are identical to the results of Ref. 3.

In the third order of perturbation theory the expression for the partition function is still quite simple

$$Z_3 = -Z_0^e Z_0^i g^3 \int_0^{1/T} d\tau_1 \int_0^{\tau_1} d\tau_2 \int_0^{\tau_2} d\tau_3 \Phi(\tau_1-\tau_2)\Phi(\tau_2-\tau_3)\Phi(\tau_1-\tau_3)$$
$$\times\{\mathcal{N}(\tau_1-\tau_2)+\mathcal{N}(\tau_2-\tau_3)+\mathcal{N}(\tau_1-\tau_3)\}, \quad (11)$$

where

$$\mathcal{N}(\tau) = \frac{e^{-\mu H\tau} + e^{-\frac{\mu H}{T}+\mu H\tau}}{1+e^{-\mu H/T}}.$$

The fourth-order terms lead to the appearance of a second energy scale in the Kondo problem. For this reason, we present the complete expression for the fourth-order correction Z_4:

$$Z_4 = Z_0^e Z_0^i g^4 \Bigg\{ \frac{1}{2}(J_0+J_H)^2 + \int_0^{1/T} d\tau_1 \int_0^{\tau_1} d\tau_2 \int_0^{\tau_2} d\tau_3 \int_0^{\tau_3} d\tau_4$$
$$\times[\Phi^2(\tau_1-\tau_2)\Phi^2(\tau_3-\tau_4)(\mathcal{N}((\tau_1-\tau_2)+(\tau_3-\tau_4))-\mathcal{N}(\tau_1-\tau_2)\mathcal{N}(\tau_3-\tau_4))$$
$$+\Phi^2(\tau_1-\tau_4)\Phi^2(\tau_2-\tau_3)(\mathcal{N}((\tau_1-\tau_2)+(\tau_3-\tau_4))-\mathcal{N}(\tau_1-\tau_4)\mathcal{N}(\tau_2-\tau_3))$$
$$-\Phi^2(\tau_1-\tau_3)\Phi^2(\tau_2-\tau_4)(\mathcal{N}(\tau_1-\tau_3)+\mathcal{N}(\tau_2-\tau_4))+\mathcal{N}(\tau_1-\tau_3)\mathcal{N}(\tau_2-\tau_4))\Big]$$
$$+\int_0^{1/T} d\tau_1 \int_0^{\tau_1} d\tau_2 \int_0^{\tau_2} d\tau_3 \int_0^{\tau_3} d\tau_4[\Phi(\tau_1-\tau_4)\Phi(\tau_3-\tau_4)\Phi(\tau_2-\tau_3)\Phi(\tau_1-\tau_2)$$
$$\times(2+2\mathcal{N}((\tau_1-\tau_2)+(\tau_3-\tau_4))+\mathcal{N}(\tau_1-\tau_2)+\mathcal{N}(\tau_1-\tau_4)+\mathcal{N}(\tau_2-\tau_4)+\mathcal{N}$$
$$\times(\tau_3-\tau_4)+\mathcal{N}(\tau_1-\tau_3)+\mathcal{N}(\tau_2-\tau_3))-\Phi(\tau_2-\tau_4)\Phi(\tau_3-\tau_4)\Phi(\tau_1-\tau_3)\Phi(\tau_1-\tau_2)$$
$$\times(2+\mathcal{N}(\tau_1-\tau_2)+\mathcal{N}(\tau_3-\tau_4))-\Phi(\tau_1-\tau_4)\Phi(\tau_2-\tau_4)\Phi(\tau_2-\tau_3)\Phi(\tau_1-\tau_3)$$
$$\times(2+\mathcal{N}(\tau_1-\tau_4)+\mathcal{N}(\tau_2-\tau_3))]\Bigg\}. \quad (12)$$

Expressions (9), (11), and (12) make it possible to find the correction arising to the free energy as a result of the interaction. It contains a large term that is proportional to the cutoff energy D and depends on the interaction constant g. Ordinarily, this contribution is treated as a shift δE of the ground-state energy and it is assumed to be temperature-independent to all orders in the coupling constant g. Then the quantity δE so determined should be identical to all orders in g (for the same cutoff) to the shift $\delta\tilde{E}$ of the ground state and found at $T=0$.

We shall now show that this identity occurs only in second and third orders in the coupling constant g. A difference arises in fourth order, leading to a second energy scale in the Kondo problem.

From Eqs. (9), (11), and (12) we find

$$-\delta E = D\left\{ g^2 4\ln 2 - 3g^3 \int_0^\infty \frac{dx}{x} \int_0^x \frac{dy(1-e^{-x})(1-e^{-y})(1-e^{-(x-y)})}{y(x-y)} \right.$$
$$+ g^4 \left[6\int_0^\infty dxdydz \frac{(1-e^{-x})(1-e^{-y})(1-e^{-z})(1-e^{-(x+y+z)})}{xyz(x+y+z)} \right.$$
$$\left.\left. - 3\int_0^\infty dxdydz \frac{(1-e^{-(x+y)})^2(1-e^{-(y+z)})^2}{(x+y)^2(y+z)^2} \right] \right\}. \quad (13)$$

The quantity $\delta\tilde{E}$ was found in Ref. 4. Using the results of Ref. 4 (see Appendix C), we write the expression for $\delta\tilde{E}$ in the form

$$-\delta\tilde{E} = D\left\{ g^2 4\ln 2 - 3g^3 \int_0^1 \frac{d\xi_1 d\xi_2 d\xi_3}{(\xi_1+\xi_2)(\xi_1+\xi_3)} \right.$$
$$+ g^4 \int_0^1 d\xi_1 d\xi_2 d\xi_3 d\xi_4 \left[\frac{10}{(\xi_1+\xi_2)(\xi_1+\xi_3)(\xi_1+\xi_4)} - \frac{4}{(\xi_1+\xi_2)(\xi_1+\xi_3)(\xi_3+\xi_4)} \right.$$
$$\left.\left. - \frac{4}{(\xi_1+\xi_2)(\xi_1+\xi_3)(\xi_1+\xi_2+\xi_3+\xi_4)} + \frac{1}{(\xi_1+\xi_2)(\xi_3+\xi_4)(\xi_1+\xi_2+\xi_3+\xi_4)} \right] \right\}. \quad (14)$$

Next, we find from Eqs. (13) and (14)

$$\int_0^1 \frac{d\xi_1 d\xi_2 d\xi_3}{(\xi_1+\xi_2)(\xi_1+\xi_3)} = 2\ln^2 2 + \frac{\pi^2}{6};$$

$$\int_0^\infty \frac{dx}{x} \int_0^x \frac{dy}{y} \frac{(1-e^{-x})(1-e^{-y})(1-e^{-(x-y)})}{x-y} = \frac{\pi^2}{6} + \left(\frac{\pi^2}{3} - 4\sum_{n=1}^\infty \frac{1}{2^n n^2} \right). \quad (15)$$

Since

$$\frac{\pi^2}{3} - 4\sum_{n=1}^\infty \frac{1}{2^n n^2} = 2\ln^2 2, \quad (16)$$

the expressions for δE and $\delta\tilde{E}$ are identical in the second and third orders of perturbation theory. In fourth order we find from Eqs. (13) and (14)

$$-(\delta\tilde{E} - \delta E) = 4g^4 D \int_0^1 d\xi_1 d\xi_2 d\xi_3 d\xi_4 \left\{ \frac{1}{(\xi_1+\xi_2)(\xi_1+\xi_3)(\xi_1+\xi_4)} \right.$$
$$- \frac{1}{(\xi_1+\xi_2)(\xi_1+\xi_3)(\xi_3+\xi_4)} - \frac{1}{(\xi_1+\xi_2)(\xi_1+\xi_3)(\xi_1+\xi_2+\xi_3+\xi_4)}$$
$$\left. + \frac{1}{(\xi_1+\xi_2)(\xi_3+\xi_4)(\xi_1+\xi_2+\xi_3+\xi_4)} \right\}. \quad (17)$$

Using the relation

$$\int_0^1 \frac{d\xi_1 d\xi_2 d\xi_3 d\xi_4}{(\xi_1+\xi_2)(\xi_1+\xi_3)(\xi_1+\xi_2+\xi_2+\xi_3+\xi_4)} = \frac{1}{2}\int_0^1 \frac{d\xi_1 d\xi_2 d\xi_3 d\xi_4}{(\xi_1+\xi_3)(\xi_1+\xi_2)(\xi_3+\xi_4)}, \tag{18}$$

we write expression (16) for the energy difference $(\delta\tilde{E}-\delta E)$ in the form

$$-(\delta\tilde{E}-\delta E) = 4g^4 D\left\{ \int_0^1 dx \ln^3\left(\frac{1+x}{x}\right) - \frac{3}{2}\int_0^1 dxdy \frac{\ln\left(\frac{1+x}{x}\right)\ln\left(\frac{1+y}{y}\right)}{x+y} + I \right\}, \tag{19}$$

where the integral I is determined by the expression

$$I = \int_0^1 \frac{d\xi_1 d\xi_2 d\xi_3 d\xi_4}{(\xi_1+\xi_2)(\xi_3+\xi_4)(\xi_1+\xi_2+\xi_2+\xi_3+\xi_4)} = 40\ln 2 - 24\ln 3 + 2\sum_{n=1}^{\infty}\frac{1}{n^2 2^{2n}}. \tag{20}$$

It is convenient to calculate the two remaining integrals in Eq. (19) together. Simple transformations yield

$$\int_0^1 dx \ln^3\left(\frac{1+x}{x}\right) - \frac{3}{2}\int_0^1 \frac{dxdy}{x+y}\ln\left(\frac{1+x}{x}\right)\ln\left(\frac{1+y}{y}\right)$$

$$= \ln^3 2 - 6\int_2^{\infty}\frac{dx\ln x\ln(x/2)}{x(x-1)(x-2)} = -2\ln^3 2 - 6\left(\zeta(3) - 2\sum_{n=1}^{\infty}\frac{1}{2^n n^3}\right), \tag{21}$$

where $\zeta(x)$ is the Riemann zeta function.

Substituting expressions (20) and (21) into Eq. (19) we find

$$-(\delta\tilde{E}-\delta E) = 4g^4 D\left\{ 40\ln 2 - 24\ln 3 + 2\sum_{n=1}^{\infty}\frac{1}{n^2 2^{2n}} - 2\ln^3 2 \right.$$

$$\left. - 6\left(\zeta(3) - 2\sum_{n=1}^{\infty}\frac{1}{2^n n^3}\right)\right\} = g^4 D\cdot 3.8506. \tag{22}$$

The fact that the right-hand side of Eq. (22) is nonzero signifies that a second characteristic energy scale T_0, such that $T_k \ll T_0 \ll \epsilon_F$, exists in the Kondo problem. To determine this scale it is necessary to investigate the higher-order terms of the perturbation theory. In zero magnetic field the anomalous terms appear only in the eighth order of perturbation theory and lead to a correction δF to the free energy as

$$\delta F = 24JDg^8\int_0^{\infty} dxdydz \frac{I_1(y+z)I_1(x+z)}{(x+y+z)^2}(1-e^{-(x+y+z)})^2, \tag{23}$$

where the integral $I_1(a)$ is determined by the expression

$$I_1(a) = \int_a^{\infty}\frac{dx(1-e^{-x})^2}{x^2}. \tag{24}$$

In order of magnitude one has

$$\delta F \sim g^8 D^2/T. \tag{25}$$

A comparison of the corrections to the specific heat from the fourth-order terms determined by Eq. (23) and the eighth-order terms in Eq. (25) shows that in order of magnitude the second characteristic energy scale T_0 in the Kondo problem is

$$T_0 \sim g^2 D. \tag{26}$$

This value of T_0 is identical to the expression obtained in Ref. 6 in the self-consistent field approximation.

The quantity $\mathcal{N}(\tau)$ in the expression for the partition function can appear in no more than one cofactor in any order of perturbation theory. This property is due to the fact that only one electron is always present in a localized state. Nonetheless, in a magnetic field the anomalous terms appear in the free energy likewise only in eighth order in the coupling constant g. Apparently, the point T_0 is a crossover from perturbation theory to strong coupling. The perturbation theory holds only in the range $T \gg T_0$. Strong coupling obtains in the range $T \ll T_0$.

We thank Professor P. Fulde for valuable remarks and support of this work.

[1] A. A. Abrikosov and A. A. Migdal, J. Low Temp. Phys. **3**, 519 (1970).
[2] A. M. Tsvelick and P. B. Wigmann, Adv. Phys. **32**, 453 (1983).
[3] N. Andrei, K. Furuya, and J. H. Lowenstein, Rev. Mod. Phys. **55**, 331 (1983).
[4] Yu. N. Ovchinnikov and A. M. Dyugaev, Zh. Éksp. Teor. Fiz. **115**, 1263 (1999) [JETP **88**, 696 (1999)].
[5] A. A. Abrikosov, L. P. Gor'kov, and I. E. Dzyaloshinskiĭ, *Methods of Quantum Field Theory in Statistical Physics* (Prentice-Hall, Englewood Cliffs, N. J., 1963).
[6] Yu. N. Ovchinnikov, A. M. Dyugaev, P. Fulde, and V. Z. Kresin JETP Lett. **66**, 195 (1997).

Translated by M. E. Alferieff

Transformation of quantum size levels into virtual levels at the boundary between *p*-GaAs and an AlAs/GaAs superlattice

V. L. Al'perovich,*) B. A. Tkachenko, and O. A. Tkachenko
Institute of Semiconductor Physics, Siberian Branch of the Russian Academy of Sciences, 630090 Novosibirsk, Russia; Novosibirsk State University, 630090 Novosibirsk, Russia

N. T. Moshegov, A. I. Toropov, and A. S. Yaroshevich
Institute of Semiconductor Physics, Siberian Branch of the Russian Academy of Sciences, 630090 Novosibirsk, Russia

(Submitted 20 May 1999; resubmitted 15 June 1999)
Pis'ma Zh. Éksp. Teor. Fiz. **70**, No. 2, 112–117 (25 July 1999)

The transformation of quantum size levels into virtual levels upon a change in the electric field in an AlAs/GaAs superlattice located in the *i* region of a *p*–*i*–*n* structure is studied experimentally and theoretically. It is shown that an interfacial state at the boundary between the superlattice and the *p*-GaAs contact layer results in a resonant increase in the probability of photoelectron tunneling from the contact into the superlattice via Wannier–Stark levels. © *1999 American Institute of Physics.* [S0021-3640(99)00914-7]

PACS numbers: 73.61.Ey, 73.40.Kp, 73.20.Dx

It is well known that when a discrete level in a potential well approaches the bottom of the continuum and transforms into a virtual level, resonant quantum scattering of slow particles occurs.[1] The cross section for scattering by a spherical well approaches infinity, and according to Levinson's theorem the scattering phase changes by π. Conversely, a symmetric one-dimensional well becomes completely transparent when a discrete level transforms into a virtual level (one-dimensional Ramsauer effect).[2] A virtual level has been observed in the scattering of a neutron by a proton with antiparallel spins, and a discrete resonance level of a deuteron has been observed in scattering of the same particles with parallel spins.[1] However, the transformation of a discrete resonance into a virtual level upon a continuous variation of the parameters of a potential well has still not been observed. In contrast to atomic and nuclear physics the parameters of potential wells and barriers can be easily controlled in semiconductor microstructures and superlattices. Fine tuning of the electronic spectrum of semiconductor superlattices by varying the thickness and the composition of individual layers during epitaxy as well as the strength of the electric field has made it possible to observe a number of phenomena, which have long been predicted theoretically but have never been observed experimentally in ordinary crystals. Specifically, Wannier–Stark localization processes in an electric field[3,4] and delocalization of electronic states on account of resonant Zener tunneling between Stark

states, originating from different minibands,[5,6] have been studied experimentally in semiconductor superlattices. Edge states,[7] predicted by Tamm for ideal crystals,[8] have been observed experimentally at the boundary between an AlGaAs/GaAs superlattice and a wide-gap AlAs layer. In the present letter we report the observation of an interfacial state at the boundary between a narrow-gap *p*-GaAs layer and an AlAs/GaAs superlattice and the observation of resonances corresponding to transformation of interfacial and Stark discrete levels into virtual levels.

The experimental samples consisted of p–i–n diodes, whose undoped i regions contained short-period $(\mathrm{AlAs})_m/(\mathrm{GaAs})_n$ superlattices with $m=3$ and $n=10$–13 monolayers (ML) and 50 periods. The samples were grown by molecular-beam epitaxy (MBE) on GaAs(100) substrates.[9,10] The superlattice was separated from the substrate by a 1000 nm thick, heavily doped n^+-GaAs buffer layer, which was used as the bottom contact. A 200 nm thick p^+-GaAs contact layer was grown on top of the superlattice. The contact regions were doped to 5×10^{18} cm^{-3}. The details of the method used to grow the superlattices and to monitor their structural perfection are described in Refs. 9 and 10. Mesa structures ≈ 1 mm in diameter and Ohmic contacts to the *n*- and *p*-type layers were prepared on the initial epitaxial structures. Measurements of the spectra of the photocurrent arising between the contacts under illumination of the structure were performed at 4.2 K on the automated setup described in Ref. 10.

The measured voltage dependences of the photocurrent $J(V)$ for mesa structures prepared on different sections of the growth ring are shown in Fig. 1 (dots). Here V is the total voltage drop across the superlattice with allowance for the built-in potential of the p–i–n structure, $V_0=1.52$ V. Because the superlattice parameters varied over the area of the ring, the mesa structures correspond to a different effective width d_{GaAs} of the GaAs wells in the range 10–12 ML. The measurements were performed for photon energies near the band gap of GaAs. In the given spectral region, the probability of optical transitions on Wannier–Stark levels[4] decreases exponentially with the photon energy, so that these transitions are not observed in the form of individual peaks. At the same time transport resonances (peaks 1–4) are observed in the $J(V)$ curves because of photoelectron production in the contact region. As shown in Ref. 11, the position of these resonances does not depend on the photon energy and corresponds to electron tunneling from the *p*-GaAs layer into the Stark levels in the superlattice. To show more clearly the characteristic features of the photocurrent in the voltage range 2–6 V, a fragment of one of the measured $J(V)$ curves is constructed in the inset using a linear scale. It is evident from Fig. 1 that the $J(V)$ curves for different mesa structures have a similar form. It is also evident that as d_{GaAs} increases, the positions of the transport resonances systematically shift in the direction of lower voltages. This shift is due to the decrease in the energy of the ground quantization level in GaAs wells. At the same time the reason for the nonmonotonic dependence of the amplitude of the resonances on the resonance number as well as the origin of the additional, wider, photocurrent peak, which is most clearly seen in the inset in Fig. 1 between the first and second Stark resonances, are unclear.

To clarify these questions we calculated the energy spectrum, wave functions, and current in the experimental superlattice. The calculation was performed by solving numerically the Schrödinger equation using the method described in Ref. 12. The problem of the reflection and transmission of electrons incident on the superlattice from the *p*-GaAs contact region was solved. The superlattice parameters were determined by com-

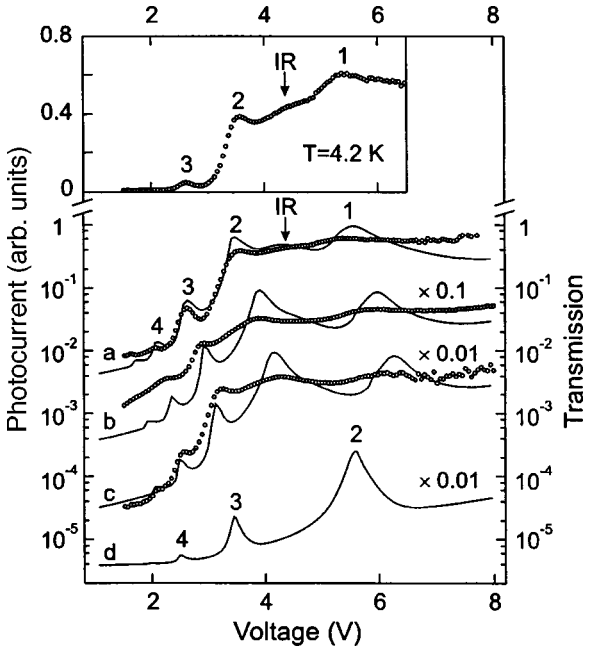

FIG. 1. Experimental (circles, left-hand scale) and theoretical (solid lines, right-hand scale) curves of the photocurrent J versus the potential V for different mesa structures corresponding to effective width d_{GaAs} of the wells in the AlAs/GaAs superlattice (in monolayers): a) $d_{\mathrm{GaAs}}=11.8$ ML; b) 10.4 ML; c) 9.8 ML. Curve d was calculated neglecting the interfacial potential well. The experimental curves were measured at $T=4.2$ K with photon energies $\hbar\omega$ near the band gap of GaAs: a) $\hbar\omega=1.521$ eV; b) 1.653 eV; c) 1.550 eV. The numbers denote the peaks of resonance origin via the Stark levels of the corresponding GaAs wells; the arrow marks a resonance with an interfacial level (IR). The curves are shifted along the vertical axis as a visual aid. Inset: Fragment of the experimental curve (linear scale) measured on the mesa structure a.

paring the calculations with the measured field dependences of the positions of the optical resonances — the peaks in the photocurrent spectra that correspond to direct and indirect optical transitions to the Wannier–Stark levels.[10] The thicknesses d_{GaAs} of the GaAs wells presented in the caption to Fig. 1 were determined from such a comparison for each mesa structure. As shown in Ref. 10, the deviations of the layer thicknesses from integer values are due to the atomic-scale roughness of the heterointerfaces. The fluctuations of the barrier thicknesses d_{AlAs} have a much weaker effect on the electron energy spectrum, so that we employed the nominal value $d_{\mathrm{AlAs}}=3$ ML. Comparing the calculations and the experimental dependences of the optical resonances on the voltage across the p–i–n structure showed that the width of the i layer is 4–10 nm greater than the width of the superlattice because of the presence of thin, dopant-depleted, $p(n)$-GaAs regions near the superlattice. The penetration of the electric field in the contact region results in the formation of a potential well in front of the superlattice. All forms of elastic and inelastic electron scattering by the irregularities of the heterointerfaces and by phonons were taken into account by fixing the imaginary correction to the potential over the entire length of the superlattice. The imaginary part of the potential describes the departure of particles from a given coherent state in the ''lifetime'' approximation $\tau=\hbar/\mathrm{Im}[U(x,E)]$, where x is the coordinate and E is the energy component corresponding to motion along the axis

of the superlattice. The reflection coefficient R in the elastic channel was calculated as a function of the electric field. The transmission coefficient T determining the magnitude of the photocurrent was calculated as $T=1-R$, since as a result of energy and momentum dissipation the electrons that have entered the superlattice can no longer return into the *p*-GaAs layer and they contribute to the photocurrent.

The theoretical curves of the electron transmission coefficient $T(V)$ as a function of voltage are shown in Fig. 1 (solid lines a, b, and c). These curves were computed for three mesa structures with different thicknesses of the GaAs layers with allowance for the presence of a triangular interfacial well in front of the superlattice. The width $d_i=4$ nm of the interfacial well and the characteristic kinetic energy of the electrons incident on the superlattice, $E_0=3.5$ meV, were found by obtaining the best fit of the theoretical curves to the experimental curves. For comparison, curve d shows the dependence $T(V)$ calculated neglecting the interfacial well for a superlattice with $d_{\mathrm{GaAs}}=11.8$ ML. It is evident that the computed curves a–c satisfactorily describe the experiment, including the position, shape, and nonmonotonic dependence of the amplitude on the number for transport resonances (peaks 1–4), corresponding to Wannier–Stark levels in wells 1–4 lining up with the bottom of the continuum in *p*-GaAs. The photocurrent peaks 1–4 arise as a result of the successive transformation of the edge Stark levels of the superlattice into virtual levels. Comparing the curves a and d in Fig. 1 shows that a correct calculation of the tunneling, taking into account the presence of a potential well for electrons at the boundary with the contact layer, makes it possible not only to describe correctly the general form of the voltage dependences of the photocurrent but also to refine the numbering of the transport resonances.[11] We note that the fact that E_0 is greater than the average thermal energy could be due to the smearing of the energies of the incident electrons because of the fluctuation potential of the charged impurities. The smearing of the energies and the fluctuations of the layer thicknesses also lead to additional broadening of the measured transport resonances as compared with the computed resonances.

It is noteworthy that the calculation also reproduces well the additional resonance shown by the arrow between the first and second Stark resonances (Fig. 1). To determine the nature of the observed resonances we analyzed plots of the probability density distributions $|\Psi|^2$ of the incident electrons along the axis of the superlattice. These plots, calculated for various voltages on the superlattice, are shown in Fig. 2. The solid curves 1, 2, 4, and 10 correspond to transport resonances with Stark levels in the fourth, third, second, and first wells, respectively. It is evident that for these curves the maximum of $|\Psi|^2$ shifts systematically from the fourth into the first GaAs well of the superlattice. The curves $|\Psi|^2$ displayed in Fig. 2 (dashed lines) show that electron penetration into the superlattice does not occur for intermediate nonresonant values of the field. The solid curve *7* corresponds to a maximum of the additional interfacial resonance (IR). Analysis showed that this resonance corresponds to transformation of a quasidiscrete interfacial level in the well between the *p*-GaAs contact layer and the superlattice ($V>4.32$ V) into a virtual level with $V<4.32$ V. The quasidiscrete resonance state corresponds to slow exponential decay of the wave function into the contact region and rapid oscillatory decay into the superlattice. In Fig. 2, an interfacial resonance appears as an increase in the probability of observing an electron near the *p*-GaAs boundary with the superlattice. From the form of the curves 5–9 in Fig. 2 it is evident that the passage of an interfacial resonance is accompanied by substantial displacement of the nodes and antinodes of the

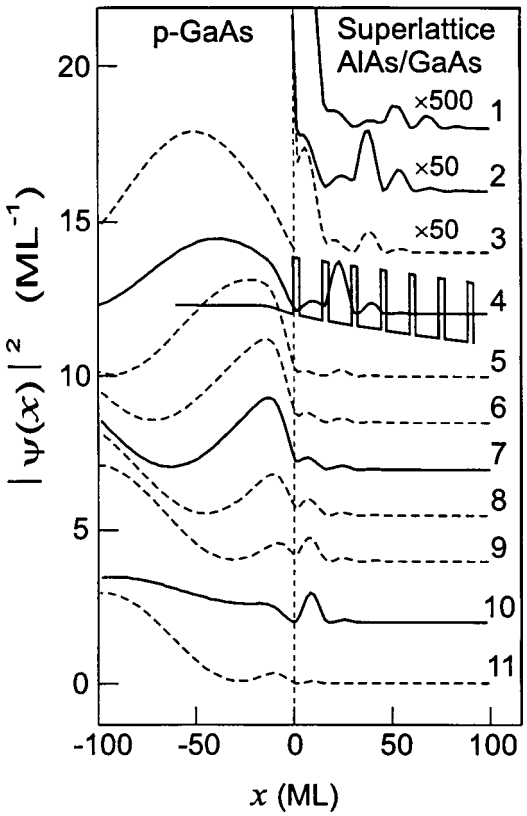

FIG. 2. Curves of the probability density $|\Psi|^2$ versus the coordinate along the axis of the GaAs/AlAs superlattice for $d_{GaAs}=11.8$ ML and different values of the voltage V: 1 — $V=2.08$ V; 2 — 2.61 V; 3 — 2.9 V; 4 — 3.44 V; 5 — 3.9 V; 6 – 4.2 V; 7 — 4.32 V; 8 — 4.6 V; 9 — 4.9 V; 10 — 5.55 V; 11 — 6.3 V. The solid curves 1, 2, 4, and 10 correspond to resonances of electrons, incident from the *p*-GaAs layer, with Stark levels in the fourth, third, second, and first GaAs wells, respectively. The solid curve 7 corresponds to a maximum of the interfacial resonance. The dashed curves correspond to intermediate (nonresonant) values of the potential. The profile of the superlattice potential in the conduction band is shown schematically together with curve 4.

electron wave in the contact layer. These displacements correspond to a change in the phase of the reflected wave as the interfacial level emerges into the *p*-GaAs continuum.

It is evident from Fig. 1 that the narrow Stark resonances appear against the background due to a wide interfacial state. The interaction of the resonances increases the probability of electron tunneling into the superlattice and leads to the characteristic nonmonotonic form of the photocurrent curves. For mesa structure a, the interfacial resonance falls in the interval between the first and second Stark resonances and therefore appears in the form of an individual spectral feature on the computed curve and in the experiment (see inset in Fig. 1). As the width of the GaAs wells decreases (curves b and c), the Stark resonances shift in the direction of stronger electric fields. As a result, for curve c the interfacial and second Stark resonances merge into a single wide, intense peak. In the absence of an interfacial potential well and, correspondingly, an interfacial

resonance, the probability of electron tunneling from *p*-GaAs into the superlattice drops sharply (curve d in Fig. 1).

Thus, in the present work the transformation of quasidiscrete resonance levels into virtual levels as a result of the variation of the electric field in an AlAs/GaAs superlattice was studied experimentally and theoretically. An interfacial state was observed to arise at the boundary between the superlattice and the contact layer. The presence of this state increases the probability of photoelectron tunneling from the contact into the superlattice via Wannier–Stark levels and makes it possible to control the phase of the electronic waves in the contact region by varying the voltage on the structure.

We thank A. S. Terekhov for a helpful discussion of this work. This work was supported by the Russian Fund for Fundamental Research (Grant 96-02-19060), the Federal Target Program ''Integratsiya'' (through Novosibirsk State University, Project 274), and the Scientific–Technical Program ''Physics of Solid-State Nanostructures'' (Grant 98-1102).

*)e-mail: alper@thermo.isp.nsc.ru

[1] L. D. Landau and E. M. Lifzhitz, *Quantum Mechanics*, 3rd ed., rev. and enl. (Pergamon Press, Oxford–New York, 1977) [cited Russian original, Nauka, Moscow, 1989].
[2] L. I. Schiff, *Quantum Mechanics*, 2nd ed. (McGraw-Hill, New York, 1955) [Russian translation, Inostr. Lit., Moscow, 1957].
[3] G. H. Wannier, Phys. Rev. **117**, 432 (1960).
[4] E. E. Mendez, F. Agullo-Rueda, and J. M. Hong, Phys. Rev. Lett. **60**, 2426 (1988).
[5] H. Schneider, H. T. Grahn, K. von Klitzing, and K. Ploog, Phys. Rev. Lett. **65**, 2720 (1990).
[6] H. Nagasawa, K. Murayama, M. Yamaguchi *et al.*, Solid-State Electron. **40**, 245 (1996).
[7] H. Ohno, E. E. Mendez, J. A. Brum *et al.*, Phys. Rev. Lett. **64**, 2555 (1990).
[8] I. Tamm, Phys. Z. Sowjetunion **1**, 733 (1932).
[9] N. T. Moshegov, L. V. Sokolov, A. I. Toropov *et al.*, Inst. Phys. Conf., Ser. No. 145: Chapter 2, 97 (1996).
[10] V. L. Al'perovich, N. T. Moshegov, V. V. Popov *et al.*, Fiz. Tverd. Tela (St. Petersburg) **39**, 2085 (1997) [Phys. Solid State **39**, 1864 (1997)].
[11] V. L. Al'perovich, N. T. Moshegov, A. S. Terekhov *et al.*, Fiz. Tverd. Tela (St. Petersburg) **41**, 159 (1999) [Phys. Solid State **41**, 143 (1999)].
[12] V. A. Tkachenko, O. A. Tkachenko, G. L. Kotkin, and V. G. Tupitsin, Physica B **175**, 75 (1991).

Translated by M. E. Alferieff

Plasticization effect and the excitation of the electronic subsystem in an LiF single crystal by an ultraweak thermalized-neutron flux in the stress-relaxation regime

A. G. Lipson,*) D. M. Sakov, V. I. Savenko, and E. I. Saunin
Institute of Physical Chemistry, Russian Academy of Sciences, 117915 Moscow, Russia

(Submitted 1 June 1999; resubmitted 16 June 1999)
Pis'ma Zh. Éksp. Teor. Fiz. **70**, No. 2, 118–123 (25 July 1999)

Plasticization is detected during stress relaxation in uniaxially loaded LiF single crystals irradiated with an ultraweak flux of thermalized neutrons (UFTN) with intensity $I_n \sim 100$ neutrons/cm^{2}s. It is shown that when loaded LiF samples are irradiated with an UFTN, excitation of the electronic subsystem of the crystal is observed and is manifested in a stimulation of deformation exoemission of electrons and the generation of F centers. © *1999 American Institute of Physics.* [S0021-3640(99)01014-2]

PACS numbers: 61.80.Hg, 62.40.+i, 62.20.Fe

It has been established previously that during irradiation of certain strongly nonequilibrium solids with an ultraweak flux of thermalized neutrons (UFTN) with intensity $I_n \leqslant 10^2$ neutrons/cm^{2}s, one observes an anomalous increase of the capture of the neutron flux, accompanied by a measurable generation of defects in the irradiated crystals.[1–3] It should be noted that the effects observed under UFTN irradiation are nontrivial, since from the energy standpoint their formation at first glance appears to be not in keeping with the neutron fluence interacting with the sample. For this reason, defect formation in crystals under UFTN irradiation can be attributed to a manifestation of a basically ''ultralow dose'' synergetic effect that destroys the energy barrier.[4] At the same time it has recently been established[5] that very weak electromagnetic influences affect the dynamics of dislocations and point defects in surface layers of alkali-halide crystals (AHCs). This effect has been studied in detail in Refs. 6 and 7. It indicates that the change in the defect structure of AHCs and, specifically, their plastic flow likewise can be stimulated by absorption of quite small amounts of energy.

In the present work, to determine the nature of the effect of UFTN on nonequilibrium crystalline systems we investigated the regimes of relaxation of mechanical stresses and the accompanying processes leading to stimulation of deformation electron exoemission (DEE)[8–10] in LiF crystals irradiated with an ultraweak flux of thermalized neutrons.

In the experiments we used LiF single crystals (produced by LOMO), grown from the melt, with total divalent impurity concentration $\sim 10^{-3}$ at. %. The yield stress of the crystals was $\sigma_y = 9.0$ MPa. Immediately before being placed into the apparatus, $10 \times 5 \times 1.5$ mm samples were punched out of a monoblock along (001) cleavage planes and pressed between dies to a fixed total deformation. The initial uniaxial compression stress

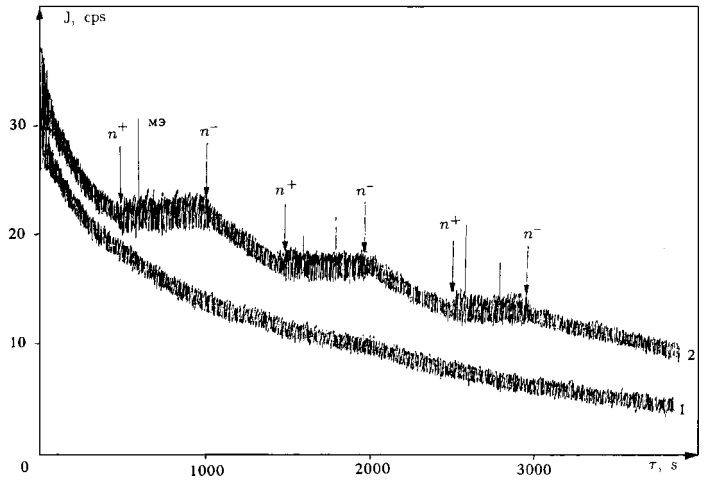

FIG. 1. Curve *1*: DEE kinetics of an LiF single crystal (fresh cleavage) under a uniaxial load $\sigma = 7.0$ MPa under conditions of the natural thermal-neutron background (residual strain $\epsilon_p < 0.1\%$). Curve *2*: Same for a different LiF sample with $\sigma = 7.0$ MPa in the presence of an UFTN source with $I_n = 100$ neutrons/cm^{2}s (n^+) and with the source removed (n^-). The arrows mark the moments when the neutron source is inserted and removed (residual strain of the sample $\epsilon_p \simeq 0.1\%$).

was chosen in the range $\sigma = 7.0$–10 MPa, depending on the experimental conditions. The holder together with the sample was placed into a vacuum chamber ($P = 10^{-6}$ Torr). The DEE was detected using a VÉU-6 channel electron multiplier. The vacuum apparatus, which is described in Ref. 11, was surrounded by a 15 cm thick layer of ''neutrostop'' (Co) polyethylene blocks to ensure thermalization and reflection of thermal neutrons. To produce a field of thermalized neutrons, a Cf-252 source of fast neutrons with intensity $I = 1.5 \times 10^3$ neutron/s, emitted into a 4π solid angle, was placed inside the apparatus 20 cm from the sample. The neutron source placed in a lead container, in turn, was covered with a 5 cm thick polyethylene shell.

Neutron-radiation analysis was used to determine the intensity of the thermalized-neutron flux and the fraction of UFTN captured in the sample.[3] Electron spin resonance was used to estimate the concentration of color centers (*F* type) generated in LiF crystals, under a mechanical load, by the UFTN.[11,12]

The kinetics of DEE in an LiF crystal held in a regime of stress relaxation below the macroscopic yield stress in the absence of UFTN is displayed in Fig. 1 (curve *1*). As expected, the DEE curve in this case decays exponentially, which is due to the damping of the dislocation current under conditions of stress relaxation in the sample.[8,9] When the UFTN (n^+) source is inserted into the setup, the DEE decay stops rapidly (Fig. 1, curve *2*). After the neutron source is removed (n^-) the DEE decay is restored almost instantaneously. This continues with repetition of the procedures (n^+)$\leftrightarrow$(n^-) up to a decrease of the emission intensity by approximately a factor of 2 from the initial level. At the same time, when the UFTN source is inserted, periodic electron mechanoemission spikes are observed to appear; these spikes are absent under conditions of the natural neutron background (Fig. 1, curve *1*) and indicate the formation of microcracks in the near-surface layer of the deformed crystal.[13] In the presence of macroscopic residual deformation of

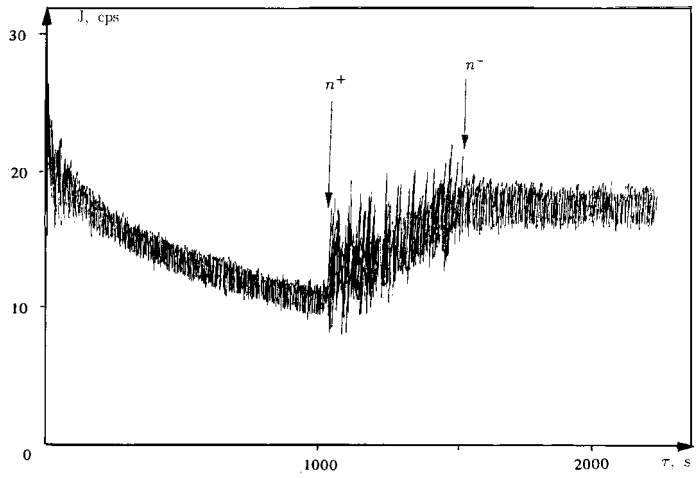

FIG. 2. DEE kinetics in a uniaxially loaded LiF crystal ($\sigma=9.2$ MPa) with insertion (n^+) and removal (n^-) of a neutron source (residual strain of the sample $\epsilon_p \simeq 1.5\%$).

single crystals, after the removal of the load and after irradiation with UFTN, i.e., for $\epsilon_p \gg 1\%$, the character of the DEE kinetics (Fig. 2) is fundamentally different from that in samples where the residual deformation is weak. The insertion of a neutron source (n^+) for samples under a stress close to the macroscopic yield point (Fig. 2) leads to their additional deformation, accompanied by an increase in the integrated intensity of DEE and microcrack formation, which leads to intense electron mechanoemission spikes. When the source is removed (n^-), the DEE intensity does not decrease, i.e., the decay before the introduction of the UFTN is nor restored, since under macroplastic deformation of the crystal substantial internal microstresses, additionally stimulating displacement of the mobile dislocations and, in consequence, increasing the DEE yield, arise at the ends of the stopped slip bands.

It should be underscored that the observed changes produced in the kinetic features of DEE as a result of the interaction of uniaxially loaded LiF crystals with UFTN, despite the individuality of the DEE spectrum of each individual crystal, are definite (not statistical), since the detection of DEE under conditions of the natural background and in the presence of UFTN is performed in different time intervals on the same sample.

According to existing ideas concerning the mechanism of dislocation exoemission of electrons in AHCs, for low strain rates ($\dot{\epsilon}_p \sim 10^{-5}$)[9] the DEE intensity is determined by the dislocation current density in the loaded crystal and by the concentration of *F* centers in it. For the DEE current to be constant, the dislocations moving toward the sample surface must strip electrons from the *F* centers. The increase in the dislocation current in the crystals under UFTN irradition in our experiments is confirmed by the presence of a significant additional residual plastic deformation of the samples. The generation of *F* centers in LiF single crystals was estimated by extrapolating the data obtained for powdered samples prepared by pulverizing the initial single crystals, since because of the weakness of the detected ESR signal it is impossible to determine the color centers in single crystals which have not been colored in advance. The use of freshly pulverized LiF

FIG. 3. ESR spectra of LiF powders at $T=300$ K, dispersed for 15 min under conditions of the natural neutron background (*1*) and under UFTN irradiation:[11] $I_n=100$ neutrons/cm^{2}s.

powders makes it possible, at least, to judge qualitatively the contribution of UFTN to the generation of F centers in loaded crystals. Figure 3 shows the ESR spectra obtained at $T=300$ K. The spectrum of an LiF crystal pulverized in 15 min under the conditions of the natural neutron background consists of a wide line ($\Delta H=120$ Oe, $g=2.0018$), which is attributed to the signal from F centers[14] localized isotropically in dispersed particles (Fig. 3, curve *1*). The intensity of the signal obtained for powder pulverized under conditions of the natural neutron background is quite low, $I_1\sim 10^{14}$ spins/g. At the same time the intensity of the analogous signal (Fig. 3, curve *2*) obtained for LiF powders dispersed in 15 min under irradiation with UFTN[11] is at least an order of magnitude greater ($I_2\sim 10^{15}$ spins/g). For this reason the ESR data permit drawing the conclusion that the irradiation of LiF crystals with UFTN during mechanical loading results in the additional generation of electronic color centers (F centers).

To a first approximation the mechanism leading to of plasticization and a change in the kinetics of DEE under UFTN irradiation is as follows. When the UFTN source is introduced (Fig. 1, curve *2*, n^+), dislocation transport and point-defect generation should intensity in the interior volume of the crystal. Thermodynamically, this effect is equivalent to an increase in the rate of plastic deformation or an increase in the temperature of the sample under a mechanical load. Irradiation of samples with UFTN during stress relaxation results in the appearance of an additional DEE component as a result of an increase in the mobility of dislocations and the generation of F centers. When the source of UFTN is removed, the velocity of mobile dislocations decreases, which lowers the level of plastic deformation of the crystal, a consequence of which will be a dropoff of DEE (Fig. 1, curve *2*, n^-). We note that microcrack formation, manifested as spikes in electron mechanoemission, attests to intensification of the plastic deformation of LiF samples under irradiation.

We shall now consider the possible physical causes of the observed plasticization and excitation of the electronic subsystem of loaded LiF crystals under UFTN irradiation. As measurements of neutron fluxes in the working volume of the apparatus by neutron-radiation analysis showed, in the process of uniaxial compression of LiF single crystals, up to 3.0% of the thermalized-neutron flux incident on the sample is absorbed. Effects of UFTN absorption which are close in magnitude have been observed previously in other nonequilibrium crystalline systems, where thermal neutrons change the physical properties.[1–3] It can be inferred that the anomalous absorption of thermalized neutrons in a loaded LiF crystal is due to the inelastic energy losses by slow neutrons scattered by

nonequilibrium optical phonons[15] generated in the lattice under the mechanical excitation.[16] We shall estimate the effect of UFTN on the dynamics of dislocation transport in a LiF single crystal on the basis of the idea that a large fraction of the energy of compound nuclei which are produced as a result of the capture of thermal neutrons is absorbed directly by the lattice surrounding nucleus[1] (neutron Mössbauer effect[17]). When the energy of compound nuclei is shed in the form of lattice excitations in zones of stress concentration, it can be efficiently transferred to dislocations and/or dislocation-blocking obstacles (impurities and point defects). For typical strain rates $\dot{\epsilon}_p \sim 10^{-5}$ s^{-1} the density of mobile dislocations in the interior volume of a crystal is $N_d = 10^5$ cm^{-2} (Refs. 9 and 18). Taking into account the characteristic time during which the UFTN acts in our experiments $\tau_n \sim 10^3$ s (Figs. 1 and 2) and using the known relation[19] between the plastic deformation in the stress relaxation regime and the average dislocation velocity v_d, viz., $\epsilon_p = \dot{\epsilon}_p \tau_n = N_d b v_d \tau_n$, where b is the Burgers vector and $v_d = v_0 \exp[-(U_0 - \gamma\sigma)/kT]$, we can estimate the specific power W_d required to ensure plasticization of LiF samples as a result of an increase in dislocation velocity ($v_{d_0} \rightarrow v_n$) under UFTN irradiation. Since in the model under study the energy required to increase the dislocation velocity is actually taken from the phonon subsystem of the crystal,[15] the corresponding estimate gives $W_d = \tau_n^{-1} c_p \rho [kT^2/(U_0 - \gamma\sigma)] \ln(\epsilon_{pn}/\epsilon_{p_0}) \approx 1$ J/cm^{3}s. Here $c_p = 42$ J/g$\cdot$deg is the specific heat of the sample, $\rho = 2.6$ g/cm^3 is the density of the sample, $T = 300$ K is the temperature, $U_0 - \gamma\sigma \approx 0.7$ eV is the activation energy for depinning of dislocations from obstacles in a loaded sample,[19] $\gamma = 10^{-21}$ cm^3 is the activation volume swept out by a dislocation depinned from an obstacle, and ϵ_{pn} and ϵ_{p_0} are the plastic deformation in the presence and absence of UFTN, respectively ($\epsilon_{pn}/\epsilon_p \cong 10$).

At the same time, an estimate of the specific power W_c released in zones of stress concentration, i.e., on pinned sections of dislocations, as a result of the conversion of the energy of a compound nucleus produced by neutron capture into the energy of the phonon subsystem gives $W_c = (0.03 I_n E_n/h)/N_d b^2 c^{1/3} \approx 10$ J/cm^{3}s, where I_n is the intensity of the UFTN, $E_n = 2.1$ MeV is the binding energy of a neutron in a ^{8}Li nucleus, h is the thickness of the sample, and $c = 10^{-3}$ at.% is the atomic concentration of divalent obstacles in the crystal.

It follows from the estimates presented that the specific power (W_c) released by capture of thermal neutrons is approximately an order of magnitude greater than the power required to activate dislocation transport. In this connection, a substantial fraction of W_c can also be expended on the formation of anionic vacancies and filling of the vacancies with electrons, i.e., on the generation of F centers ($E_f = 5.0$ eV). In addition, new F centers are formed as a result of intensification of crossings of delocations[10] moving under conditions of uniaxial loading of AHCs and under UFTN irradiation. Therefore, when an UFTN is absorbed by a loaded LiF single crystal, conditions are produced for stimulation of plastic flow, resulting in efficient excitation of the electronic subsystem of the irradiated crystal (generation of electronic color centers and intensification of DEE). It should be underscored that effects due to disordering of AHCs under the irradiation by thermal neutrons have been previously observed only in reactor fluxes,[20] i.e., fluxes with densities at least ten orders of magnitude higher than that of the UFTN employed.

In conclusion, we note that the additional mechanism of plasticization of AHCs by

an UFTN could be rearrangement of the structure of the obstacles themselves, accompanied by a decrease in the activation barriers to dislocation motion.

To specify in greater detail the micromechanism of the observed effect, additional investigations using monoenergetic neutron beams and crystals with different impurity concentration are planned.

We thank A. V. Strelkov, V. K. Ignatovich, L. B. Pikel'ner, and S. Z. Shmurak for helpful discussions.

*)e-mail: lipson@lmm.phyche.msk.su

[1] A. G. Lipson, D. M. Sakov, and E. I. Saunin, JETP Lett. **62**, 828 (1995).
[2] A. G. Lipson, B. F. Lyakhov, E. I. Saunin *et al.*, Pis'ma Zh. Tekh. Fiz. **22**, 42 (1996) [Tech. Phys. Lett. **22**, 618 (1996)].
[3] A. G. Lipson, I. I. Bardyshev, V. A. Kuznetsov, and B. F. Lyakhov, Fiz. Tverd. Tela (St. Petersburg) **40**, 254 (1998) [Phys. Solid State **40**, 229 (1998)].
[4] Ya. B. Zel'dovich, A. L. Buchachenko, and E. L. Frankevich, Usp. Fiz. Nauk **155**, 3 (1988) [Sov. Phys. Usp. **31**, 385 (1988)].
[5] V. I. Al'shits, E. V. Darinskaya, T. M. Perekalina, and A. A. Urusovskaya, Fiz. Tverd. Tela (Leningrad) **29**, 467 (1987) [Sov. Phys. Solid State **29**, 265 (1987)].
[6] Yu. I. Golovin and R. B. Morgunov, JETP Lett. **61**, 596 (1995).
[7] V. I. Al'shits, N. N. Bekkauer, A. E. Smirnov, and A. A. Urusovskaya, Zh. Éksp. Teor. Fiz. **115**, 951 (1999) [JETP **88**, 523 (1999)].
[8] A. V. Poletaev and S. Z. Shmurak, Pis'ma Zh. Tekh. Fiz. **7**, 1352 (1981) [Sov. Tech. Phys. Lett. **7**, 577 (1981)].
[9] A. V. Poletaev and S. Z. Shmurak, Zh. Éksp. Teor. Fiz. **87**, 657 (1984) [Sov. Phys. JETP **60**, 376 (1984)].
[10] V. A. Zakrevskiĭ and A. V. Shul'diner, Fiz. Tverd. Tela (Leningrad) **27**, 3042 (1985) [Sov. Phys. Solid State **27**, 1826 (1985)].
[11] A. G. Lipson, D. M. Sakov, V. V. Gromov, and E. I. Saunin, Fiz. Tverd. Tela (St. Petersburg) **35**, 2503 (1993) [Phys. Solid State **35**, 1266 (1993)].
[12] A. G. Lipson, V. A. Kuznetsov, E. I. Saunin *et al.*, Zh. Tekh. Fiz. **67**, 100 (1997) [Tech. Phys. **42**, 676 (1997)].
[13] J. T. Dickinson, E. E. Donaldson, and M. K. Park, J. Mater. Sci. **16**, 2897 (1981).
[14] R. Kaplan and P. J. Bray, Phys. Rev. **129**, 1919 (1963).
[15] P. A. Egelstaff and G. Holt, in *Inelastic Scattering of Neutrons in Solids and Liquids*, Proceedings of an International Symposium, Chalk River, 1962, Vol. **2**, Vienna, 1963, p. 178.
[16] A. G. Lipson and V. A. Kuznetsov, Dokl. Akad. Nauk SSSR **332**, 172 (1993) [Phys. Dokl. **38**, 406 (1993)].
[17] H. Frauenfelder, *The Mössbauer Effect* (Benjamin, New York, 1962).
[18] V. Z. Bengus, E. D. Tabachnikova, and V. N. Ostroverkh, Fiz. Tverd. Tela (Leningrad) **15**, 3452 (1973) [Sov. Phys. Solid State **15**, 2306 (1973)].
[19] B. I. Smirnov, *Dislocation Structure and Ordered Crystals* [in Russian] (Nauka, Leningrad, 1981).
[20] A. A. Urusovskaya and M. N. Perzhinova, Fiz. Tverd. Tela (Leningrad) **10**, 3146 (1968) [Sov. Phys. Solid State **10**, 2487 (1968)].

Translated by M. E. Alferieff

Dynamic self-polarization of nuclei in low-dimensional systems

V. L. Korenev*)
A. F. Ioffe Physicotechnical Institute, Russian Academy of Sciences, 194021 St. Petersburg, Russia

(Submitted 21 June 1999)
Pis'ma Zh. Éksp. Teor. Fiz. **70**, No. 2, 124–129 (25 July 1999)

A mechanism of dynamic self-polarization of nuclei is studied which is weakly temperature-dependent and operates efficiently in low-dimensional systems (quantum wells, quantum dots). It is due to the hyperfine interaction of nuclei with excitons whose spin polarization is artificially maintained at zero (by illuminating with unpolarized light) but for which nonequilibrium alignment occurs. Nuclear self-polarization arises as a result of the conversion of the alignment of excitons into nuclear orientation in the effective magnetic field of the polarized nuclei. © *1999 American Institute of Physics.* [S0021-3640(99)01114-7]

PACS numbers: 76.70.Fz, 71.70.Jp

Dynamic self-polarization of nuclei (DSN) in solids was predicted by D'yakonov and Perel'.[1,2] DSN should arise in a system of nuclear spins interacting with electrons whose spins are artificially disordered (for example, by illuminating with unpolarized light). Then at temperatures below the critical temperature, T_c, the disordered state of the nuclei is unstable. The stable state is found to be one in which the nuclear spins are almost completely polarized and which is maintained by the Overhauser effect. An estimate for GaAs shows that $T_c = 1.3$ K.[3] This imposes strict limitations on the light intensity. On the one hand, the intensity must be high enough for efficient relaxation of nuclear spins on photoelectrons and low enough to avoid overheating the lattice. This is probably the reason why DSN has not been observed thus far.

In the present work we examine a different mechanism of DSN, which is weakly temperature-dependent and efficient in low-dimensional systems (quantum wells, quantum dots). It is due to the hyperfine interaction of nuclei with excitons, whose spin polarization is maintained artificially at zero by illumination with unpolarized light. Just as in Refs. 1 and 2, DSN is the result of the hyperfine interaction of nuclei with electrons (the interaction of nuclei with holes is negligibly small). However, an important feature of this mechanism is a strong correlation of the spins of the electron and the hole in the exciton, resulting in alignment of excitons (the ground state of an exciton in quantum wells contains four spin sublevels). It arises as a result of the difference of the lifetimes of the optically active and inactive excitons, it is comparatively weakly temperature-dependent, and the degree of alignment can be close to one. In the absence of a magnetic

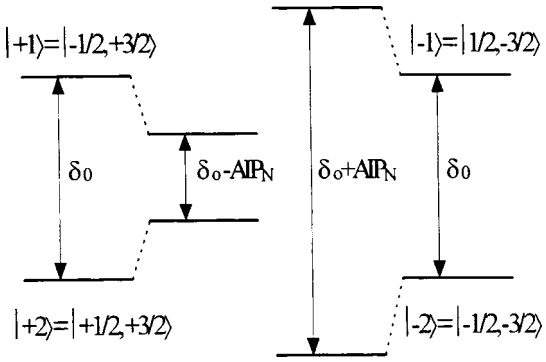

FIG. 1. Energy-level scheme for the ground state of an exciton in quantum polarization.

field the nonequilibrium alignment of excitons does not result in polarization of the nuclei. In an external magnetic field the symmetry decreases and alignment can be converted into orientation (polarization).[4] In this case the effective magnetic field of the nuclei themselves plays the role of a magnetic field: The polarized nuclei produce an effective field in which conversion of the nonequilibrium alignment of excitons into nuclear polarization occurs, the initial polarization of the nuclei increases, and the disordered state of the nuclear spins is unstable.

We note that the conversion of nonequilibrium alignment of excitons into the orientation of nuclei could be promising for producing high degrees of nuclear polarization in nanostructures.

We shall examine in greater detail the essence of the self-polarization of nuclei interacting with excitons. The ground state $el-hh1(1s)$ of an exciton with a heavy hole, localized in a quantum well with a zinc blende lattice, is fourfold degenerate and is characterized by angular momentum projection $M=s+j=\pm 1,\ \pm 2$ on the growth axis $z \| [001]$ of the structure (the electron spin $s=\pm 1/2$ and the hole angular momentum $j=\pm 3/2$). The exchange interaction splits this state into a radiative doublet $|\pm 1\rangle$ and a nonradiative doublet $|\pm 2\rangle$ (we neglect the comparatively small doublet splittings due to the low symmetry of the nanostructure).[5] Figure 1 shows the energy-level scheme of excitons in GaAs-type quantum-size structures (δ_0 is the exchange splitting in an exciton). If a small polarization of nuclei, $P_N>0$, has appeared as a result of fluctuations, then the electron in an exciton undergoes Zeeman splitting: $E_z=sAIP_N$ (A is the hyperfine structure constant and I is the nuclear spin). The energy of the excitonic levels in which the electron spin is directed upwards increases (the states $|+2\rangle$ and $|-1\rangle$), while the energy of states with the electron spin directed downwards (the states $|-2\rangle$ and $|+1\rangle$) decreases (see Fig. 1). We shall assume that only optically inactive excitons $|\pm 2\rangle$ exist and that the number of excitons in the states $|+2\rangle$ and $|-2\rangle$ is the same. In other words, alignment of the excitons exists but their polarization is zero. We assume the lattice temperature T to be sufficiently high so that the thermal energy is much greater than the characteristic spin splittings, and the D'yakonov–Perel' mechanism of self-polarization of nuclei[1,2] plays no role. The hyperfine interaction induces exciton transitions from the state $|+2\rangle$ to the state $|+1\rangle$ (in the process, the angular momentum projection of the nucleus increases by 1) with probability W_+ and also from the state

$|-2\rangle$ to the state $|-1\rangle$ (the projection of the nuclear angular momentum decreases by 1) with probability W_-. In the first case the initial polarization of the nuclei increases and in the second case it decreases. DSN arises as a result of the dependence of the polarization time of the nuclei on the magnitude of the splitting of the spin levels of an electron: The smaller the splitting, the more rapidly the electrons polarize the nuclei.[3] Then it is easy to see that $W_+ > W_-$. Therefore the initial fluctuation increases, the splitting of the electron decreases even more, and so on. As a result, a stationary state in which $AIP_N \approx \delta_0$ is established. Since in type-I GaAs-based quantum wells $\delta_0 \approx 100$ μeV[5] and $AI \approx 100$ μeV,[3] the polarization P_N of the nuclei is close to 1. Localized excitons (on island fluctuations of the quantum-well width or exciton in a quantum dot) are responsible for the dynamic polarization, since the dynamic polarization time of the nuclei by free excitons is large,[6] just as in the case of bulk semiconductors.[3] The polarized nuclei must split the spin levels of the optically active excitons $|\pm 1\rangle$, which can be observed, for example, in experiments on optical near-field spectroscopy.[7]

We shall now determine the magnitude of the nuclear polarization, assuming that $W_+ \neq W_-$. The hyperfine interaction conserves the total spin of the nucleus–electron system in an exciton, so that the equations of balance for the stationary populations N_μ of the spin sublevels of nuclei with spin I have the form

$$W^+_{\mu,\mu-1} N_\mu n_1 + W^-_{\mu,\mu-1} N_\mu n_{-2} = W^+_{\mu-1,\mu} N_{\mu-1} n_2 + W^-_{\mu-1,\mu} N_{\mu-1} n_{-1}, \tag{1}$$

where n_1, n_2, n_{-1}, and n_{-2} are the numbers of excitons with angular momentum projections $+1$, $+2$, -1, and -2, respectively; μ is the projection of the nuclear spin momentum on the z axis. The probability $W^+_{\mu,\mu-1}$ in the first term on the left-hand side of Eq. (1) describes a transition of a nucleus from the state $|\mu\rangle$ to the state $|\mu-1\rangle$ and of an electron from $|s=-1/2\rangle$ to $|s=+1/2\rangle$), forming an exciton with a hole for which $j=+3/2$ (see Fig. 1). The probability $W^+_{\mu-1,\mu}$ of the reverse transition is related with the probability of the direct transition by a thermodynamic relation $W^+_{\mu,\mu-1} = \exp(\epsilon/T) W^+_{\mu-1\mu}$ (where ϵ is the energy difference between the states $|\mu, s=-1/2, j=+3/2\rangle$ and $|\mu-1, s=+1/2, j=+3/2\rangle$). At high temperatures $W^+_{\mu,\mu-1} = W^+_{\mu-1,\mu} \equiv W_+$. The probabilities $W^-_{\mu,\mu-1} = W^-_{\mu-1,\mu} \equiv W_-$ for the flipping of the spins of the nucleus and the electron, forming an exciton with a hole for which $j=-3/2$, have an analogous meaning. We find from Eq. (1)

$$\frac{N_\mu}{N_{\mu-1}} = \frac{W_+ n_r + W_- n_{nr}}{W_+ n_{nr} + W_- n_r} = \frac{1 - wP_{12}}{1 + wP_{12}}, \tag{2}$$

where $n_r = n_1 + n_{-1}$ and $n_{nr} = n_2 + n_{-2}$ are the numbers of optically active and inactive excitons, respectively; the parameter $P_{12} = (n_{nr} - n_r)/(n_{nr} + n_r)$ is the degree of alignment of the excitons, while the parameter $w = (W_+ - W_-)/(W_+ + W_-)$ characterizes the difference of the rates of polarization of the nuclei by electrons forming an exciton with a $j=+3/2$ hole (W_+) and a $j=-3/2$ hole (W_-). The degree of polarization P_N of the nuclei can be expressed in terms of the Brillouin function

$$P_N = B_I(Ix) \quad \text{and} \quad x = \ln\left(\frac{1 + wP_{12}}{1 - wP_{12}}\right). \tag{3}$$

This equation makes it possible to determine the stationary value of the nuclear polarization for known P_{12} and w. The quantity P_{12} is determined by the kinetics of creation,

relaxation, and recombination of excitons and is assumed to be independent of the nuclear polarization. However, w depends strongly on P_N because the polarization rates of the nuclei depend on the splitting ΔE of the electron spin levels. Indeed, the rate of polarization of the nuclei by localized electrons has the form[3]

$$W \propto \frac{\Gamma^2}{\Gamma^2+(\Delta E)^2}, \tag{4}$$

where the parameter $\Gamma=\hbar/\tau_c$ is inversely proportional to the correlation time τ_c of the random field produced by electrons at the nuclei and inducing transitions between the spin sublevels of the nuclei. Using Eq. (4), the following relation can be obtained between the polarization rates of the nuclei:

$$\frac{W_+}{W_-}=\frac{\Gamma^2+(E_{-1}-E_{-2})^2}{\Gamma^2+(E_1-E_2)^2}. \tag{5}$$

Here the splitting of the spin levels of an electron forming an exciton with a hole with $j=-3/2$ is essentially the splitting of the excitonic states $|-2\rangle$ and $|-1\rangle$, i.e., $\Delta E=E_{-1}-E_{-2}=\delta_0+AIP_N$ (Fig. 1). Similarly, for an electron forming an exciton with a $j=+3/2$ hole, the splitting $\Delta E=E_1-E_2=\delta_0-AIP_N$. In the first case the splitting increases in the effective magnetic field of the nuclei, while in the second case it decreases. Using these relations we obtain

$$w=\frac{2\delta_0 AIP_N}{(AIP_N)^2+\delta_0^2+\Gamma^2}. \tag{6}$$

Equations (3) and (6) give the solution of the problem of dynamic self-polarization of nuclear interacting with localized excitons. They can be solved numerically. However, an analytical solution can be obtained if the polarization of the nuclei is not too large. For this, we expand the Brillouin function in a series and retain the first term. Then, taking account of Eq. (6), we have

$$P_N=qP_N\frac{1}{1+\gamma^2+(\alpha P_N)^2}, \tag{7}$$

where

$$q=\frac{4AI(I+1)}{3\delta_0}P_{12}, \quad \gamma=\frac{\Gamma}{\delta_0}, \quad \alpha=\frac{AI}{\delta_0}.$$

Equation (7) always has a solution for $P_N=0$. However, for $q>1+\gamma^2$ there are two additional solutions corresponding to a nonzero polarization of the nuclei

$$P_N=\pm\sqrt{q-1-\gamma^2}/\alpha. \tag{8}$$

The limit of stability of the state with $P_N=0$ can be obtained using the dynamical equation describing the relaxation of nuclei with characteristic time T_1 to the stationary value (7) near $P_N=0$:

$$\frac{dP_N}{dt}=-\frac{1}{T_1}\left(P_N-qP_N\frac{1}{1+\gamma^2}\right)=-\frac{P_N}{T_1}\left(1-\frac{q}{1+\gamma^2}\right). \tag{9}$$

As follows from Eq. (9), for $q>1+\gamma^2$ the state with zero polarization of the nuclei is unstable.

Polarized nuclei produce an effective magnetic field that splits the states $|+1\rangle$ and $|-1\rangle$ of optically active excitons (Fig. 1) by the amount

$$|E_1-E_{-1}|=|AIP_N|=\begin{cases}\delta_0\sqrt{q-1-\gamma^2}, & q>1+\gamma^2\\ 0, & q<1+\gamma^2\end{cases}. \tag{10}$$

We shall estimate this splitting for excitons localized in type-I GaAs-based quantum wells. The typical exchange splitting is $\delta_0\approx 100$ μeV,[5] and the parameter $AI(I+1)/3\approx 100$ μeV.[3] If the number of inactive and active excitons forms the ratio 2:1, then $P_{12}=1/3$ and the parameter $q\approx 1.3$. To determine the parameter $\gamma=\hbar/\delta_0\tau_c$ it is necessary to know the correlation time of the electronic field. For localized excitons it is determined by the shortest electron spin relaxation times τ_{se} and their lifetime $\tau\sim 0.1$ ns. Experiments on optical orientation and alignment of excitons show[5] that the spin relaxation times of electrons and holes for localized excitons is of the order of their lifetime. For this reason, for making estimates we take $\tau_c=\tau=0.1$ ns. Then the parameter $\gamma^2\approx 0.01$ is negligibly small. Therefore in this case $\gamma>1+\gamma^2$ and the state with nonzero polarization of the nuclei $P_N\approx 60\%$ is stable, and the splitting of the states $|+1\rangle$ and $|-1\rangle$ is $AIP_N=60$ μeV. This splitting can be observed experimentally, for example, using near-field optical spectroscopy.[7] To estimate the parameter P_{12} we assumed that the number of inactive excitons is greater than the number of active excitons. This situation can occur with nonresonant excitation of electron–hole pairs, which then become bound into excitons. In the absence of spin relaxation, the active excitons recombine both radiatively and nonradiatively, while the inactive excitons combine only nonradiatively. If the temperature is not too high, then the nonradiative channels are frozen out, and inactive excitons will accumulate, so that P_{12} is close to 1. These are the most favorable conditions for DSN. For resonant excitation of excitons the situation is reversed. In this case $P_{12}<0$, $q<0<1+\gamma^2$, and the unpolarized state of the nuclei is stable.

We examined above DSN in the absence of an external magnetic field. However, in order for nuclear polarization not to vanish as a result of spin–spin interactions of the nuclei a stabilizing field B greater than the local nuclear field $B_L\approx 10$ Hz (Ref. 2) must be applied along the z axis. For low-dimensional systems there is one other reason. For localization of an exciton on an anisotropic island in a quantum well or in a quantum dot, there is an additional splitting of radiative and nonradiative excitonic states.[5] Here the state $|+1\rangle$ mixes with $|-1\rangle$ and the state $|+2\rangle$ mixes with $|-2\rangle$. For example, for a type-I GaAs-based nanostructure the splitting of the active states $\delta_2\sim 10$ μeV.[7] The splitting of the inactive states, as a rule, is smaller.[8] Even though the anisotropic part of the exchange interaction is less than the isotropic part ($\delta_2\sim 10$ μeV), it will prevent DSN. For this reason, it is necessary to apply an external magnetic field B (along the z axis) such that the Zeeman splitting μgB of the excitons will be greater than δ_2. For the exciton g factor, $g=1$, the field $B\geqslant 2$ kHz.

In summary, dynamic self-polarization of nuclei can be accomplished by nonresonant excitation of excitons with unpolarized light in GaAs/AlGaAs-type quantum wells placed in a magnetic field in the Faraday geometry.

I am deeply grateful to V. P. Zakharchenya for steady interest in this work and to R.

I. Dzhioev and I. A. Merkulov for fruitful discussions. This work was partially supported by the Russian Fund for Fundamental Research (Project 98-02-18213), by a Grant in Support of Scientific Schools (96-15-96393), and by the Fund for Interdepartmental Scientific-Technical Programs as part of the program ''Physics of Solid-State Nanostructures.''

*)e-mail: korenev@orient.ioffe.rssi.ru

[1] M. I. D'yakonov and V. I. Perel', JETP Lett. **16**, 398 (1972).
[2] M. I. D'yakonov, Zh. Éksp. Teor. Fiz. **67**, 1500 (1974) [Sov. Phys. JETP **40**, 746 (1974)].
[3] B. P. Zakharchenya and F. Maĭer (eds.), *Optical Orientation. Modern Problems of Condensed Media* [in Russian] (Nauka, Leningrad, 1989).
[4] R. I. Dzhioev, H. M. Gibbs, E. L. Ivchenko *et al.*, Phys. Rev. B **56**, 13405 (1997); L. S. Vlasenko, M. P. Vlasenko, V. N. Lomasov *et al.* Zh. Éksp. Teor. Fiz. **91**, 1037 (1986) [Sov. Phys. JETP **64**, 612 (1986)].
[5] E. L. Ivchenko and G. E. Pikus, *Superlattices and Other Heterostructures. Symmetry and Optical Phenomena* (Springer-Verlag, Berlin, 1995).
[6] V. K. Kalevich, V. L. Korenev, and O. M. Fedorova, JETP Lett. **52**, 349 (1990).
[7] S. W. Brown, T. A. Kennedy, D. Gammon *et al.*, Phys. Rev. B **54**, R17339 (1996); D. Gammon, S. W. Brown *et al.*, Science **277**, 85 (1997).
[8] H. W. van Kesteren, E. C. Cosman, W. A. J. A. van der Poel *et al.*, Phys. Rev. B **41**, 5283 (1990).

Translated by M. E. Alferieff

Quasi-long-range order in the random anisotropy Heisenberg model

D. E. Feldman*)

Landau Institute of Theoretical Physics, Russian Academy of Sciences, 142432 Chernogolovka, Moscow Region, Russia

(Submitted 21 June 1999)
Pis'ma Zh. Éksp. Teor. Fiz. **70**, No. 2, 130–135 (25 July 1999)

The random field and random anisotropy N-vector models are studied with the functional renormalization group in $4-\epsilon$ dimensions. The random anisotropy Heisenberg ($N=3$) model has a phase with an infinite correlation length at low temperatures and weak disorder. The correlation function of the magnetization obeys a power law $\langle \mathbf{m}(\mathbf{r}_1)\mathbf{m}(\mathbf{r}_2)\rangle \sim |\mathbf{r}_1-\mathbf{r}_2|^{-0.62\epsilon}$. The magnetic susceptibility diverges at low fields as $\chi \sim H^{-1+0.15\epsilon}$. In the random field N-vector model the correlation length is finite at arbitrarily weak disorder for any $N>3$.
 [S0021-3640(99)01214-1]

PACS numbers: 75.10.Jm

The effect of impurities on the order in condensed matter is interesting, since disorder is almost inevitably present in any system. If the disorder is weak, the short range order is the same as in the pure system. However, the large-distance behavior can be strongly modified by arbitrarily weak disorder. This happens in systems of continuous symmetry in the presence of a random symmetry-breaking field.[1] The first experimental example of this kind is the amorphous magnet.[2] During the last decade a lot of other related objects have been found. These are liquid crystals in the porous media,[3] nematic elastomers,[4] He-3 in aerogel,[5] and vortex phases of impure superconductors.[6] The nature of the low-temperature phases of these systems is still unclear. The only reliable statement is that long-range order is absent.[1,7,8] However, other details of the large-distance behavior are poorly understood.

Neutron scattering[9] reveals sharp Bragg peaks in impure superconductors at low temperatures and weak external magnetic fields. Since the vortices cannot form a regular lattice,[7] it is tempting to assume that there is a quasi-long-range order (QLRO), that is the correlation length is infinite and correlation functions vary slowly with the distance. Recent theoretical[10] and numerical[11] studies of the random field XY model, which is the simplest model of the vortex system in an impure superconductor,[6] support this picture. Theoretical advances[10] are afforded by two new technical approaches: the functional renormalization group[12] and the replica variational method.[13] These methods are free from the drawbacks of the standard renormalization group and give reasonable results. The variational method considers the possibility of spontaneous replica symmetry breaking and treats the fluctuations approximately. On the other hand, the functional renormal-

ization group provides a subtle analysis of the fluctuations about the replica-symmetrical ground state. Surprisingly, the methods yield close and sometimes even the same results.

Both techniques were originally suggested for the random manifolds[12,13] and then were used to obtain information about some other disordered systems with Abelian symmetry.[10,14–16] Less is known about non-Abelian systems. The simplest of them are the random field (RF)[1] and random anisotropy (RA)[2] Heisenberg models. The latter was introduced as a model of the amorphous magnet.[2] In spite of a long discussion, the question of QLRO in these models is still open. There is experimental evidence in favor of no QLRO.[17] On the other hand, recent numerical simulations[18] support the possibility of QLRO in these systems. The only theoretical approach developed up till now is based on the spherical approximation[19] and predicts the absence of QLRO when the number of magnetization components $N \gg 1$. However, there is no reason for this approximation to be valid at $N \sim 1$.

In this letter we study the RF $O(N>3)$ and RA $O(N>2)$ models in $4-\epsilon$ dimensions with the functional renormalization group. The large-distance behaviors of the systems are found to be quite different. While in the RF $O(N)$ model with $N>3$ the correlation length is always finite, the RA Heisenberg ($N=3$) model has a phase with QLRO. In this phase the correlation function of the magnetization obeys a power law and the magnetic susceptibility diverges at low fields.

To describe the large-distance behavior at low temperatures we use the classical nonlinear σ model with the Hamiltonian

$$H=\int d^D x\left[J\sum_{\mu}\partial_\mu \mathbf{n}(\mathbf{x})\partial_\mu \mathbf{n}(\mathbf{x})+V_{\mathrm{imp}}(\mathbf{x})\right], \tag{1}$$

where $\mathbf{n}(\mathbf{x})$ is the unit vector of the magnetization, $V_{\mathrm{imp}}(\mathbf{x})$ the random potential. In the RF case it has the form

$$V_{\mathrm{imp}}=-\sum_{\alpha} h_\alpha(\mathbf{x})n_\alpha(\mathbf{x}); \qquad \alpha=1,\ldots,N, \tag{2}$$

where the random field $\mathbf{h}(\mathbf{x})$ has a Gaussian distribution and $\langle h_\alpha(\mathbf{x})h_\beta(\mathbf{x}')\rangle = A^2\delta(\mathbf{x}-\mathbf{x}')\delta_{\alpha\beta}$. In the RA case the random potential is given by the equation

$$V_{\mathrm{imp}}=-\sum_{\alpha,\beta} \tau_{\alpha\beta}(\mathbf{x})n_\alpha(\mathbf{x})n_\beta(\mathbf{x}); \quad \alpha,\beta=1,\ldots,N, \tag{3}$$

where $\tau_{\alpha\beta}(\mathbf{x})$ is a Gaussian random variable, $\langle \tau_{\alpha\beta}(\mathbf{x})\tau_{\gamma\delta}(\mathbf{x}')\rangle = A^2\delta_{\alpha\gamma}\delta_{\beta\delta}\delta(\mathbf{x}-\mathbf{x}')$. Random potential (3) corresponds to the same symmetry as the more conventional choice $V_{\mathrm{imp}}=-(\mathbf{h}\cdot\mathbf{n})^2$ but is more convenient for further discussion.

The Imry–Ma argument[1,8] suggests that in our problem, long-range order is absent at any dimension $D<4$. One can estimate the Larkin length, up to which there are strong ferromagnetic correlations, with the following qualitative renormalization group (RG) approach. Remove the fast modes and rewrite the Hamiltonian in terms of the block spins corresponding to the scale $L=ba$, where a is the ultraviolet cutoff. Then make a rescaling such that the Hamiltonian is restored to its initial form with new constants $A(L), J(L)$. Dimensional analysis provides the estimates

$$J(L)\sim b^{D-2}J(a); \quad A(L)\sim b^{D/2}A(a). \tag{4}$$

To estimate the typical angle ϕ between neighboring block spins, one notes that the effective field acting on each spin has two contributions: the exchange contribution and a random one. The exchange contribution of order $J(L)$ is oriented along the local average direction of the magnetization. The random contribution of order $A(L)$ may have any direction. This allows one to write at low temperatures that $\phi(L) \sim A(L)/J(L)$. The Larkin length corresponds to the condition $\phi(L) \sim 1$ and equals $L \sim (J/A)^{2/(4-D)}$, in agreement with the Imry–Ma argument.[1] If Eq. (4) were exact, the Larkin length could be interpreted as the correlation length. However, there are two sources of corrections to Eq. (4). Both of them are already relevant in the derivation of the RG equation for the pure system in $2+\epsilon$ dimensions.[20] The first source is the renormalization due to the interaction, and the second results from the rescaling of the magnetization which is necessary to ensure the fixed-length condition $\mathbf{n}^2 = 1$. The leading corrections to Eq. (4) are proportional to $\phi^2 J$, $\phi^2 A$. Thus, the RG equation for the combination $(A(L)/J(L))^2$ is the following

$$\frac{d}{d\ln L}\left(\frac{A(L)}{J(L)}\right)^2 = \epsilon\left(\frac{A(L)}{J(L)}\right)^2 + c\left(\frac{A(L)}{J(L)}\right)^4, \quad \epsilon = 4 - D. \tag{5}$$

If the constant c in Eq. (5) is positive the Larkin length is indeed the same as the correlation length. But if $c<0$ the RG equation has a fixed point, corresponding to a phase with an infinite correlation length. As is seen below, either situation is possible, depending on the system.

To derive the RG equations in a systematic way we use the method, suggested by Polyakov[20] for the pure system. The same consideration as in the XY model[10] and random manifold model[12] suggests that near a zero-temperature fixed point in $4-\epsilon$ dimensions there is an infinite set of relevant operators. After replica averaging the relevant part of the effective replica Hamiltonian can be represented in the form

$$H_R = \int d^D x \left[\sum_a \frac{1}{2T} \sum_\mu \partial_\mu \mathbf{n}_a \partial_\mu \mathbf{n}_a - \sum_{ab} \frac{R(\mathbf{n}_a \mathbf{n}_b)}{T^2} \right], \tag{6}$$

where a,b are replica indices, $R(z)$ is some function, and T the temperature. In the RA case the function $R(z)$ is even due to the symmetry with respect to changing the sign of the magnetization.

The one-loop RG equations for the N-component model in $4-\epsilon$ dimensions are obtained by a straightforward combination of the methods of Refs. 12 and 20. The RG equations become simpler after the following substitution for the argument of the function $R(z)$: $z = \cos\phi$. In terms of this new variable one has to find even periodic solutions $R(\phi)$. The period is 2π in the RF case and π in the RA case. In a zero-temperature fixed point the one-loop equations are

$$d\ln T/d\ln L = -(D-2) - 2(N-2)R''(0) + O(R^2, T); \tag{7}$$

$$0 = dR(\phi)/d\ln L = \epsilon R(\phi) + (R''(\phi))^2 - 2R''(\phi)R''(0) - (N-2)[4R(\phi)R''(0) + 2\cot\phi R'(\phi)R''(0) - (R'(\phi)/\sin\phi)^2] + O(R^3, T). \tag{8}$$

The two-spin correlation function is given by the expression $\langle \mathbf{n}(\mathbf{x})\mathbf{n}(\mathbf{x}')\rangle \sim |\mathbf{x}-\mathbf{x}'|^{-\eta}$, where

$$\eta = -2(N-1)R''(0). \tag{9}$$

The same equations (7)–(9) were derived by a different and more cumbersome method in Ref. 21. In that paper the critical behavior in $4+|\epsilon|$ dimensions was studied by considering analytical fixed point solutions $R(\phi)$. In the Heisenberg model, analytical solutions are absent and they are unphysical for $N \neq 3$.[21] In this letter we search for nonanalytical $R(\phi)$. At the nonanalytical fixed point $R^{\mathrm{IV}}(\phi=0)=\infty$, and hence there is no Taylor expansion with respect to ϕ.[12] Nevertheless, an expansion in powers of $|\phi|$ does exist, similar to the case of the RF XY model.[10]

Let us consider the RA model at $N=3$. We solve Eq. (8) numerically. Since the coefficients in Eq. (8) are large as $\phi \to 0$, it is convenient to use the expansion of $R(\phi)$ with respect to $|\phi|$ at small ϕ. At larger ϕ the equation is integrated by the Runge–Kutta method. The solutions to be found have zero derivatives at $\phi = 0, \pi/2$. At $N=3$ the solution with the largest $|R''(0)|$, which corresponds to $\eta = 0.62\epsilon$ (9), has two zeroes in the interval $[0,\pi]$. There are also solutions with 4 and more zeroes. They all correspond to $\eta < 0.5\epsilon$. We shall see below that these solutions are unstable.

To test the stability of the solution with two zeroes we use an approximate method. The instability to the constant shift of the function $R(\phi)$ has no interest for us, since the constant shifts do not change the correlators.[12] To study the stability to the other perturbations it is convenient to rewrite Eq. (8), substituting $\omega[R''(\phi)]^2$ for $[R''(\phi)]^2$. The case of interest is $\omega=1$, but at $\omega=0$ the equation can be solved exactly. The solution at $\omega=1$ can be found using perturbation theory in ω. The exact solution at $\omega=0$ is $R_{\omega=0}(\phi) = \epsilon(\cos 2\phi/24 + 1/120)$. The perturbation expansion provides the following asymptotic series for η: $\eta = \epsilon(0.67 - 0.08\omega + 0.14\omega^2 - \ldots)$. The resulting estimation $\eta = \epsilon(0.67 \pm 0.08)$ agrees with the numerical result well. This allows us to expect that a stability analysis of the solution $R_{\omega=0}$ of the equation with $\omega=0$ will provide information about the stability of the solution of Eq. (8). A simple calculation shows that $R_{\omega=0}$ is stable in the linear approximation. Thus, there is a stable zero-temperature fixed point of the RG equations with the critical exponent of the correlation function

$$\eta = 0.62\epsilon. \tag{10}$$

The critical exponent γ of the magnetic susceptibility $\chi(H) \sim H^{-\gamma}$ in the weak uniform field H is given by the equation

$$\gamma = 1 + (N-1)R''(0)/2 = 1 - 0.15\epsilon. \tag{11}$$

In four dimensions the one-loop RG equations for the RA Heisenberg model allow to obtain the exact large-distance asymptotic behavior of the correlation function. It obeys the equation $\langle \mathbf{n}(\mathbf{x})\mathbf{n}(\mathbf{x}')\rangle \sim \ln^{-0.62}|\mathbf{x}-\mathbf{x}'|$. Numerical analysis of Eq. (8) shows that at $N>10$ the QLRO is absent in the RA model. This agrees with the results of the spherical approximation $N=\infty$.

Let us demonstrate the absence of physically acceptable fixed points in the RF case at $N>3$. We shall derive an inequality for critical exponents. We then show that the inequality has no solutions. We use a rigorous inequality for the connected and disconnected correlation functions[22]

$$\langle \mathbf{n}_a(\mathbf{q})\mathbf{n}_a(-\mathbf{q})\rangle - \langle \mathbf{n}_a(\mathbf{q})\mathbf{n}_b(-\mathbf{q})\rangle \leqslant \mathrm{const}\sqrt{\langle \mathbf{n}_a(\mathbf{q})\mathbf{n}_a(-\mathbf{q})\rangle}, \tag{12}$$

where $\mathbf{n}(\mathbf{q})$ is a Fourier component of the magnetization, and a,b are replica indices. The large-distance behavior of the connected correlation function at a zero-temperature fixed point can be derived from the expression $\chi \sim \int \langle\langle \mathbf{n}(\mathbf{0})\mathbf{n}(\mathbf{x})\rangle\rangle d^D x$ and the critical exponent of the susceptibility (11). At a fixed point Eq. (12) provides an inequality for the critical exponents of the connected and disconnected correlation functions.[22] Both exponents can be expressed via $R''(0)$. This allows to obtain the following relation:

$$4 - D \leqslant \frac{3-N}{N-1}\,\eta, \tag{13}$$

where η is given by Eq. (9). Since Eq. (13) is incompatible with the requirement $\eta > 0$, there are no accessible fixed points for $N > 3$. This suggests the strong coupling regime with a presumably finite correlation length.

In the RA case a similar consideration uses the connected and disconnected correlation functions of the field $(n_x(\mathbf{r})n_y(\mathbf{r}))$ in presence of Gaussian disorder (3). At $N = 3$ the resulting condition for the critical exponent, $\eta \geqslant \epsilon/2$, rules out all but one fixed points of RG equation (8).

The question of the large-distance behavior of the RF and RA Heisenberg models was discussed by Aharony and Pytte on the basis of an approximate equation of state.[23] They also obtained QLRO in the RA case. However, we believe that this is an accidental coincidence, since the equation of state[23] is valid only in the first order in the strength of the disorder, while higher orders are crucial for critical properties.[24] In particular, the approach of Ref. 23 incorrectly predicts the absence of QLRO in the RF XY model and its presence in the RA spherical model. It also provides incorrect critical exponents in the Heisenberg case.

The RA Heisenberg model is relevant for the amorphous magnets.[2] At the same time, for their large-distance behavior the dipole interaction may be important.[17] Besides, a weak nonrandom anisotropy is inevitably present due to mechanical stresses.

In conclusion, we have found that the random anisotropy Heisenberg model has the infinite correlation length and a power-law dependence of the correlation function of the magnetization on the distance at low temperatures and weak disorder in $4-\epsilon$ dimensions. On the other hand, the correlation length of the random field $O(N>3)$ model is always finite.

The author is thankful to E. Domany, G. Falkovich, M. V. Feigelman, Y. Gefen, S. E. Korshunov, A. I. Larkin, Y. B. Levinson, V. L. Pokrovsky and A. V. Shytov for helpful discussions. This work was supported by RFBR Grant 96-02-18985 and by Grant 96-15-96756 of the Russian Program of Leading Scientific Schools.

*)e-mail: feldman@itp.ac.ru

[1] Y. Imry and S. K. Ma, Phys. Rev. Lett. **35**, 1399 (1975).
[2] R. Harris, M. Plischke, and M. J. Zuckermann, Phys. Rev. Lett. **31**, 160 (1973).
[3] T. Bellini, N. A. Clark, and D. W. Schaefer, Phys. Rev. Lett. **74**, 2740 (1995).
[4] S. V. Fridrikh and E. M. Terentjev, Phys. Rev. Lett. **79**, 4661 (1997).
[5] K. Matsumoto, J. V. Porto, L. Pollak *et al.*, Phys. Rev. Lett. **79**, 253 (1997).
[6] G. Blatter, M. V. Feigelman, V. B. Geshkenbein *et al.*, Rev. Mod. Phys. **66**, 1125 (1994).
[7] A. I. Larkin, Zh. Éksp. Teor. Fiz. **58**, 1466 (1970) [Sov. Phys. JETP **31**, 784 (1970)].

[8] R. A. Pelcovits, E. Pytte, and J. Rudnik, Phys. Rev. Lett. **40**, 476 (1978).
[9] U. Yaron, P. L. Gammel, D. A. Huse *et al.*, Phys. Rev. Lett. **73**, 2748 (1994).
[10] S. E. Korshunov, Phys. Rev. B **48**, 3969 (1993); T. Giamarchi and P. Le Doussal, Phys. Rev. B **52**, 1242 (1995).
[11] M. J. P. Gingras and D. A. Huse, Phys. Rev. B **53**, 15193 (1996).
[12] L. Balents and D. S. Fisher, Phys. Rev. B **48**, 5949 (1993).
[13] M. Mezard and G. Parisi, J. Phys. A **23**, L1229 (1990); J. Phys. (France) **1**, 809 (1991).
[14] D. E. Feldman, JETP Lett. **65**, 114 (1997); Phys. Rev. B **56**, 3167 (1997).
[15] T. Emig and T. Nattermann, Phys. Rev. Lett. **81**, 1469 (1998).
[16] L. Radzihovsky and J. Toner, http://xxx.lanl.gov/abs/cond-mat/9811105.
[17] B. Barbara, M. Coauch, and B. Dieny, Europhys. Lett. **3**, 1129 (1987).
[18] R. Fisch, Phys. Rev. B **57**, 269 (1998); **58**, 5684 (1998); J. Chakrabaty, Phys. Rev. Lett. **81**, 385 (1998).
[19] P. Lacour-Gayet and G. Toulouse, J. Phys. (France) **35**, 425 (1974); S. L. Ginzburg, Zh. Éksp. Teor. Fiz. **80**, 244 (1981) [Sov. Phys. JETP **53**, 124 (1981)]; A. Khurana, A. Jagannathan, and J. M. Kosterlitz, Nucl. Phys. B **240**, 1 (1984); M. V. Feigelman and M. V. Tsodyks, Zh. Éksp. Teor. Fiz. **91**, 955 (1986) [Sov. Phys. JETP **64**, 562 (1986)].
[20] A. M. Polyakov, Phys. Lett. B **59**, 79 (1975); *Gauge Fields and Strings*, Harwood Academic Publishers, Chur, 1987.
[21] D. S. Fisher, Phys. Rev. B **31**, 7233 (1985).
[22] M. Schwartz and A. Soffer, Phys. Rev. Lett. **55**, 2499 (1985).
[23] A. Aharony and E. Pytte, Phys. Rev. Lett. **45**, 1583 (1980).
[24] Y. Y. Goldshmidt, Nucl. Phys. B **225**, 123 (1983).

Published in English in the original Russian journal. Edited by Steve Torstveit.

Negative magnetoresistance in mixed-valence $La_{0.6}Y_{0.1}Ca_{0.3}MnO_3$: Evidence for charge localization governed by the Curie–Weiss law

S. Sergeenkov
SUPRAS, Institute of Physics, B5, University of Liège, B-4000 Liège, Belgium; Bogoliubov Laboratory of Theoretical Physics, Joint Institute for Nuclear Research, 141980 Dubna, Moscow Region, Russia

H. Bougrine
SUPRAS, Institute of Physics, B5, University of Liège, B-4000 Liège, Belgium; SUPRAS, Montefiore Electricity Institute, B28, University of Liège, B-4000 Liège, Belgium

M. Ausloos
SUPRAS, Institute of Physics, B5, University of Liège, B-4000 Liège, Belgium

A. Gilabert
Laboratoire de Physique de la Matière Condensée, Université de Nice-Sophia Antipolis, Parc Valrose F-09016 Nice, Cedex 02, France

(Submitted 23 June 1999)
Pis'ma Zh. Éksp. Teor. Fiz. **70**, No. 2, 136–140 (25 July 1999)

The colossal negative magnetoresistance $\Delta\rho$ observed in $La_{0.6}Y_{0.1}Ca_{0.3}MnO_3$ at $B=1$ T shows an unusual, nearly perfect symmetry (around the peak temperature $T_0=160$ K), suggestive of a Curie–Weiss-dominated transport mechanism in this material both above and below the field-dependent Curie temperature $T_C \equiv T_0$. Attributing this symmetry to strong magnetic fluctuations below T_C (which are triggered by the Y substitution and cause a ''bootstrap'' destruction of the ferromagnetic phase), the data are interpreted in terms of the nonthermal spin hopping and magnetization-dependent charge carrier localization scenario leading to $\Delta\rho=-\rho_s(1-e^{-\gamma M^2})$, with the magnetization $M(T,B)=CB/|T-T_C(B)|^{\nu}$. The separate fits through all the data points above and below T_C yield $C^+\simeq 2C^-$ and $\nu_+\simeq\nu_-\simeq 1$, in agreement with the predictions of the Landau mean-field theory.
 [S0021-3640(99)01314-6]

PACS numbers: 75.30.Vn, 75.30.Kz, 72.15.Rn

Recently interest in the mixed-valence manganite perovskites $R_{1-x}Ca_xMnO_3$ (where R=La,Y,Nd,Pr) has been renewed due to the large negative magnetoresistive (MR) effects observed near the ferromagnetic (FM) ordering of Mn spins.[1–12] In the doping range $0.2<x<0.5$, these compounds are known to undergo a double phase transition from a paramagnetic insulating state to a ferromagnetic metallic state near the Curie temperature T_C. Above $x=0.5$, the specific heat and susceptibility measurements reveal[3,6,8,9] an extra

antiferromagnetic (AFM) canted-like transition at a tempreature T_{AFM} lying below T_C. At the same time, substitution on the La site was found to modify the phase diagram through cation size effects leading toward either charge-ordered or AFM instability.[1–3,6,9] On the other hand, Babushkina *et al.*[1,2] have found that a composition $(La_{1-y}Pr_y)_{0.7}Ca_{0.3}MnO_3$ with $y=0.75$ undergoes a metal–insulator transition even upon a mere isotopic substitution of oxygen. This conclusion has been further corroborated by Balagurov *et al.*,[3] who determined the magnetic structure of this compound (using a neutron diffraction method) and found that substitution of ^{18}O for ^{16}O leads to a modification of the electronic state which correlates both with the observed alteration of the magnetic structure and with the charge ordering process.

At the same time,[6,9] Y substitution is responsible for two major modifications of the parent manganite $La_{0.7}Ca_{0.3}MnO_3$: (i) it lowers the FM Curie temperature T_C, and (ii) it weakens the system's robustness against strong AFM fluctuations (which are developed locally within the ordered FM matrix) by shifting T_C closer to T_{AFM}. The latter is considered[4,10–13] to be the most probable reason for strong magnetic localization of spin-polarized carriers, which in turn results in a hopping-dominated charge carrier transport mechanism below T_C. Above T_C, the resistivity presumably follows a thermally activated Mott-like variable-range hopping law $\rho \propto \exp(T_0/T)^z$ with $1/4 \leqslant z \leqslant 1$.

In this letter we present some typical results for magnetoresistivity (MR) measurements on a manganite sample $La_{0.6}Y_{0.1}Ca_{0.3}MnO_3$ at $B=1$ T field for a wide temperature interval (ranging from 20 K to 300 K) and compare them with the available theoretical explanations. As we shall see, the data are best described in terms of the nonthermal (rather than Mott-like thermally activated) spin hopping scenario with a magnetization-dependent charge carrier localization length $L(M)$ both above and below T_C. The interpretation is essentially based on the assumption of rather strong magnetic fluctuations in this material far beyond the Curie point T_C, which have been found[5] to dominate its magneto-thermopower behavior as well.

The polycrystalline $La_{0.6}Y_{0.1}Ca_{0.3}MnO_3$ samples used in our measurements were prepared from stoichiometric amounts of La_2O_3, Y_2O_3, $CaCO_3$, and MnO_2 powders. The mixture was heated in air at 800 °C for 12 hours to achieve decarbonation and then pressed at room temperature to obtain parallelipedic pellets. An annealing and sintering from 1350 °C to 800 °C was made slowly (during 2 days) to preserve the right phase stoichiometry. A small bar ($10\,\mathrm{mm} \times 4\,\mathrm{mm}^2$) was cut from one pellet. The electrical resistivity $\rho(T,B)$ was measured using the conventional four-probe method. To avoid the Joule and Peltier effects, a dc current $I=1$ mA was injected (in a one-second pulse) successively on the two sides of the sample. The voltage drop V across the sample was measured with high accuracy by a KT256 nanovoltmeter. The magnetic field B of 1 T was applied normal to the current. Figure 1 presents the temperature dependence of the resistivity $\rho(T,B)$ for a $La_{0.6}Y_{0.1}Ca_{0.3}MnO_3$ sample at zero field and at $B=1$ T. The corresponding MR $\Delta\rho(T,B)=\rho(T,B)-\rho(T,0)$ is shown in Fig. 2 as a function of reduced temperature $(T-T_0)/T_0$, with $T_0=160$ K being the temperature at which the negative MR exhibits a minimum. Notice the nearly perfect symmetry of the MR with respect to the left ($T<T_0$) and right ($T>T_0$) wings, thus suggesting a ''universal'' magnetotransport mechanism above and below T_0. Before discussing a probable scenario for the observed MR temperature behavior, let us briefly review the current theoretical models. Several unification approaches have been suggested.[10–13] In essence, all of them are

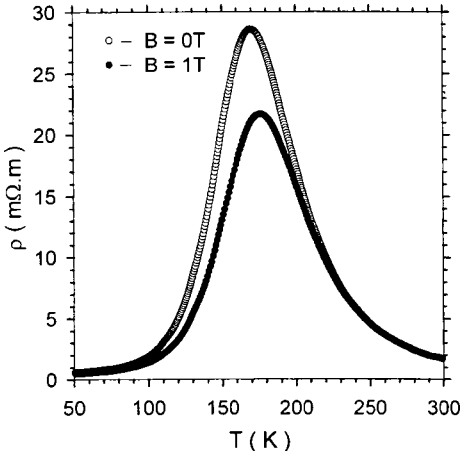

FIG. 1. Temperature behavior of the observed resistivity $\rho(T,B)$ in $La_{0.6}Y_{0.1}Ca_{0.3}MnO_3$ at zero field and at $B=1$ T.

based on a magnetic localization concept which relates the observable MR at any temperature and/or applied magnetic field to the local magnetization. In particular, one of the most advanced models of this kind[10] ascribes the metal–insulator (M–I)-like transition to a modification of the spin-dependent potential $J_H\mathbf{s}\cdot\mathbf{S}$ associated with the onset of magnetic order at T_C (here $J_H \simeq 1eV$ is the on-site Hund's-rule exchange coupling of an e_g electron with $s=1/2$ to the localized Mn t_{2g} ion core with $S=3/2$). Specifically, the hopping based conductivity reads

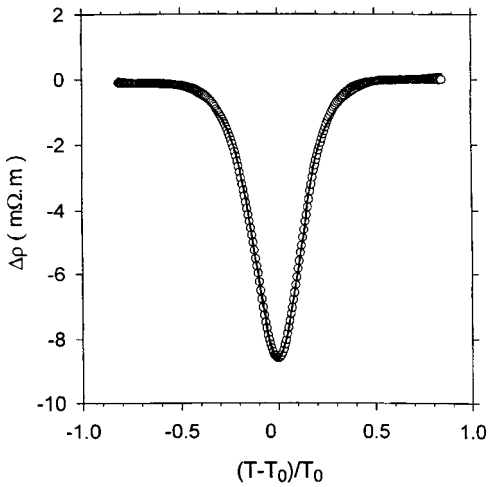

FIG. 2. Dependence of the observed MR $\Delta\rho(T,B)=\rho(T,B)-\rho(T,0)$ in $La_{0.6}Y_{0.1}Ca_{0.3}MnO_3$ at $B=1$T as a function of $(T-T_0)/T_0$, with $T_0=160$ K being the temperature at which the MR reaches its minimum. The solid line through all the data points is the best fit according to Eq. (3).

$$\sigma=\sigma_m\exp\left(-\frac{2R}{L}-\frac{W_{ij}}{k_BT}\right), \tag{1}$$

where

$$\sigma_m=e^2R^2\nu_{\rm ph}N(E_m). \tag{2}$$

Here R is the hopping distance (typically[10] of the order of 1.5 unit cells), L is the charge carrier localization length (typically[12] $L\simeq 2R$), $\nu_{\rm ph}$ is the phonon frequency, $N(E_m)$ is the density of available states at the magnetic energy $E_m\simeq J_H$, and W_{ij} is the effective barrier between the hopping sites i and j. There are two possible ways of introducing an explicit magnetization dependence into the above model: either by modifying the hopping barrier $W_{ij}\to W_{ij}-\alpha\mathbf{M}_i\cdot\mathbf{M}_j$ or by assuming a magnetization-dependent localization length $L(M)$. The first scenario (suggested by Viret *et al.*[10]) results in a thermally activated behavior of MR over the whole temperature range. Indeed, since a sphere of radius R contains $(4/3)\pi R^3/v$ sites, where $v=5.7\times 10^{-29}\,\mathrm{m}^3$ is the lattice volume per manganese ion, the smallest value of W_{ij} is therefore $[(4/3)\pi R^3N(E_m)]^{-1}$. Minimizing the hopping rate, one finds that the resistivity should vary as $\ln(\rho/\rho_0)=[T_0\{1-(M/M_s)^2\}/T]^{1/4}$. This scenario was used by Wagner *et al.*[12] to interpret their MR data on low-conductive $Nd_{0.52}Sr_{0.48}MnO_3$ films. Assuming the molecular-field result for the magnetization, they found that their data scale with the Brillouin function $\mathcal{B}$ in the ferromagnetic state and follow a $\mathcal{B}^2$ dependence in the paramagnetic state. Unfortunately, all attempts to fit our MR data with the above thermally activated hopping formula have failed. In our case the observed MR seems to follow a steeper temperature behavior exhibiting a remarkable symmetry around T_0. Instead, we were able to successfully fit our data for the whole temperature interval with

$$\Delta\rho(T,B)=-A[1-e^{-\beta(T)}], \tag{3}$$

where

$$\beta(T)=\beta_0\left[\frac{T_0}{T-T_0}\right]^{2\nu}, \tag{4}$$

and A, β_0, and ν are temperature-independent parameters. The separate fits for our MR data above and below $T_0=160\,\mathrm{K}$ produce $A=0.873\pm 0.001\,\Omega\cdot\mathrm{cm}$, $\beta_0^+=0.015\pm 0.001$, $\beta_0^-=0.004\pm 0.001$, $\nu^+=1.16\pm 0.01$, and $\nu^-=1.12\pm 0.01$, in agreement with the observed symmetry. This suggests us to interpret our findings in terms of a nonthermal localization scenario,[4,5,13] which emphasizes the role of a nonmagnetic disorder and assumes a magnetization dependence of the localization length $L(M)$ (rather than hopping barrier W_{ij}) which diverges at the M–I phase transition. Within this scenario, the Curie point T_C is defined in terms of the Curie–Weiss susceptibility $\chi=C/(T_C-T)$ as $\chi^{-1}(T_C,B)=0$, while the M–I transition temperature $T_{\rm MI}$ is such that $M(T_{\rm MI},B)=M_0$ [with M_0 being a fraction of the saturated magnetization M_s). In terms of the spontaneous magnetization M, it means that for $M<M_0$ the system is in a highly resistive (insulator-like) phase, while for $M>M_0$ the system is in a low resistive (metallic-like) state. Adopting this scenario (with $W_{ij}/k_BT\ll 2R/L$, see Eq. (1)], we can write $\rho(T,B)=\rho_0(T)+\rho_m\exp[2R/L(M)]$ for the field-induced resistivity in our sample. Here, $\rho_0(T)$ is a field-independent background resistivity, $\rho_m=1/\sigma_m$, and the localization length $L(M)$

depends on the field and temperature through the corresponding dependences of the magnetization $M(T,B)$. Assuming after Sheng *et al.*[13] that $L(M)=L_0/(1-M^2/M_0^2)$, we arrive at the following simple expression for the MR

$$\Delta\rho(T,B)=-\rho_s[1-e^{-\gamma M^2(T,B)}], \tag{5}$$

where $\gamma=2R/L_0M_0^2$, and $\rho_s=\rho(T,0)-\rho_0(T)$ is the temperature-independent residual resistivity.[12] To account for the observed symmetry of the MR around T_0, we identify T_0 with the Curie temperature $T_C(B)$ at a finite magnetic field B, and assume that the field and temperature dependence of the magnetization is governed by the same Curie–Weiss like law $M(T,B)=\chi^{\pm}(T,B)B$ with $\chi^{\pm}(T,B)=C^{\pm}/|T-T_C|^{\nu_{\pm}}$ above $(+)$ and below $(-)$ T_C, respectively. Given the above definitions, we obtain $|T_C(B)-T_{\rm MI}|^{\nu_-}=C^-B/M_0$ for the difference between the two critical temperatures, which implies that within the Curie–Weiss scenario, $T_{MI}\equiv T_C(0)$. Thus, in agreement with the Landau theory of second-order phase transitions (see, e.g., Landau and Lifshitz,[14] Chapter V), below $T_C(B)$ the Curie–Weiss law exists in the form of the ''generalized susceptibility'' $\chi^-(T,B)\propto 1/B$, leading to a nonzero value of the spontaneous magnetization M even at zero magnetic field. Finally, by comparing Eq. (5) with the above-used fitting formula [see Eq. (3)], we arrive at the following relations between the fitting and model parameters, viz., $A=\rho_s$, $\beta_0^-=(2R/L_0)[1-T_C(0)/T_C(B)]^{2\nu_-}$, and $C^+/C^-T_0^{\phi}\sqrt{\beta_0^+/\beta_0^-}$, with $\phi=\nu_+-\nu_-$, and $T_0=\ =T_C(B)$. Taking into account the zero-field Curie temperature $\nu_{\pm}$ for this material,[5] we obtain $2R/L_0\simeq 1$ for the ratio of hopping distance to localization length, and $C^+/C^-=\ =1.98\pm 0.01$ for the ratio of Curie constants above and below T_C, in accordance with the mean-field theory predictions.[14] Furthermore, using the former ratio and the value obtained for the residual resistivity, $\rho_s\simeq 0.873\,\Omega\cdot$cm, we get an estimate for the hopping distance R, provided the density of states $N(E_m)$ and the phonon frequency $\nu_{\rm ph}$ are known. Assuming[10] that $N(E_m)\simeq 9\times 10^{26}{\rm m}^{-3}{\rm eV}^{-1}$ and $\nu_{\rm ph}\simeq 2\times 10^{13}{\rm s}^{-1}$ (estimated from Raman shift for Mn–O optical modes)[12] for these two parameters, we arrive at a reasonable value of $R\simeq 5.5$Å, which in turn results in $L_0\simeq 11$ Å for the zero-temperature, zero-field carrier charge localization length, in good agreement with the other reported[4–6,10,12] estimates of this parameter.

In conclusion, we would like to comment on the plausibility of our interpretation, which is essentially based on the Curie–Weiss behavior of the magnetization. Clearly the possibility of using the Curie–Weiss law (which is usually limited to the critical region around T_C) throughout the whole region (ranging from the paramagnetic to the ferromagnetic state) suggests the presence of strong fluctuations both above and below T_C. To account for a possible source of these fluctuations, we turn to the magnetic structure of our sample. As we mentioned in the introductory part, along with lowering the Curie point, Y substitution brings about another important effect. Namely, it drives the magnetic structure closer to a canted AFM phase (which occurs at $T_{\rm AFM}<T_C$),[9] thus triggering the development of local AFM fluctuations within the parent FM matrix. In turn, these fluctuations cause a trapping of spin-polarized carriers in a locally FM environment, leading to hopping-dominated transport of charge carriers between the spin polarons thus formed, over the whole temperature interval. Besides, according to Jaime *et al.*,[6] polaronic distortions in the PM phase of these manganites should inevitably persist in the FM phase (below T_c) as well, where there remain significant indications of spin scatter-

ing due to the collapse of large polarons in the FM state, which reduces the effective exchange coupling via the double exchange mechanism, causing a ''bootstrap'' destruction of FM and triggering the concomitant M–I transition.

We thank J. C. Grenet and R. Cauro (University of Nice-Sophia Antipolis) for lending us the sample. Part of this work has been financially supported by the Action de Recherche Concertées 94-99/174. M. A. and A. G. thank CGRI for financial support through the TOURNESOL program. S. S. thanks FNRS (Brussels) for some financial support.

[1] N. A. Babushkina, L. M. Belova, O. Yu. Gorbenko *et al.*, Nature (London) **391**, 159 (1998).
[2] N. A. Babushkina, L. M. Belova, V. I. Ozhogin *et al.*, J. Appl. Phys. **83**, 7369 (1998).
[3] A. M. Balagurov, V. Yu. Pomyakushin, D. V. Sheptyakov *et al.*, JETP Lett. **69**, 50 (1999).
[4] S. Sergeenkov, H. Bougrine, M. Ausloos *et al.*, JETP Lett. **69**, 858 (1999).
[5] S. Sergeenkov, H. Bougrine, M. Ausloos *et al.*, Phys. Rev. B (in press).
[6] M. Jaime, M. B. Salamon, M. Rubinstein *et al.*, Phys. Rev. B **54**, 11914 (1996).
[7] J. Fontcuberta, V. Laukhin, and X. Obradors, Appl. Phys. Lett. **72**, 2607 (1998).
[8] H. Y. Hwang, S-W. Cheong, P. G. Radaelli *et al.*, Phys. Rev. Lett. **75**, 914 (1995).
[9] A. P. Ramirez, J. Phys.: Condens. Matter **9**, 8171 (1997).
[10] M. Viret, L. Ranno, and J. M. D. Coey, Phys. Rev. B **55**, 8067 (1997).
[11] L. P. Gor'kov and V. Z. Kresin, JETP Lett. **67**, 985 (1998).
[12] P. Wagner, I. Gordon, L. Trappeniers *et al.*, Phys. Rev. Lett. **81**, 3980 (1998).
[13] L. Sheng, D. Y. Xing, D. N. Sheng *et al.*, Phys. Rev. Lett. **79**, 1710 (1997).
[14] L. D. Landau and E. M. Lifshitz, *Electrodynamics of Continuous Media*, Pergamon Press, Oxford, 1960.

Published in English in the original Russian journal. Edited by Steve Torstveit.

Measurement of the state of an individual spin using a ''turnstile''

S. N. Molotkov and S. S. Nazin
Institute of Solid State Physics, Russian Academy of Sciences, 142432 Chernogolovka, Moscow Region, Russia

(Submitted 22 June 1999)
Pis'ma Zh. Éksp. Teor. Fiz. **70**, No. 2, 141–147 (25 July 1999)

A scheme is proposed for measuring the state of an individual spin (system of spins). The scheme is based on the idea of a single-electron ''turnstile'' and the injection of single spin-polarized electrons from the magnetic metallic borders. Applications to the recently proposed scheme of quantum spin gates based on a silicon matrix are discussed (B. E. Kane, Nature **393**, 133 (1998)). © *1999 American Institute of Physics.* [S0021-3640(99)01414-0]

PACS numbers: 75.10.Jm, 03.65.Bz

After the discovery of efficient quantum algorithms[1] and a rigorous proof of the possibility of quantum computations[2] which are stable against errors, various implementations of quantum logic gates started to appear: based on cold ions,[3] nuclear magnetic resonance,[4] optics,[5] semiconductor nanostructures,[6] and the Josephson effect.[7] The idea of creating quantum gates based on a silicon matrix[8] with embedded donor P^{31} impurity atoms was recently advanced. The nuclear spin and the electron spin of the P^{31} atom play the role of quantum bits. One of the unclear aspects of the scheme of Ref. 8 is the measurement of the state of an individual nuclear or electron spin (or both together). The idea of indirect detection of the spin state using a single-electron transistor has been discussed in Refs. 9 and 10. The proposed schemes do not permit detecting directly the state of an individual spin, but rather they measure only different charge states of the system of electronic and nuclear spins.

Detection of an individual spin in itself is not exotic. The first observation of the Larmor precession of an individual spin localized on a $Si(111)7\times7$ surface in an ultrahigh vacuum, using a scanning tunneling microscope (STM), was demonstrated by an IBM group (see Refs. 11 and 12) ten years ago. There were also reports of the detection in the STM current of an electronic paramagnetic resonance signal from an individual spin in an organic molecule.[13] It has also been demonstrated that the STM with a magnetic probe is sensitive at the atomic level to the state of individual spins on the surfaces of magnetic materials.[14] The measured quantity in an STM is the tunneling current, which on atomic scales depends on the position of the probe along the surface. For a magnetic probe the tunneling current contains a spin-dependent component[12]

$$I_t(\mathbf{x}) \propto \rho_c(\mathbf{x})\rho_t \mathbf{m}_c(\mathbf{x})\cdot\mathbf{m}_t,$$

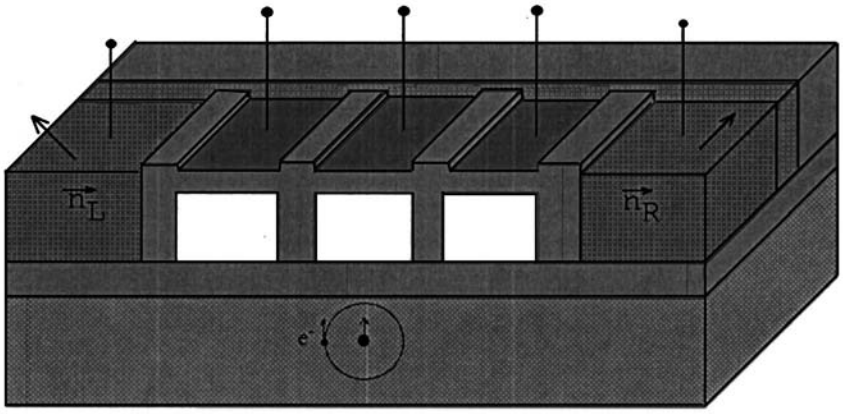

FIG. 1.

where $\rho_{c,t}(\mathbf{x})$ are the local densities of states at the probe tip and on the surface, and $\mathbf{m}_c(\mathbf{x})$ and $\mathbf{m}_t$ are the local magnetizations on the surface at the point $\mathbf{x}$ and at the probe tip. However, current measurements in the stationary state are not directly suitable for applications to the states of quantum gates.

To implement quantum gates it is necessary to know how to perform measurements on a system at an arbitrary point in time. According to the general quantum-mechanical measurement theory,[15–17] the most complete description of any specific measuring procedure to which a quantum-mechanical system can be subjected is given by the so-called instrument $T(d\lambda)$ consisting of the mapping of the states of the system ρ_s (density matrices) prior to measurement into the density matrix $\overline{\rho_s}=T(d\lambda)\rho_s$ (to within the normalization) of the system immediately after the measurement, which has given a result near $d\lambda$ (the probability of obtaining the result near $d\lambda$ is $\mathrm{Tr}\widetilde{\rho}_s=\mathrm{Tr}\,\{T(d\lambda)\rho_s\}$). It is known that any instrument can be represented in the form

$$T(d\lambda)\rho_s=\mathrm{Tr}_A\{(I_s\otimes M_A(d\lambda))U(\rho_s\otimes\rho_A)U^{-1}\},$$

i.e., any measurement can be realized by attaching to the system of interest an ancillary system in a fixed state ρ_A (A denotes ancilla), the combined unitary evolution (U) of both systems for a certain period of time, and then a measurement, generated by a certain decomposition of unity $M_A(d\lambda)$, on the ancillary system.

In what follows a method is proposed for detecting the state of an individual spin (or a system of spins, for example, nuclear spin + electron spin). The method is based on the idea of a ''turnstile.''[18,19] In this scheme the following are present explicitly: preparation of the ancillary system (ρ_A) at an arbitrary moment in time, switching on of the interaction between ρ_A and ρ_s, combined unitary evolution, switching off of the interaction at an arbitrary time, and detection of the state of the ancillary system.

Let us examine a model system. Let the system consist of spins beneath the surface, for example, an atom with nuclear spin and an electron localized on the nuclear spin (Fig. 1). Let there also be a system of tunneling-coupled quantum dots on the surface such that the central dot is located above the spin system playing the role of quantum bits (Figs. 1

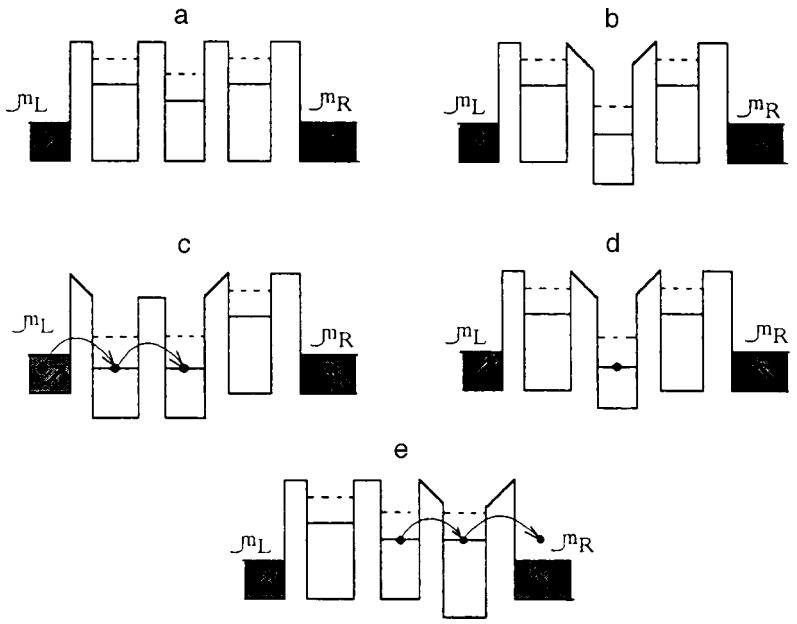

FIG. 2.

and 2). One size-quantized level is present in each quantum dot. The outer dots are coupled by a tunneling coupling with metallic magnetic electrodes (Figs. 1 and 2).

The Hamiltonian of quantum dots tunneling-coupled with the borders and with one another can be represented in the form

$$H=\sum_{k,\sigma,\alpha=L,R}\varepsilon_{k\sigma\alpha}a^{+}_{k\sigma\alpha}a_{k\sigma\alpha}+\sum_{\sigma}\left(\varepsilon_c c^{+}_{c\sigma}c_{c\sigma}+\varepsilon_L c^{+}_{L\sigma}c_{L\sigma}+\varepsilon_R c^{+}_{R\sigma}c_{R\sigma}\right)$$

$$+\sum_{k\sigma}\left(T_{kL}c^{+}_{L\sigma}a_{k\sigma L}+T_{cL}c^{+}_{c\sigma}c_{L\sigma}+T_{cR}c^{+}_{c\sigma}c_{R\sigma}+\text{ h.c.}\right)$$

$$+\sum_{\sigma}\left(U_L n_{L\sigma}n_{L-\sigma}+U_c n_{c\sigma}n_{c-\sigma}U_r n_{R\sigma}n_{R-\sigma}\right), \tag{1}$$

where the first two terms describe the states of the electrons in the isolated borders and dots, the third term describes the tunneling coupling between the borders and the dots, and the last term describes the Coulomb repulsion in the dots (if it is substantial). We assume that the electrons in the borders are in a spin-polarized state and that the magnetization vector in the borders has directions $\mathbf{n}_L$ and $\mathbf{n}_R$, respectively, and is fixed, for example, by the magnetic anisotropy. If the system is in an external magnetic field, then this field must be added to the Hamiltonian. The Hamiltonian of the spin system (quantum gate), for example, for the situation nuclear spin + electron spin localized on the nuclear spin, can be represented in the form

$$H_s=\sum_{\sigma}\ \varepsilon_s c^{+}_{s\sigma}c_{s\sigma}+g_s\mu_B c^{+}_{s\sigma}c_{s\sigma'}\boldsymbol{\sigma}_{\sigma\sigma'}\cdot\mathbf{H}+g_I\mu_B\mathbf{I}\cdot\mathbf{H}+g_{sI}\mathbf{I}\cdot\boldsymbol{\sigma}_{\sigma\sigma'}c^{+}_{s\sigma}c_{s\sigma'}\,. \tag{2}$$

In a magnetic field the contribution from the metallic electrodes must be taken into account. The Hamiltonian of the interaction of the spins in a quantum gate with the electron localized in a central dot (see below) depends on the specific geometry of the structure. For example, if the electron wave functions in the central dot and at the center can overlap, then the Hamiltonian can be written in the form

$$H_{\rm int}=\sum_{\sigma}\ (t_{sc}c^{+}_{s\sigma}c_{c\sigma}+\text{h.c.})+g_{cI}\mathbf{I}\cdot\boldsymbol{\sigma}_{\sigma\sigma'}c^{+}_{c\sigma}c_{c\sigma'}+\sum_{\sigma}\ U_{sc}n_{c\sigma}n_{s-\sigma}\,. \tag{3}$$

If the overlap is negligible, then only the dipole–dipole interaction should be retained.

The complete solution of the temporal evolution of the system is a nontrivial problem. To make progress we must assume a definite hierarchy of times for various processes occurring in the system. Let $\tau_{\rm res}$ be the characteristic tunneling time into a border from the central dot when the levels in the neighboring quantum dots are put in resonance (this time is the same as the tunneling time, for example, from the left-hand well into the border through one barrier); let $\tau_{\rm non}$ be the characteristic tunneling time into the border from the central dot when the levels in the dots are taken out of resonance; and, let $\tau_{\rm dyn}$ be the characteristic time of combined evolution as a result of the interaction of an electron in the central dot and the spins in the gate. We shall assume that $\tau_{\rm res}\ll\tau_{\rm dyn}\ll\tau_{\rm non}$. In what follows we shall use the well-known fact that for tunneling through two barriers (from the central dot into one of the borders) with the levels in resonance the additional smallness associated with the additional barrier is removed. The characteristic times are inversely proportional to the level width and depend on the position of the level. The times can be estimated using the relations (see, for example, Ref. 19)

$$\frac{1}{\tau(\omega)}=\gamma(\omega)=\frac{|T_{Lc}|^2\gamma_0^2}{[\tilde{\varepsilon}_c(\omega)-\tilde{\varepsilon}_L(\omega)]^2+\gamma_0^2},\qquad \gamma_0=\sum_k\ |T_{kL}|^2\delta(\omega-\varepsilon_{kL})=|T_L|^2.$$

Here $\gamma_0=|T_L|^2\approx|T_{cL}|^2=|T|^2$ is the initial tunneling transmittance of the barriers between wells and between the wells and borders, which without loss of generality can be assumed to be the same. In resonance $(\tilde{\varepsilon}_c(\omega_r)=\tilde{\varepsilon}_L(\omega_r))$ $1/\tau_{\rm res}\approx|T|^2=\gamma_0$. When the levels leave resonance by an amount greater than the level width $(\Delta\gg\gamma_0)$, the characteristic time becomes $t/\tau_{\rm non}\approx\gamma_0(\gamma_0^2/\Delta^2)\ll 1/\tau_{\rm res}$. Taking the Coulomb repulsion into account does not qualitatively change the situation.

We shall now discuss the different stages of the measuring procedure (Fig. 2):

a) At first the size-quantized levels in the quantum dots are unoccupied (they lie above the chemical potentials in the borders). The dashed lines show the levels in the dots that are split off by the Coulomb interaction.

b,c) Voltage pulses are applied to the central and left-hand dots at times τ $(\tau_{\rm res}\ll\tau\ll\tau_{\rm dyn})$ so that the levels at the points L and c are brought into resonance and drop below the chemical potential μ_L in the left-hand border. Over the time $\tau_{\rm res}$ the levels in the left-hand and central dots are filled with electrons from the left-hand border.

d) Next, a voltage pulse is applied at times $\tau_{\rm res}\ll\tau\ll\tau_{\rm dyn}$ to the left-hand dot. This pulse moves the level in the dot above the chemical potential μ_L. Over the characteristic

time τ_{res} the level of the left-hand well is emptied because the electron goes back into the left-hand border. The level in the central dot remains filled. At times $<\tau_{\text{non}}$ it can be assumed that the electron has ''forgotten'' the borders and is isolated, its spin state being determined by the state of the left-hand border. This procedure results in the preparation initially (instantaneously against the background of $\tau \ll \tau_{\text{dyn}}$) of an ancillary quantum system in the state $\rho_A(t=0)$. Since the density matrix for spin 1/2 can always be represented in the form $\rho = 1/2(I+\boldsymbol{\sigma}\cdot\mathbf{u})$, the state of an electron arriving in the central dot from the left-hand border is described by the density matrix $\rho_A(t=0)=(1/2)(I+\boldsymbol{\sigma}\cdot\mathbf{u}_L)$, where $\mathbf{u}_L$ is a vector describing the direction and degree of polarization of the electrons in the left-hand border. Next, it can be assumed that at times $\tau_{\text{res}} \ll \tau \ll \tau_{\text{non}}$ combined quantum dynamics of an electron in the central dot and the spins in the gate occurs as described by the unitary evolution

$$\tilde{\rho}(t) = U(t)(\rho_A(t=0)\otimes\rho_s(t=0))U^{-1}(t), \quad U(t)=\exp\left(i\int_0^t H_{\text{int}}(t')dt'\right).$$

Here $\rho_s(t=0)$ is the density matrix of the quantum gate at time $t=0$. Diagonalization of the Hamiltonian H_{int} presents no difficulties, since this Hamiltonian describes a finite-dimensional system (for example, the combined dynamics of an electron in a dot + a nuclear spin + an electron localized on the nuclear spin requires diagonalizing an 8×8 matrix). The density matrix of an electron in the central well by the time t after combined evolution is

$$\rho_A(t) = \text{Tr}_s\{U(t)(\rho_A(t=0)\otimes\rho_s(t=0))U(t)^{-1}\} = \frac{1}{2}(I+\boldsymbol{\sigma}\cdot\mathbf{u}_A(t)),$$

where the vector $\mathbf{u}_A(t)$ gives the spin that an electron in the central dot acquired by the time t as a result of interaction with the spins in the gate.

e) Detection of the state of an electron in the central well is performed by measuring the current flowing into the right-hand border. For this, voltage pulses are applied for time τ_1 to the central and right-hand quantum dots (see Fig. 2e), similarly to the way this was done when an electron was injected from the left-hand border. If the time τ_1 is short is compared with τ_{res}, then the probability that the electron escapes into the right-hand border will be proportional to τ_1. Since $\tau_{\text{dyn}} \gg \tau_{\text{res}}$, the interaction between the ancillary system and the quantum gate is switched off virtually instantaneously (against the background of the combined dynamics) at time t. The probability of an electron escaping into the right-hand border per unit time is, to within numerical factors,

$$\text{Pr} \propto |T|^2 \text{Tr}_{sA}\{\rho_R\cdot\rho_a(t)\} = |T|^2 \text{Tr}_{sA}\{(I_s\otimes\rho_R)(U(t)(\rho_s(t=0)\otimes\rho_A(t=0))U^{-1}(t))\},$$

where $\rho_R = 1/2(I+\boldsymbol{\sigma}\cdot\mathbf{u}_R)$ is the density matrix of electrons in the right-hand border. This means that the probability of a current pulse appearing in the right-hand border depends on the spin state of an electron in the central quantum dot:

$$\text{Pr} = C\tau_1\cdot|T|^2\{1+\mathbf{u}_R\cdot\mathbf{u}_A(t)\}, \tag{4}$$

where C is a constant (the scalar product arises because the wave functions of two spinors in the dot and the right-hand border are matched; it is necessary to use a common quantization axis for the spin[20]).

f) Finally, voltage pulses of magnitude such that an electron from the central dot, if it has not been transferred into the right-hand border as a result of the operation e, would depart into the left-hand border with probability 1, are applied to the central and left-hand quantum dots at a certain time.

We denote the total duration of the cycle consisting of the operations a–f by τ_0. Then for fixed τ_1 a current $\Pr \cdot e/\tau_0$ will flow through the system of quantum dots. The value of the constant C in Eq. (4) can be determined by measuring the current for the case of polarizations with the same direction in the left-hand and right-hand borders with the interaction with the gate switched off ($t=0$), when $\mathbf{u}_R(t)\cdot\mathbf{u}_A(t)=|\mathbf{u}_R|\cdot|\mathbf{u}_L|$ (we assume that the degrees of polarization $|\mathbf{u}_R|$ and $|\mathbf{u}_L|$ in the borders are known).

Thus, the polarization vector $\mathbf{u}_A(t)$ of the ancillary system, which depends on the initial state ρ_s of the gate prior to the measurement, can be reconstructed by measuring the current using the scheme described above. Generally speaking, to reconstruct completely the state of the gate from the measured current it is necessary to know how to compute all three components of the vector $\mathbf{u}_s$ determining the density matrix of the gate. It is obvious that for this it is necessary to measure the current for at least three different combinations of the parameters of the system. For example, the direction of magnetization in both borders and the interaction time of the ancillary system with the gate can be changed. However, the question of whether or not information about the behavior of the tunneling current as a function of the indicated parameters is sufficient for complete reconstruction of the vector $\mathbf{u}_s$ must be solved separately for each specific interaction Hamiltonian between the ancillary system and the gate.

The characteristic nonresonant tunneling time can be made quite long by increasing the width of the double barrier, so that this time is not a limitation. The characteristic time of the combined quantum dynamics of an electron in the central dot and the gate can be estimated as a time of the order of the dynamics of an isolated gate. The latter is the reciprocal of the Larmor spin precession frequency in an external magnetic field.[8] In a field $B\approx 100$ G (0.01 T) it is $1/\tau_{\rm dyn}\approx 10^6$ Hz. The resonant tunneling time can easily be adjusted to $\tau_{\rm res}\approx 10^{-9}$ s, which in principle makes it possible to perform a measurement of the current pulses at times $\tau\leqslant\tau_{\rm res}$. The temperature must not exceed 1 mK, so that at least the Zeeman splitting would not be washed out by the temperature. As the working temperature increases, $\tau_{\rm dyn}$ and correspondingly $\tau_{\rm res}$ decrease and the measurement time of the current pulses decreases. We note that quantum dots, like the silicon matrix,[8] must be made of isotopes without nuclear spin; this requirement precludes the use of technology developed on the basis of GaAs/GaAlAs materials and necessitates systems based on Si/SiGe.

We thank K. A. Valiev for a discussion of the results. This work was supported by the Russian Fund for Fundamental Research (Project No. 98-02-16640), by Project No. 02.04.5.2.40.T.50 of the program ''Promising Technologies and Micro- and Nanoelectronics Devices,'' and the program ''Surface Atomic Structures'' (Project No. 1.1.99).

[1] P. W. Shor, *Proceedings of the 35th Annual Symposium on the Foundations of Computer Science*, Santa Fe, NM, USA, edited by S. Goldwasser (IEEE Comput. Soc. Press, Los Alamitos, 1994), p. 124.
[2] A. Yu. Kitaev, Usp. Mat. Nauk **52**(6), 53 (1997).
[3] J. I. Cirac and P. Zoller, Phys. Rev. Lett. **74**, 4091 (1995).
[4] N. A. Gehenfeld and I. L. Chuang, Science **275**, 350 (1997); D. G. Cory, M. D. Price, and T. F. Havel, Physica D **120**, 82 (1998).

[5] Q. A. Turchette *et al.*, Phys. Rev. Lett. **75**, 4710 (1995); G. J. Milburn, Phys. Rev. Lett. **62**, 2124 (1989).
[6] A. Barenco, D. Deutsch, A. Ekert, and R. Jozsa, Phys. Rev. Lett. **74**, 4083 (1995); S. N. Molotkov, JETP Lett. **64**, 237 (1996).
[7] A. Shnirman, G. Schön, and Z. Hermon, Phys. Rev. Lett. **79**, 2371 (1997); L. B. Ioffe, V. B. Geshkenbein, M. V. Feigel'man *et al.*, Nature (London) **398**, 679 (1999).
[8] B. E. Kane, Nature (London) **393**, 133 (1998).
[9] B. E. Kane, N. S. McAlpine, A. S. Dzurak *et al.*, xxx.lanl.gov/abs/cond-mat/9903371.
[10] R. Vrijen, E. Yablonovich, Kang Wang *et al.*, xxx.lanl.gov/abs/quant-ph/9905096.
[11] Y. Manassen, R. J. Hamers, J. E. Demuth, and A. J. Castellano Jr., Phys. Rev. Lett. **62**, 2513 (1989).
[12] S. N. Molotkov, Surf. Sci. **264**, 235 (1992); **261**, 7 (1992); **302**, 235 (1994); JETP Lett. **55**, 173 (1992); **59**, 190 (1994).
[13] A. W. McKinnon and M. E. Weland, *Abstracts of STM'91, International Conference on Scanning Tunneling Microscopy*, Interlaken, 1991, p. 51.
[14] I. V. Shets, R. Wiesendanger, D. Brúgler *et al.*, J. Appl. Phys. **71**, 5496 (1992); R. Wiesendanger, H.-J. Gúntherodt, G. Gúntherodt, and R. Ruf, Phys. Rev. Lett. **65**, 247 (1990); M. W. Prins, R. Jansen, and H. van Kempen, Phys. Rev. B **53**, 8105 (1996).
[15] A. S. Kholevo, *Probabilistic and Statistical Aspects of the Quantum Theory* [in Russian] (Nauka, Moscow, 1980).
[16] K. Kraus, *States, Effects and Operations* (Springer-Verlag, Berlin, 1983).
[17] P. Busch, M. Grabowski, and P. J. Lahti, *Operational Quantum Physics*, Springer Lecture Notes in Physics (1995), Vol. 31.
[18] *Proceedings of the NATO ASI on Single Charge Tunneling*, edited by H. Grabert and M. H. Devoret, March, 1991 (Plenum, New York, 1992).
[19] S. N. Molotkov and S. S. Nazin, JETP Lett. **58**, 279 (1993).
[20] S. N. Molotkov and S. S. Nazin, Zh. Éksp. Teor. Fiz. **107**, 1232 (1995) [JETP **80**, 686 (1995)].

Translated by M. E. Alferieff

Semiclassical limit for Chern–Simons theory on compact hyperbolic spaces

A. A. Bytsenko*)
St. Petersburg State Technical University, 195251 St. Petersburg, Russia; Departamento de Fisica, Universidade Estadual de Londrina, Caixa Postal 6001, Londrina-Parana, Brazil

M. C. Falleiros†) and A. E. Gonçalves‡)
Departamento de Fisica, Universidade Estadual de Londrina, Caixa Postal 6001, Londrina-Parana, Brazil

(Submitted 23 June 1999)
Pis'ma Zh. Éksp. Teor. Fiz. **70**, No. 2, 65–69 (25 July 1999)

The invariant integration method for Chern–Simons theory defined on compact hyperbolic spaces of the form $\Gamma\backslash\mathbb{H}^3$ is verified in the semiclassical approximation. The semiclassical limit for the partition function is calculated. The contribution to the sum over topologies in three-dimensional quantum gravity is briefly discussed. © *1999 American Institute of Physics.* [S0021-3640(99)00114-0]

PACS numbers: 11.15.−q, 02.40.−k

INTRODUCTION

It is known that topological invariants associated with 3-manifolds can be constructed within the framework of Chern–Simons gauge theory.[1] These values were specified in terms of the axioms of topological quantum field theory,[2] whereas an equivalent derivation of invariants was also given combinatorially in Refs. 3 and 4, where modular Hopf algebras related to quantum groups were used. The Witten's (topological) invariants have been explicitly calculated for a number of 3-manifolds and gauge groups.[5–11] The semiclassical approximation for the Chern–Simons partition function $\mathfrak{W}(k)$ can be given by the asymptotic $k\to\infty$ of Witten's invariant of a 3-manifold M and a gauge group G. Typically this expression is a partition function of a quadratic functional.

This note is an extension of the previous paper.[12] Our aim here will be to use the invariant integration method[13,14] in its simplest form for the semiclassical approximation for Chern–Simons theory, defined on hyperbolic 3-manifolds of the form $M=\Gamma\backslash\mathbb{H}^3$, where $\mathbb{H}^3$ is the Lobachevsky space and Γ is a co-compact discrete group of isometries (see Ref. 15 for details).

THE SEMICLASSICAL APPROXIMATION FOR THE PARTITION FUNCTION

The semiclassical approximation for the partition function. The partition function associated to Chern–Simons gauge theory has the form

$$\mathfrak{W}(k)=\int \mathcal{D}A\,\exp[ikCS(A)],\quad k\in\mathbb{Z}, \tag{1}$$

where

$$CS(A)=\frac{1}{4\pi}\int_M \mathrm{Tr}\left(A\wedge dA+\frac{2}{3}A\wedge A\wedge A\right). \tag{2}$$

The quantity $\mathfrak{W}(k)$ is a (well-defined) topological invariant of M. The formal integration in (1) is over the gauge fields A in a trivial bundle, i.e., 1-forms on a 3-dimensional manifold M with values in Lie algebra $\mathbf{g}$ of gauge group G.

In the limit $k\to\infty$ Eq. (1) is given by its semiclassical approximation, involving only partition functions of quadratic functionals:[1]

$$\sum_{[A_f]}\exp[ikCS(A_f)]\int \mathcal{D}B\,\exp\left(\frac{ik}{4\pi}\int_M \mathrm{Tr}(B\wedge d_{A_f}B)\right). \tag{3}$$

In Eq. (3) the sum is taken over representatives A_f for each point $[A_f]$ in the moduli space of flat gauge fields on M. In addition, B is a Lie-algebra-valued 1-form and d_{A_f} is the covariant derivative determined by A_f, namely $d_{A_f}B=dB+[A_f,B]$.

We shall use the invariant integration method,[13,14] which enables the partition functions in Eq. (3) to be evaluated in complete generality. Let M be a compact oriented Riemannian manifold without boundary, and $n=2m+1=\dim M$ is the dimension of the manifold. Let $\chi:\pi_1(M)\mapsto O(V,\langle\cdot,\cdot\rangle_V)$ be a representation of $\pi_1(M)$ on real vector space V. The mapping χ determines (on the basis of a standard construction in differential geometry) a real flat vector bundle ξ over M and a flat connection map ∇_p on the space $\Omega^p(M,\xi)$ of differential p-forms on M with values in ξ. One can say that χ determines the space of smooth sections in the vector bundle $\Lambda^p(TM)^*\otimes\xi$. One can construct from the metric on M and Hermitian structure in ξ a Hermitian structure in $\Lambda(TM)^*\otimes\xi$ and the inner products $\langle\cdot,\cdot\rangle_m$ in the space $\Omega^m(M,\xi)$. Thus

$$S_{\mathcal{O}}=\langle\omega,\mathcal{O}\omega\rangle_m,\quad \mathcal{O}=*\nabla_m, \tag{4}$$

where $(*)$ is the Hodge-star map. The map $\mathcal{O}$ is formally self-adjoint with the property $\mathcal{O}^2=\nabla_m^*\nabla_m$. Suppose that the quadratic functional (4) is defined on the space $\mathcal{G}=\mathcal{G}(M,\xi)$ of smooth sections in a real Hermitian vector bundle ξ over M. There exists a canonical topological elliptic resolvent $R(S_{\mathcal{O}})$, related to the functional (4), namely

$$0\overset{0}{\to}\Omega^0(M,\xi)\overset{\nabla_0}{\to}\ldots\overset{\nabla_{m-2}}{\to}\Omega^{m-1}(M,\xi)\overset{\nabla_{m-1}}{\to}\ker(S_{\mathcal{O}})\overset{0}{\to}0. \tag{5}$$

Therefore, for the resolvent $R(S_{\mathcal{O}})$, we have $\mathcal{G}_p=\Omega^{m-p}(M,\xi)$ and $H^p(R(S_{\mathcal{O}}))=H^{m-p}(\nabla)$, where $H^p(\nabla)=\ker(\nabla_p)/\mathrm{Im}(\nabla_{p-1})$ are the cohomology space. Note that $S_{\mathcal{O}}\geqslant 0$ and therefore $\ker(S_{\mathcal{O}})\equiv\ker(\mathcal{O})=\ker(\nabla_m)$. Let us choose an inner product $\langle\cdot,\cdot\rangle_{H^p}$ in each space $H^p[R(S_{\mathcal{O}})]$.

The partition function of $S_{\mathcal{O}}$ with resolvent (5) can be written in the form:[14,16]

$$\mathfrak{W}(k)\equiv\mathfrak{W}(k;R(S_{\mathcal{O}}),\langle\cdot,\cdot\rangle_H,\langle\cdot,\cdot\rangle)=(\pi/k)^{\zeta(0,|\mathcal{O}|)/2}e^{-\frac{i\pi}{4}\eta(0,\mathcal{O})}\tau(M,\chi,\langle\cdot,\cdot\rangle_H)^{1/2}, \tag{6}$$

where $|\mathcal{O}|=\sqrt{\mathcal{O}^2}$ is defined via spectral theory. This is the basic formula one has to evaluate.

It can be shown that the zeta function $\zeta(s,|\mathcal{O}|)$ appearing in the partition function (6) is well-defined and analytic for $\mathrm{Re}\, s>0$ and can be continued to a meromorphic function on $\mathbb{C}$, regular at $s=0$. Furthermore, the zeta function can be expressed in terms of the dimensions of the cohomology spaces of $\mathcal{O}$. Since $H^p[R(S_{\mathcal{O}})]=H^{m-p}(\nabla)$ (the Poincarè duality) for the resolvent (5), it follows that (see Refs. 14 and 16 for details)

$$\zeta(0||\mathcal{O}|)=-\sum_{p=0}^{m}(-1)^p \dim H^p(R(S))=(-1)^{m+1}\sum_{p=0}^{m}(-1)^p \dim H^p(\nabla). \tag{7}$$

The dependence of the eta invariant $\eta(0|\mathcal{O})$ of Atiyah–Patodi–Singer[17–19] on the connection map $\mathcal{O}$ can be expressed with the help of the formula for the index of the twisted signature operator for a certain vector bundle over $M\otimes[0,1]$. Furthermore it can be shown[17] that $\eta(s|B)=2\,\eta(s|\mathcal{O})$, where the B are elliptic self-adjoint maps on $\Omega(M,\xi)$ defined on p-forms by

$$B_p=(-i)^{\lambda(p)}(*\nabla+(-1)^{p+1}\nabla *). \tag{8}$$

In this formula $\lambda(p)=(p+1)(p+2)+m+1$ and for the Hodge star-map we have used $*\alpha\wedge\beta=\langle\alpha,\beta\rangle_{\mathrm{vol}}$. From the Hodge theory we have

$$\dim\ker B=\sum_{p=0}^{m}\dim H^p(\nabla).$$

Finally the quantity $\tau(M,\chi,\langle\cdot,\cdot\rangle_H)$ is related to the Ray–Singer (analytic) torsion $T_{an}^{(2)}(M)$. In fact, if $H^0(\nabla)\neq 0$ and $H^p(\nabla)=0$ for $p=1,\ldots,m$, then the product

$$\tau(M,\chi,\langle\cdot,\cdot\rangle_H)=T_{an}^{(2)}(M)\cdot \mathrm{Vol}(M)^{-\dim H^0(\nabla)}, \tag{9}$$

is metric independent,[20] i.e., the metric dependence of the Ray–Singer torsion factors out as $V(M)^{-\dim H^0(\nabla)}$.

THE CASE OF REAL COMPACT HYPERBOLIC MANIFOLDS

Let us consider the specific case of a compact hyperbolic 3-manifolds of the form $M=\Gamma\backslash\mathbb{H}^3$. If the flat bundle ξ is acyclic, then for analytic torsion one gets[21]

$$[T_{an}^{(2)}(X_\Gamma)]^2\equiv\mathfrak{R}_\chi(0)=\prod_{p=0}^{\dim M}[\det\triangle_p]^{(-1)^{p+1}p/2}, \tag{10}$$

where $\mathfrak{R}_\chi(s)$ is the Ruelle function and $\triangle_p$ is the Laplacian restricted on p-forms, and the determinants are defined by means of zeta regularization. The function $\mathfrak{R}_\chi(s)$ extends meromorphically to the entire complex plane $\mathbb{C}$; it is an alternating product of more complicated factors, each of which is a Selberg zeta function $Z_p(s;\chi)$. The Ruelle function associated with closed oriented hyperbolic 3-manifold $\Gamma\backslash\mathbb{H}^3$ has the form $\mathfrak{R}_\chi(s)=Z_0(s;\chi)Z_2(2+s;\chi)/Z_1(1+s;\chi)$. For the Ray–Singer torsion one gets[12]

$$[T_{an}(\Gamma\backslash H^3)]^2=\mathcal{R}_\chi(0)=\frac{[Z_0(2,\chi)]^2}{Z_1(1,\chi)}\exp\left(-\frac{\mathrm{Vol}(\Gamma\backslash\mathbb{H}^3)}{3\pi}\right), \tag{11}$$

where $\mathrm{Vol}(\Gamma\backslash\mathbb{H}^3)$ is the volume of a fundamental domain of $\Gamma\backslash\mathbb{H}^3$. In the presence of non-vanishing Betti numbers $b_j=b_j(\Gamma\backslash\mathbb{H}^3)$ we have[12,22]

$$[T_{an}(\Gamma\backslash H^3)]^2=\frac{(b_1-b_0)![Z_0^{(b_0)}(2,\chi)]^2}{[b_0!]^2 Z_1^{(b_1-b_0)}(1,\chi)}\exp\left(-\frac{\mathrm{Vol}(\Gamma\backslash\mathbb{H}^3)}{3\pi}\right). \tag{12}$$

Now we consider the contribution associated with the eta invariant. A remarkable formula relating $\eta(s,\mathcal{O})$ to the closed geodesics on $\Gamma\backslash\mathbb{H}^3$ has been obtained by Millson.[23] More explicitly, Millson has proved the following result for a Selberg type (Shintani) zeta function $\tilde{Z}(s,\mathcal{O})$, which admits a meromorphic continuation to the entire complex plane. $\tilde{Z}(s,\mathcal{O})$ is a holomorphic function at $s=0$ and

$$\log\tilde{Z}(0,\mathcal{O})=\pi i\,\eta(0,\mathcal{O}). \tag{13}$$

Furthermore, it is possible to show that $\tilde{Z}(s,\mathcal{O})$ satisfies the functional equation $\tilde{Z}(s,\mathcal{O})\tilde{Z}(-s,\mathcal{O})=e^{2\pi i\,\eta(0,\mathcal{O})}$.

Now we have all the ingredients for evaluation of the partition function (6) in terms of Ray–Singer torsion and a Selberg type function. The final result is

$$\mathfrak{W}(k)=\left(\frac{\pi}{k}\right)^{\zeta(0,|\mathcal{O}|)/2}\left[\frac{\mathcal{R}_\chi(0)}{\tilde{Z}(0,\mathcal{O})}\right]^{1/4}[\mathrm{Vol}(\Gamma\backslash G)]^{-\dim H^0(\nabla)/2}, \tag{14}$$

where $\zeta(0,\mathcal{O})$ is given by Eq. (7).

CONCLUDING REMARKS

We have derived explicit formulas for the semiclassical approximation to the Chern–Simons partition function, using the invariant integration method. The final formulas are given in a form where the behavior as $k\mapsto\infty$ is obvious. In this connection we have explicitly exhibited the first term in the level-k asymptotic expansion for compact hyperbolic families of 3-manifolds.

The evaluation of the Ray–Singer torsion presented in this paper may be useful within the Euclidean path-integral approach to 3-dimensional quantum gravity, where the partition function is evaluated by summing the contributions from all possible topologies.[24] For negative cosmological constant Λ, the classical extrema of the Euclidean action are hyperbolic manifolds. It has been shown that 3-dimensional gravity can be rewritten as a Chern–Simons theory for a suitable gauge group.[25] Therefore in the one-loop partition function the quantum prefactor turns out to be dependent on the Ray–Singer torsion of a hyperbolic manifold. Note that the dependence on the volume of the Ray–Singer torsion is exponentially decreasing, making a contribution to the one-loop Euclidean partition function of the same nature of the one corresponding to the classical action. Namely, the one-loop Euclidean partition function, including only one extremum with $\Lambda<0$ and in absence of zero modes, reads (see also Ref. 12)

$$\mathfrak{W}_{\Gamma\backslash\mathbb{H}^3}=\left[\frac{\mathcal{R}_\chi(0)}{\tilde{Z}(0,\mathcal{O})}\right]^{1/4}\exp\left[-\frac{\mathrm{Vol}(\Gamma\backslash\mathbb{H}^3)}{4\pi G}\left(\frac{1}{G|\Lambda|^{1/2}}+\frac{1}{3}\right)\right], \tag{15}$$

where the second term in the exponential is the first quantum correction.

Note that there is a class of compact sufficiently large hyperbolic manifolds which admit arbitrarily large values of $b_1(M)$. In general, hyperbolic manifolds have not been completely classified and therefore a systematic computation is not yet possible. However this is not the case for certain sufficiently large manifolds, the Haken manifolds.[26] There exists an algorithm for the enumeration of all Haken manifolds, and there exists an algorithm for recognizing homeomorphy of the Haken manifolds.[27] These manifolds give an essential contribution to the partition functions (14) and (15).

Finally, the explicit result (14) can be very important for investigating the relation between quantum invariants for an oriented 3-manifold, defined with the help of a representation theory of quantum groups,[3,4] and Witten's invariant,[1] which is, instead, related to the path integral approach.

A. A. B. was partially supported by a CNPq grant (Brazil), RFFI Grant (Russia) 98-02-18380-a, and by GRACENAS Grant (Russia) 6-18-1997.

*)e-mail: abyts@fisica.uel.br
†)e-mail: faleiros@npd.uel.br
‡)e-mail: goncalve@fisica.uel.br

[1] E. Witten, Commun. Math. Phys. **121**, 351 (1989).
[2] G. Moor and N. Seiberg, Commun. Math. Phys. **123**, 77 (1989).
[3] N. Reshetikhin and V. Turaev, Commun. Math. Phys. **127**, 1 (1990).
[4] N. Reshetikhin and V. Turaev, Invent. Math. **103**, 547 (1991).
[5] R. Dijkgraaf and E. Witten, Commun. Math. Phys. **129**, 393 (1990).
[6] R. Kirby and P. Melvin, Invent. Math. **105**, 473 (1991).
[7] D. S. Freed and R. E. Gompf, Commun. Math. Phys. **141**, 79 (1991).
[8] L. C. Jeffrey, Commun. Math. Phys. **147**, 563 (1992).
[9] S. K. Rama and S. Sen, Mod. Phys. Lett. A **8**, 2285 (1993).
[10] L. Rozansky, Commun. Math. Phys. **171**, 279 (1995).
[11] L. Rozansky, Commun. Math. Phys. **175**, 275 (1996).
[12] A. A. Bytsenko, L. Vanzo, and S. Zerbini, Nucl. Phys. B **505**, 641 (1997).
[13] A. S. Schwarz, Commun. Math. Phys. **64**, 233 (1979).
[14] D. H. Adams, Phys. Lett. B **417**, 53 (1998).
[15] A. A. Bytsenko, G. Cognola, L. Vanzo, and S. Zerbini, Phys. Rep. **266**, 1 (1996).
[16] D. H. Adams and S. Sen, http://xxx.lanl.gov/abs/hep-th/9503095.
[17] M. F. Atiyah, V. K. Patodi, and I. M. Zinger, Math. Proc. Cambridge Philos. Soc. **77**, 43 (1975).
[18] M. F. Atiyah, V. K. Patodi, and I. M. Zinger, Math. Proc. Cambridge Philos. Soc. **78**, 405 (1975).
[19] M. F. Atiyah, V. K. Patodi, and I. M. Zinger, Math. Proc. Cambridge Philos. Soc. **79**, 71 (1976).
[20] D. Ray and I. Singer, Adv. Math. **7**, 145 (1971).
[21] D. Fried, Invent. Math. **84**, 523 (1986).
[22] A. A. Bytsenko, A. E. Gonçalves, and W. da Cruz, Mod. Phys. Lett. A **13**, 2453 (1998).
[23] J. J. Millson, Ann. Math. **108**, 1 (1978).
[24] S. Carlip, Class. Quantum Grav. **10**, 207 (1993).
[25] E. Witten, Nucl. Phys. B **311**, 46 (1988).
[26] W. Haken, Acta Math. **105**, 245 (1961).
[27] S. V. Matveev, Usp. Mat. Nauk **52**, 147 (1997).

Published in English in the original Russian journal. Edited by Steve Torstveit.

Detection of the decay of an acoustic soliton arising during pulsed breakdown of a glassy semiconductor film

É. N. Voronkov*)
Moscow Power Engineering Institute, 111250 Moscow, Russia

(Submitted 21 June 1999)
Pis'ma Zh. Éksp. Teor. Fiz. **70**, No. 2, 70–72 (25 July 1999)

The results of an experiment demonstrating the appearance of a soliton under certain conditions of pulsed breakdown of a glassy semiconductor film in a magnetic field are reported. The wave is excited by a current filament moving at a velocity close to the speed of sound between two parallel electrodes in an external magnetic field. To distinguish the direction of motion of the acoustic wave and that of the current filament along the substrate, electrodes with a bend that changes the direction of motion of the filament are deposited. Two ''frozen'' structural-excitation fronts, diverging at an angle to one another and attesting to the decay of the soliton at the moment the current filament vanishes, are observed at the location of the bend in the electrodes. [S0021-3640(99)00214-5]

PACS numbers: 61.43.Dq, 43.35.Ns

An excited electronic subsystem in glassy semiconductors transfers energy to the structural matrix. This gives rise to a metastable state of the structure, and the propagation of this state can be accompanied by the generation of a directed acoustic wave. In the present letter the results of an experiment demonstrating the appearance of an acoustic soliton under certain conditions of pulsed breakdown of a glassy semiconductor film (5 μm thick As_2SeTe_2) are reported. The film was deposited by vacuum deposition on a $20\times 70\times 1.5$ mm glass substrate. Metallic (Al) strips — electrodes separated by 1 mm — were present on the film surface. Pulsed breakdown was accomplished in the gap between these electrodes in a 2 T external magnetic field.

A glassy chalcogenide semiconductor (GCS) was chosen as the object of study on the basis of the fact that these materials can possess a metastable structural state.[1,2] Moreover, it is much easier to excite the electronic subsystem in them than in classical glasses. The use of GCS films also enables visual detection of the structural changes occurring in the material, since these materials easily crystallize and melt.

The electronic subsystem was excited by voltage pulses with amplitudes up to 800 V and duration up to 4 ms applied to the electrodes. The amplitude of the maximum current in a pulse was set at a level sufficient for streamer breakdown but insufficient for leader breakdown. This made it possible to produce a stable current filament perpendicular to the contacts. The channel filled with an electron–hole plasma arising in the process was moved along the sample by the external magnetic field, producing excitation in the entire

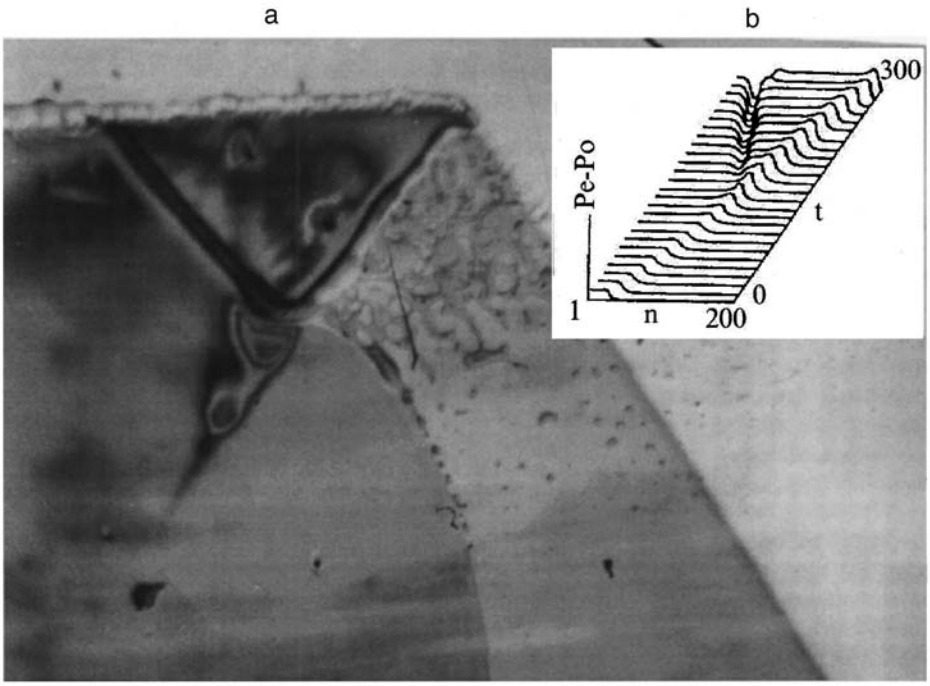

FIG. 1. a) Photograph of a section of the film with traces of soliton decay (the excitation propagated from left to right); b) results of simulation of soliton decay.[4]

region through which it passed. This region comprised a large fraction of the area of the entire sample.

Since the velocity of the filament was close to the velocity of sound, the method used to excite the structure ruled out overheating of the material by Joule heat. On the one hand this made it possible to increase the excitation power and on the other it made it possible to detect the changes arising as a result of the interaction between the excited electronic subsystem and the initially ''cold'' matrix.

It should be noted that after passage of the current filament the outward appearance and properties of the film remained virtually unchanged, aside from a small increase in the resistivity. The visible evidence of excitation of the film consisted of a decrease in reflection (the film became darker) and the appearance of macrodefects, if they were present (scratches, extraneous impregnations) as a result of decoration of the material which had crystallized around them.

The calculations performed in Ref. 3 show that the propagation of an excitation in a plasma of partially mobile ions can give rise to an acoustic soliton. To distinguish the direction of motion of the acoustic wave and the direction of motion of the plasma filament along the substrate and to separate the region of the film where excitation of the electronic subsystem had occurred from the region where there was no such excitation, electrodes containing a bend which changed the direction of motion of the filament were used. After a voltage pulse was applied to such a sample, two ''frozen'' structural exci-

tation fronts, which diverged at an angle to one another (Fig. 1a), were observed at the location of the bend in the electrodes. Splashes of material were observed in front of the crest of the leading edge. This indicates that this front propagated with a substantial release of energy. The trailing edge consisted of a trough. The picture observed at the location of the bend in the electrodes can be explained by the fact that the bend resulted in a sharp decrease in the intensity of the electric field in the filament reaching it and, correspondingly, in the cessation of current in it, i.e., pumping of the electronic subsystem, a consequence of which was ''freezing'' of the structure of the material in the state in which it was found at this moment.

The results of numerical simulation of soliton dynamics in bistable media explain the appearance of two fronts. Figure 1b displays simulation results showing the decay of a topological soliton.[4] The agreement between the experiment performed and the computational results presented in Ref. 4 is interesting. A characteristic feature of the experiment with respect to the calculations is that in our case the propagation of the stationary wave was associated with not the bistability of the system but rather a constant inflow of energy, which transferred the system into a metastable state with a higher energy. When the inflow of energy ceased, the soliton decayed.

In conclusion, it should be noted that the application of a magnetic field in experiments on breakdown of semiconductors and dielectrics makes it possible not only to increase substantially the current density without destroying the sample but also to investigate a number of fast processes because of the spatial sweep effectuated by the magnetic field. At the same time, the results obtained made it possible to demonstrate the important (in many cases decisive) role of coherent acoustic waves, which in experiments on breakdown of solids is usually masked by the delayed action of thermal effects.

*)e-mail: edward@b14s1nt.mpei.ac.ru

[1] M. I. Klinger and V. G. Karpov, Zh. Éksp. Teor. Fiz. **82**, 1687 (1982) [Sov. Phys. JETP **55**, 976 (1982)].
[2] S. A. Dembovskiĭ, A. S. Zyubin, and F. V. Grigor'ev, Fiz. Tekh. Poluprovodn. **32**, 944 (1998) [Semiconductors **32**, 843 (1998)].
[3] K. Saeki, Phys. Rev. Lett. **80**, 1224 (1998).
[4] L. I. Manevich, A. V. Savin, V. V. Smirnov, and S. N. Volkov, Usp. Fiz. Nauk **164**, 937 (1999).

Translated by M. E. Alferieff

Lateral localization of optical phonons in GaAs quantum islands

M. D. Efremov, V. A. Volodin,*) V. V. Preobrazhenskiĭ, and B. R. Semyagin
Institute of Semiconductor Physics, Siberian Branch of the Russian Academy of Sciences, 630090 Novosibirsk, Russia

V. A. Sachkov and V. V. Bolotov
Institute of Sensor Microelectronics, Siberian Branch of the Russian Academy of Sciences, 644077 Omsk, Russia

E. A. Galaktionov and A. V. Kretinin
Novosibirsk State University, 630090 Novosibirsk, Russia

(Submitted 2 June 1999)
Pis'ma Zh. Éksp. Teor. Fiz. **70**, No. 2, 73–79 (25 July 1999)

Lateral localization of phonons in GaAs islands formed on the (100) surface under conditions of (2×4) structural reconstruction is detected by means of Raman scattering. The triplet structure of the peak corresponding to laterally localized phonons is detected in the Raman scattering spectra of a $GaAs_{0.6}/AlAs_5$ sublattice grown by molecular-beam epitaxy. The distribution of islands over different configurations is determined by comparing the theoretical Raman scattering spectra, calculated in the Vol'kenshteĭn bond polarizability approximation, with the experimental spectra. The atomic configuration of the islands is identical to the results obtained previously by scanning tunneling microscopy. According to the calculation, 70% of the islands contain fewer than 18 Ga atoms, and lateral localization occurs with AlAs barrier thickness of 2 or more monolayers. © *1999 American Institute of Physics.* [S0021-3640(99)00314-X]

PACS numbers: 63.20.Dj, 78.30.Fs

The properties of quantum-size objects produced by molecular-beam heteroepitaxy of III–V semiconductors largely depend on the structural quality of the heterointerfaces. The growth of layers under conditions of structural reconstruction of the surface fixes the atomic relief of the heterointerface, which can dramatically change the properties of superlattices with ultrathin layers of materials. In the last few years a great deal of attention has been devoted to finding the mechanisms leading to the reconstruction of the (100) GaAs surface and to determining the structure of the atomic configurations on it. Progress in this field depends primarily on the development of direct methods for investigating surface structure: scanning tunneling microscopy, atomic force microscopy, and high-resolution electron microscopy. Thus, it has been established on the basis of scanning tunneling microscopy and HEED data that the (2×4) reconstruction of the (001)

GaAs surface consists of highly ordered chains of arsenic dimers extended along the [110] direction.[1–3] Direct observations using scanning tunneling microscopy have revealed that with a submonolayer gallium coating on a reconstructed surface GaAs(001)–(2×4) the gallium adatoms form quantum islands extending in the direction [110]. The width of the islands in the [100] direction is twice the interatomic distance, and the most stable islands are ones containing six or fewer Ga dimers.[4] Of special interest is the question of the extent to which the structural reconstruction of the surface determines the atomic structure of the heterointerface (since it is not obvious that the surface structure is preserved during heteroepitaxial growth) and determines the phonon properties of the heterostructures obtained. The present work is devoted to solving this question.

Since the frequencies of the optical vibrations of atoms in GaAs and AlAs are different, optical phonons localize within a layer of one material with a damping depth of one monolayer in the neighboring layers.[5] The frequency of the localized phonons depends on the characteristic size of the object.[6–8] This makes it possible to determine it with atomic accuracy from Raman scattering spectroscopy data.[5–8] However, since nonresonant Raman scattering is weak, it is impossible to study an individual object, and to increase the signal a large ensemble of quantum-size objects must be produced. So far, the phonon properties of GaAs islands obtained by submonolayer growth under conditions of structural reconstruction of the surface have not been investigated. It can be expected that lateral localization of phonons in islands will modify the Raman scattering spectra, since the strongest shift of the phonon frequency is observed when the dimensions of the GaAs quantum objects equal several interatomic distances.[9–13]

The $GaAs_{0.6}/AlAs_5$ superlattices investigated were grown by molecular-beam epitaxy on a semi-insulating GaAs(001) substrate with a 0.1 μm thick GaAs epitaxial buffer layer. The substrate temperature was 550 °C. Prior to each opening of the gallium flux growth was interrupted for a time, and the AlAs surface was held for a time under conditions conducive to (2×4) reconstruction. The state of the surface was monitored by HEED. After the flux of gallium atoms was interrupted, the structure was held for a time in vacuum, so that stable configurations of GaAs islands on the surface of the AlAs layer would survive. The alternating GaAs and AlAs layers were 0.6 and 5 ML thick, respectively. The $GaAs_{0.6}/AlAs_5$ superlattice contained 400 periods and was coated with a 4 nm thick protective layer of GaAs. The phonon spectrum of the objects obtained was investigated using Raman scattering spectroscopy. The spectra were recorded at room temperature in the backscattering geometry $Z[XY]\overline{Z}$ on an automated setup based on a DFS-52 monochromator. The Raman scattering was excited by Ar-laser lines.

Figure 1 shows the Raman scattering spectra of a $GaAs_{0.6}/AlAs_5$ superlattice with excitation by the Ar-laser lines 514.5, 496.5, 488, and 476.5 nm. The peak near 290 cm^{-1}, which is seen in all spectra, corresponds to Raman scattering by long-wavelength LO phonons in the GaAs substrate. This shows that the superlattice is semitransparent at the wavelengths used. For all excitation wavelengths the Raman scattering signal corresponding to scattering by an LO phonon localized in GaAs possesses a triplet structure (peaks 1–3). The transverse optical phonons are inactive in Raman scattering from the (001) surface.[5] The position of the 258 cm^{-1} peak corresponds to the first localized mode for longitudinal phonons in a GaAs layer with an effective thickness of 0.6 ML. It is natural to infer that the appearance of the additional phonon modes with different frequencies is due to the lateral structure of GaAs quantum objects. The fre-

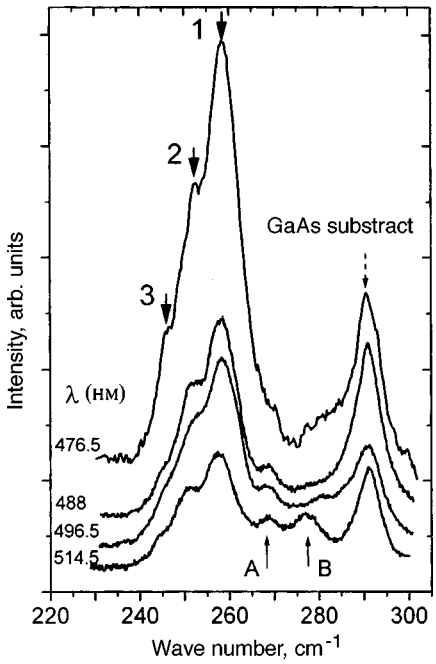

FIG. 1. Raman scattering spectra of a $GaAs_{0.6}/AlAs_5$ superlattice, grown on a $(001)-(2\times4)$ reconstructed surface. The spectra were recorded in $Z[XY]\overline{Z}$ geometry for various scattering excitation wavelengths.

quency of peak 2 differs from that of peak 1 by $7.5\,\mathrm{cm}^{-1}$, and the difference between the frequencies of peaks 3 and 2 is $5.5\,\mathrm{cm}^{-1}$ for all Raman scattering excitation wavelengths. These parameters can be used to estimate the lateral dimensions of GaAs objects, which equal 2–3 lattice constants. It should be noted that the structure of the observed Raman scattering spectra was not distinguished in surface scans of the superlattice. This indicates that it is uniform and that the GaAs quantum objects formed are stable.

To determine the structure and form of the GaAs quantum islands produced on an AlAs (001) surface, theoretical calculations of the phonon modes were performed for various configurations. The calculations of the characteristic frequencies and vectors of the vibrational modes were performed in the Born–Karman approximation taking account of the interaction of eight nearest neighbors. The long-range Coulomb interaction was taken into account in the dipole approximation in the ''rigid-ion'' model. The effective charge of the cations and anions and the elastic parameters were fit by the least-squares method to the experimental data on neutron scattering by phonons in the directions Δ, Σ, Λ, Z, and Q, obtained at $T=12\,\mathrm{K}$.[14] Next, the phonon frequencies were extrapolated to room temperature, starting from the temperature dependence $\delta\omega/\delta T = -1.35\times10^{-2}\,\mathrm{cm}^{-1}\,\mathrm{K}^{-1}$ (Ref. 15).

Since three localized LO modes were clearly observed in the experimental Raman scattering spectra (Fig. 1), it was assumed at first that the reconstruction of the surface corresponded to the Chadi model,[1,2] in which three infinite rows of arsenic dimers are separated by a row of vacancies. However, the calculations showed that if the GaAs

islands were infinite ''quantum wires'' extended along the $[\bar{1}11]$ direction and possessing in the [110] direction a width of three gallium atoms and one aluminum atom, then only two of the nine optical modes of gallium arsenide are Raman-active in the (XY) geometry, and the frequency of the most intense mode is 6 cm^{-1} higher than the frequency of the experimentally observed peak 1 (Fig. 1). As was shown in Ref. 3 by scanning tunneling microscopy, the unit cell of the reconstructed surface $(001)-(2\times4)$ with configurations α, β, and γ contains two arsenic dimers and two dimer vacancies. In Ref. 4 it was established on the basis of scanning tunneling microscopy data that the Ga adatoms form quantum islands extended along the $[1\bar{1}0]$ direction, and the width of the islands in the [110] direction is twice the interatomic distance.

Let us consider first the configuration of GaAs islands in the form of infinite quantum wires along the [110] direction, which are formed by Ga dimers. The unit cell of such a structure in the [110] direction contains two Ga and two As atoms, separated by four Al and As atoms, and it contains five AlAs monolayers in the [001] growth direction. In this configuration the GaAs coverage is 0.5 ML, and the AlAs coverage is 5.5 ML. The phonon spectrum and the Raman scattering spectrum in the $Z[XY]\bar{Z}$ geometry were calculated for such islands, and the results are presented in Fig. 2a. The vertical lines show the characteristic frequencies of GaAs-type phonon modes, the heights of the lines are proportional to the Raman scattering intensity, and the modes which are inactive in scattering are labeled below, similar notations were adopted for all calculations. In all computed spectra the width of all Raman scattering lines at half-height was taken to be 5 cm^{-1}. As one can see from Fig. 2a, two of the six GaAs-type optical phonon modes are active in scattering. This is natural, since the unit cell in this configuration contains two Ga atoms. The first mode lies approximately 2 cm^{-1} higher than the experimental peak 1 (Fig. 1), and the second mode lies 8 cm^{-1} below the first one. These two modes arise because of the lateral localization of GaAs-type optical phonons in the [110] direction, perpendicular to the quantum wire.

As already mentioned, the most stable configurations of the GaAs islands were the islands containing six or fewer Ga dimers.[4] If the GaAs quantum wire whose configuration is described above is broken by barriers consisting of Al atoms, GaAs-type optical phonons will also be localized in the [110] direction. The phonon spectra of such finite-length quantum wires were calculated for different AlAs barrier thicknesses. For a barrier thickness of one Al atom the computed phonon spectrum with such structures was essentially identical to the spectrum of an infinite wire. For a barrier thickness of two Al atoms, characteristic features associated with the additional lateral localization of optical phonons appeared sharply in the spectrum, and as the barrier thickness increased to three or more Al atoms, no further transformation of the spectrum was observed. This allows us to conclude that the penetration of GaAs-type optical phonons modes in the lateral direction into AlAs is very small, and a 2 ML AlAs barrier is sufficient for lateral localization to appear. It should be noted that the ''lateral decay'' depth corresponds to the decay depth in the direction of growth, which is 1–2 ML.[5,8]

The phonon and Raman scattering spectra of an island with a 6×2 configuration (where 6 and 2 are the numbers of Ga atoms in the $[1\bar{1}0]$ and [110] directions, respectively, and they are separated by barriers consisting of two Al atoms) are displayed in Fig. 2b. In this configuration the coverage of the GaAs layer is 0.375 ML. It is evident that the six Raman-active modes (from a total of 36 modes) form groups of three bands,

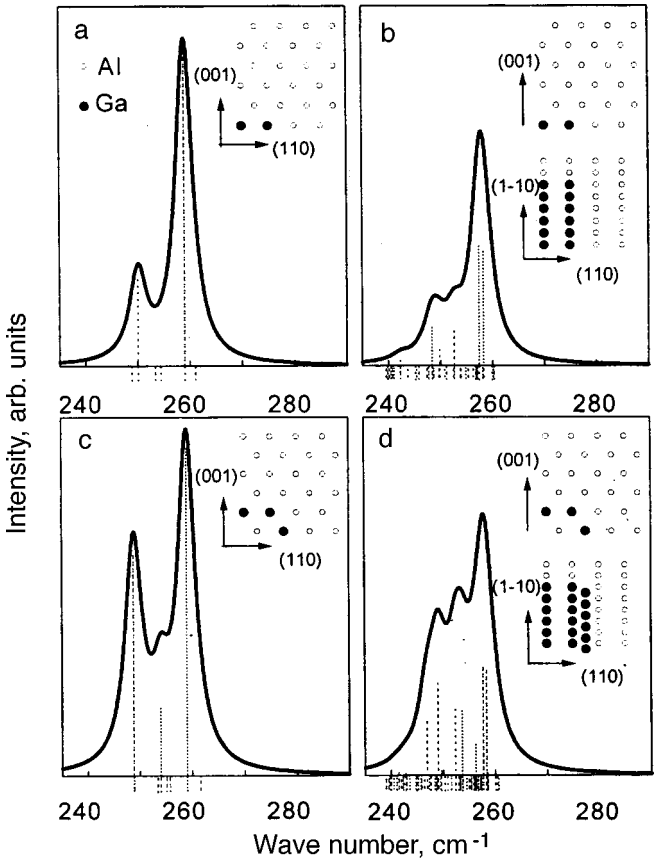

FIG. 2. Phonon spectra and Raman scattering spectra calculated for various configurations of GaAs quantum islands. The positions of the GaAl atoms are shown, and the positions of the As atoms are not shown.

whose frequencies are close to the frequencies of the experimentally observed peaks. The qualitatively computed spectra correspond to the experimentally observed spectra, but the ratios of the intensities of the experimental peaks 1, 2, and 3 (Fig. 1) are different from the calculations (Fig. 2b).

When the reconstructed surface AsAs$(001)-(2\times4)$ is covered with a GaAs layer with a thickness greater than 0.5 ML, the Ga atoms can fill not only the As dimer rows,[4] but they can also fill the ''trenches'' on the $(001)-(2\times4)$ surface. The Raman spectra for such configurations of GaAs islands are presented in Figs. 2c and 2d. The configuration in Fig. 2c is a quantum wire of infinite length in the direction [110], and its unit cell in the [110] direction contains two Ga and two As atoms, separated by four Al and As atoms, and a Ga atom located on the first layer below in the direction of growth. The configuration in Fig. 2d is similar to the preceding one, but the length of the GaAs quantum wire is bounded by six Ga atoms, separated by a 2 Al atom barrier. The coverage of the GaAs layer for the configurations in Figs. 2c and 2d is 0.75 and 0.625 ML, respectively. It is evident from Figs. 2c and 2d that the Raman scattering spectrum calculated for the last configuration agrees qualitatively with experiment, and the com-

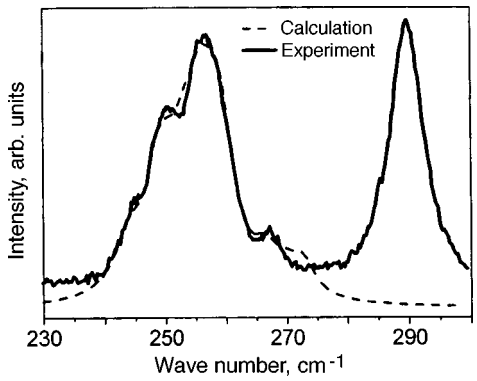

FIG. 3. Experimental ($\lambda_{exc}=488$ nm and computed Raman scattering spectra of a $GaAs_{0.6}/AlAs_5$ superlattice grown on a (2×4) reconstructed (001) surface.

puted and experimental average thicknesses of the GaAs layers agree well with each other.

Returning to Fig. 1 and comparing it with Fig. 2, we note that the peaks 1, 2, and 3 can be explained qualitatively and quantitatively on the basis of the computed Raman scattering spectra for the above-mentioned configurations, but the experimentally observed features marked by upward arrows in Fig. 1 cannot be explained. These features can be explained if it is assumed that GaAs quantum islands thicker than 1 ML can form. The Raman scattering spectra of GaAs layers on a reconstructed $AlAs(001)-(2\times4)$ surface with average thickness 1, 1.25, and 1.5 ML were calculated, and it was found that for such quite thick layers the characteristic features associated with the lateral structure are practically absent, but rather one peak corresponding to scattering by the $LO1$ mode is observed. Apparently, the peaks near 269 and 277 cm^{-1}, clearly observed in the experimental spectrum for excitation wavelength 514 nm, can be explained by scattering on phonons localized in such GaAs objects with an average thickness of 1 and 1.5 ML. When the wavelength exciting Raman scattering is 514 nm, the conditions of Raman scattering are probably close to resonance, which explains the dependence of the intensity of these peaks on the pump wavelength.

Figure 3 shows the experimental Raman scattering spectrum for a wavelength of 488 nm in comparison with the computed spectrum, where the contribution of the 10 main island configurations was taken into account. The theoretical spectrum was fit to the experimental spectrum by minimizing the standard deviation. It is evident from the figure that the agreement between theory and experiment is very good. In addition, it is extremely surprising that even the GaAs layer thickness obtained by averaging over all configurations agreed with amazing accuracy with the experimental thickness — 0.6 ML. Judging from the results of the fit, about 70% of the GaAs quantum islands contain fewer than 18 Ga atoms, confirming the results of Ref. 4.

In summary, in the present work the Raman scattering method was used to determine the structure of a GaAs/AlAs heterointerface, which corresponded to (2×4) structural reconstruction of the surface and agreed with the scanning tunneling microscopy data.[4] It was demonstrated that the lateral localization of phonons in GaAs islands occurs

over a distance of one or two interatomic distances, which makes it possible to determine the atomic structure of the heterointerface by comparing the experimental and computed Raman scattering spectra.

This work was supported by the Russian Fund for Fundamental Research (Grants 97-02-18422 and 99-02-16668) and by the Siberian Branch of the Russian Academy of Sciences (Grant 16 of the competition for young scientists for projects in physicotechnical sciences). The authors are grateful to the Scientific Council of the Institute of Semiconductor Physics, Siberian Branch of the Russian Academy of Sciences, for sponsoring investigations, as expressed in the award of a young-scientists stipend to V. A. Volodin by the Institute of Semiconductor Physics of the Siberian Branch of the Russian Academy of Sciences.

*)e-mail: volodin@isp.nsc.ru

[1] D. J. Chadi, J. Vac. Sci. Technol. A **5**, 834 (1987).
[2] Tomihiro Hashizume, Q. K. Xue, J. Zhou *et al.*, Phys. Rev. Lett. **73**, 2208 (1994).
[3] A. R. Avery, C. M. Goringe, D. M. Holmes *et al.*, Phys. Rev. Lett. **76**, 3344 (1996).
[4] M. Itoh, G. R. Bell, A. R. Avery *et al.*, Phys. Rev. Lett. **81**, 633 (1998).
[5] M. Cardona and G. Günterodt, *Light Scattering in Solids V. Superlattices and Other Microstructures* (Springer-Verlag, Berlin, 1989).
[6] J. Sapriel, J. C. Michel, J. C. Toledano *et al.*, Phys. Rev. B **28**, 2007 (1983).
[7] B. Jusserand, D. Paquet, J. Kervarec *et al.*, J. de Physique **45**, C5-145 (1984).
[8] M. Cardona, Superlattices Microstruct. **5**, 27 (1989).
[9] G. Armelles, P. Castrillo, P. D. Wang *et al.*, Solid State Commun. **94**, 613 (1995).
[10] P. Castrillo, G. Armelles, and J. Barbolla, Solid-State Electron. **40**, 175 (1996).
[11] V. A. Volodin, M. D. Efremov, V. Ya. Prints *et al.*, JETP Lett. **63**, 994 (1996).
[12] V. A. Volodin, M. D. Efremov, V. V. Preobrazhenskiĭ *et al.*, JETP Lett. **66**, 47 (1997).
[13] V. A. Volodin, M. D. Efremov, and V. V. Bolotov, Superlattices and Microstructures (in press).
[14] D. Strauch and B. Dorner, J. Phys.: Condens. Matter **2**, 1457 (1990).
[15] B. Jusserand and J. Sapriel, Phys. Rev. B **24**, 7194 (1981).

Translated by M. E. Alferieff

Ion acceleration by superintense laser pulses in plasmas

T. Zh. Esirkepov
Moscow Institute of Physics and Technology, 141700 Dolgoprudny, Moscow Region, Russia

Y. Sentoku, K. Mima, and K. Nishihara
Institute of Laser Engineering, Osaka University, Osaka 565-0871, Japan

F. Califano and F. Pegoraro
Dip. di Fisica, Università di Pisa and INFM, Pisa 56100, Italy

N. M. Naumova and S. V. Bulanov
General Physics Institute, Russian Academy of Sciences, 117924 Moscow, Russia

Y. Ueshima
JAERI-Kansai, Neyagawa, Osaka 564-8680, Japan

T. V. Liseikina and V. A. Vshivkov
Institute of Computation Technology, Siberian Branch of the Russian Academy of Sciences, 630090 Novosibirsk, Russia

Y. Kato
JAERI-Kansai, Tokai, Ibaraki 319-1100, Japan

(Submitted 9 June 1999)
Pis'ma Zh. Éksp. Teor. Fiz. **70**, No. 2, 80–86 (25 July 1999)

Ion acceleration by petawatt laser radiation in underdense and overdense plasmas is studied with 2D3V-PIC (Particle in Cell) numerical simulations. These simulations show that the laser pulse drills a channel through the plasma slab, and electrons and ions expand in vacuum. Fast electrons escape first from the electron–ion cloud. Later, ions gain a high energy on account of the Coulomb explosion of the cloud and the inductive electric field which appears due to fast change of the magnetic field generated by the laser pulse. Similarly, when a superintense laser pulse interacts with a thin slab of overdense plasma, its ponderomotive pressure blows all the electrons away from a finite-diameter spot on the slab. Then, due to the Coulomb explosion, ions gain an energy as high as 1 GeV. © *1999 American Institute of Physics.* [S0021-3640(99)00414-4]

PACS numbers: 52.65.Rr, 52.40.Nk

It is well known that the interaction of ultraintense laser pulses with plasmas is accompanied by the acceleration of charged particles, both ions and electrons. However, it is expected that ion acceleration will become more efficient when the plasma is irradiated by a petawatt laser pulse[1] than in the case of laser pulses with more moderate

power. Various acceleration mechanisms have been invoked in the different regimes of the laser–plasma interaction, including ion acceleration during the expansion of the plasma in vacuum[2] and the ''Coulomb explosion.'' The Coulomb explosion is associated with the breakdown of plasma quasineutrality when the electrons are expelled from a self-focusing radiation channel in the plasma, after which the ions expand due to the repulsion of the unneutralized electrical charge.[3] The Coulomb explosion has also been invoked in order to describe the generation of fast ions during the interaction of laser pulses with clusters.[4] This ion acceleration up to high energy values can shed light on the observed[5] neutron production in overdense plasmas and opens up a way of producing laser induced nuclear reactions in a controlled way.[6]

An electron interacting with an electromagnetic wave with intensity $I \approx 2 \times 10^{21}\,\mathrm{W/cm^2}$ acquires an energy equal to $\mathcal{E}_e = mc^2a^2/2 \approx 1\,\mathrm{GeV}$. This light intensity corresponds to laser pulses with powers in the petawatt range and to values of order $\sqrt{M/m}$ for the dimensionless amplitude $a = eE/m\omega c$. Here M/m is the ion-to-electron mass ratio. This means that in the wave field, electrons become as heavy as ions. A short laser pulse in an underdense plasma produces a wake with an amplitude $\varphi = \mathcal{E}_e/e$, where φ is the electrostatic potential. Thus, for $a \approx 2\sqrt{M/m}$ the ions gain an energy $\approx Mc^2$ during a half period of the wake wave, and the ion motion in the wake of the laser pulse in an underdense plasma becomes relativistic. We note that this amplitude of the laser radiation is much smaller than that for which the dimensionless amplitude a calculated with the ion mass becomes of order M/m, i.e., when the ion quiver velocity equals the speed of light. This latter amplitude corresponds to an intensity $I \approx 7 \times 10^{24}\,\mathrm{W/cm^2}$ for a 1 μm laser in a hydrogen plasma.

When considering the interaction of the laser pulse with an overdense plasma we take the plasma to have the form of a thin slab of width l_s. We assume that this plasma slab is irradiated by a laser beam with amplitude a and radius $R \gg l_s$ at the focus. The electrons interacting with the laser light are expelled from their initial position in the plasma slab. If the electron energy in the pulse field $\mathcal{E}_e = mc^2a^2/2$ is high enough, the electrons can overcome the attractive electric field due to charge separation. To blow the electrons off, the pulse amplitude must be such that $\mathcal{E}_e > \mathcal{E}_\mathrm{C}$, where the Coulomb energy is about $\mathcal{E}_\mathrm{C} \approx 2\pi^2e^2nl_sR$, or

$$a > (l_sR/d_e^2)^{1/2} \equiv (4\pi\epsilon_0 R/\lambda)^{1/2}. \tag{1}$$

Here $d_e = c/\omega_{pe}$ is the collisionless skin depth and $\epsilon_0 = l_s\lambda/4\pi d_e^2$ dimensionless parameter introduced in Ref. 7. Later the ions start to expand due to Coulomb repulsion. This is the Coulomb explosion. Ions gain an energy of the order of $\mathcal{E}_\mathrm{C}$, which, if it is assumed that $\mathcal{E}_e \approx \mathcal{E}_\mathrm{C}$, can be rewritten as $\mathcal{E}_i \approx Mc^2(m/M)a^2$. We see that ions acquire an energy of the order of the ion rest mass when $a \approx \sqrt{M/m}$.

The goal of the present paper is to analyze, with 2D-PIC (Particle in Cell) simulations, the mechanisms of the ion acceleration during the interaction of a petawatt laser pulse with underdense and overdense plasmas, when the radiation intensity reaches $\approx 10^{22}\,\mathrm{W/cm^2}$, which corresponds to $a > \sqrt{M/m}$.

To investigate the interaction of a laser pulse with a slab of underdense plasma, we have performed 2D-PIC fully relativistic simulations using a model value of the ion-to-electron mass ratio, 256, and $\sqrt{M/m} = 16$. Below we present the results of our simulations of a circularly polarized pulse with amplitude $a_e = 20$. The laser pulse is Gaussian

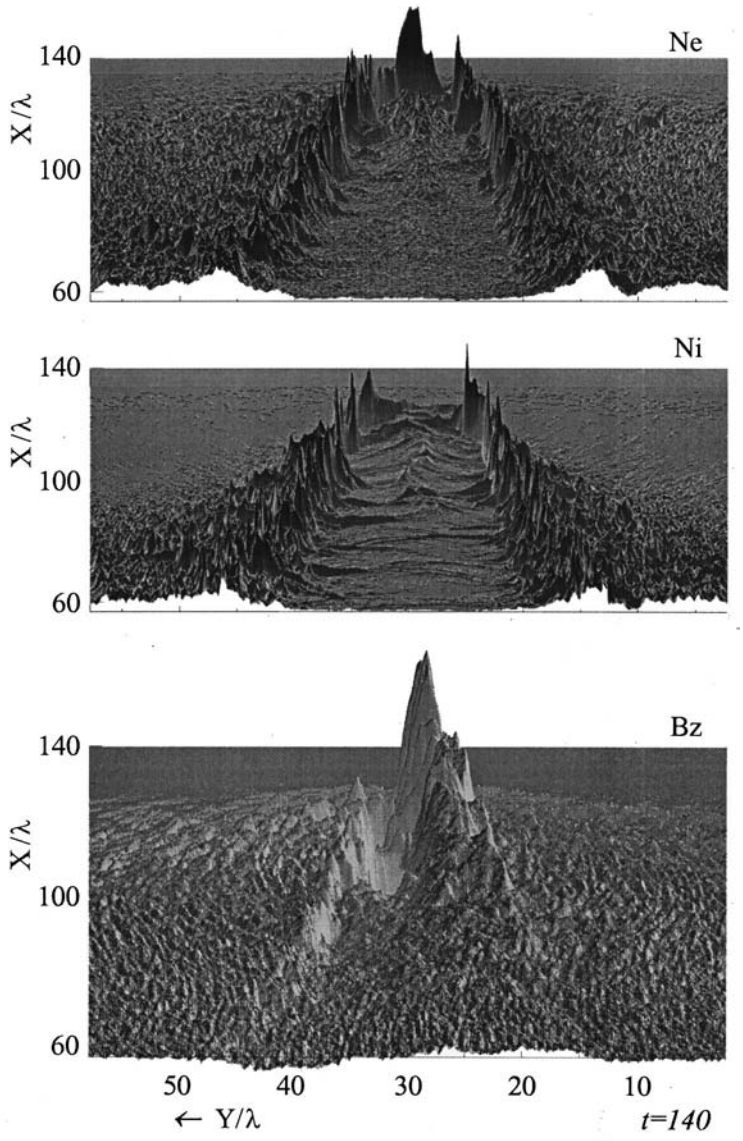

FIG. 1.

along y, with a full width $l_\perp = 10\lambda$, and has a triangular form along the x axis, with length $l_\parallel = 20\lambda$ and a sharp front of order 2λ. The plasma density corresponds to the ratio $\omega_{pe}/\omega = 0.45$ or $n = 0.2025 n_{\rm cr}$. The plasma slab, of length $L = 125\lambda$, begins at $x = 0$ and is preceded by a vacuum region 5λ long. The laser pulse is initialized outside the plasma in the vacuum region $x < 0$. In Fig. 1 we present the x,y distribution of the electron and ion densities and of the z component of the magnetic field at $t = 140(2\pi/\omega)$. The laser pulse is focused in a relatively small region due to relativistic self-focusing. However the

channel behind the laser pulse is not totally evacuated, as can be seen in Fig. 1. Indeed, the plasma moves predominantly outward in the radial direction, but at the same time an ''inverted'' corona mode of a hot, inward-expanding plasma is formed. Colliding on the channel axis, these hot plasma flows form a relatively dense plasma filament in the region $100\lambda < x < 120\lambda$. The phenomenon of the ''inverted'' corona and formation of a hot filament inside the channel was discussed in Ref. 8 in the framework of the gas dynamics approximation. In the present case the situation is more complex: the inward-expanding plasma is inhomogeneous in the direction along the channel and is formed by narrow jets. In addition, a significant portion of the filament is made up of plasma that enters the channel through the front region of the channel. The electric current carried by the filament sustains the dipolar magnetic field, which in turn focuses the plasma toward the axis.

Figure 2 shows the phase planes p_x, x of electrons (a) and ions p_x, x (b) and p_x, y (c). Figure 2c shows the x, y distribution of the z component of the magnetic field for $t = 175(2\pi/\omega)$, when the laser pulse has drilled a hole through the plasma slab. We see that the electron cloud expands into the vacuum in the forward direction. In the phase plane (p_x, y) shown in Fig. 2c we see that the ion motion is well collimated. The collimation of the ion motion can be explained by the pinching in the self-generated magnetic field, which changes polarity at the ion jet axis, as is seen in Fig. 2d.

The mechanisms that accelerate the ions can be described by invoking the pull on the ions by the electrons that are expanding in the forward direction, the Coulomb repulsion in the electrically non neutral ion cloud that is formed when the electrons are ripped away by the ponderomotive pressure of the laser radiation, and the inductive electric field generated due the fast change of the magnetic field during expansion of the magnetized plasma cloud. These three mechanisms work together with a continuous change from one to the other and provide an energy gain of the same order of magnitude.

We note that, when the high-energy cloud appears at the end of the channel, the electrons expand in vacuum faster than the ions. This forms an ion cloud with an unneutralized electric charge. It is easy to show that typical ion energy is equal to $\mathcal{E}_i \approx 4\pi^2 n e^2 R^2 \approx \pi m c^2 (R/d_e)^2$ in the relativistic case.

In the simulations presented above the ratio of the channel radius to the collisionless skin depth is about 10 to 30 which gives $\mathcal{E}_i \approx 300 mc^2$ to $\approx 900 mc^2$, in an agreement with the energy of fast ions seen in Fig. 2.

Now we consider the ion acceleration in the inductive electric field generated by the fast change of the magnetic field during expansion of the magnetized plasma cloud. As is seen in Figs. 1 and 2, the self-generated magnetic field vanishes at the axis and changes its sign in the upper and lower regions. When the electron–ion cloud leaves the channel, it carries a magnetic field B frozen into the plasma at a distance larger than the collisionless skin depth. In the expanding plasma the magnetic field decreases, and its value can be found from conservation of the magnetic flux: $\Phi = \pi L^2 B = \text{constant}$, where $L(t)$ is the cloud radius, which is equal to R at the end of the channel.

The change of the magnetic field leads to the generation of the electric field $E = \dot{L} B/c = \dot{L}\Phi/\pi L^2$ directed along the laser beam axis. This electric field accelerates the ions in the forward direction and slows down the electrons. A relativistic charged particle, accelerated in the vicinity of the axis, where it is not magnetized, acquires an energy

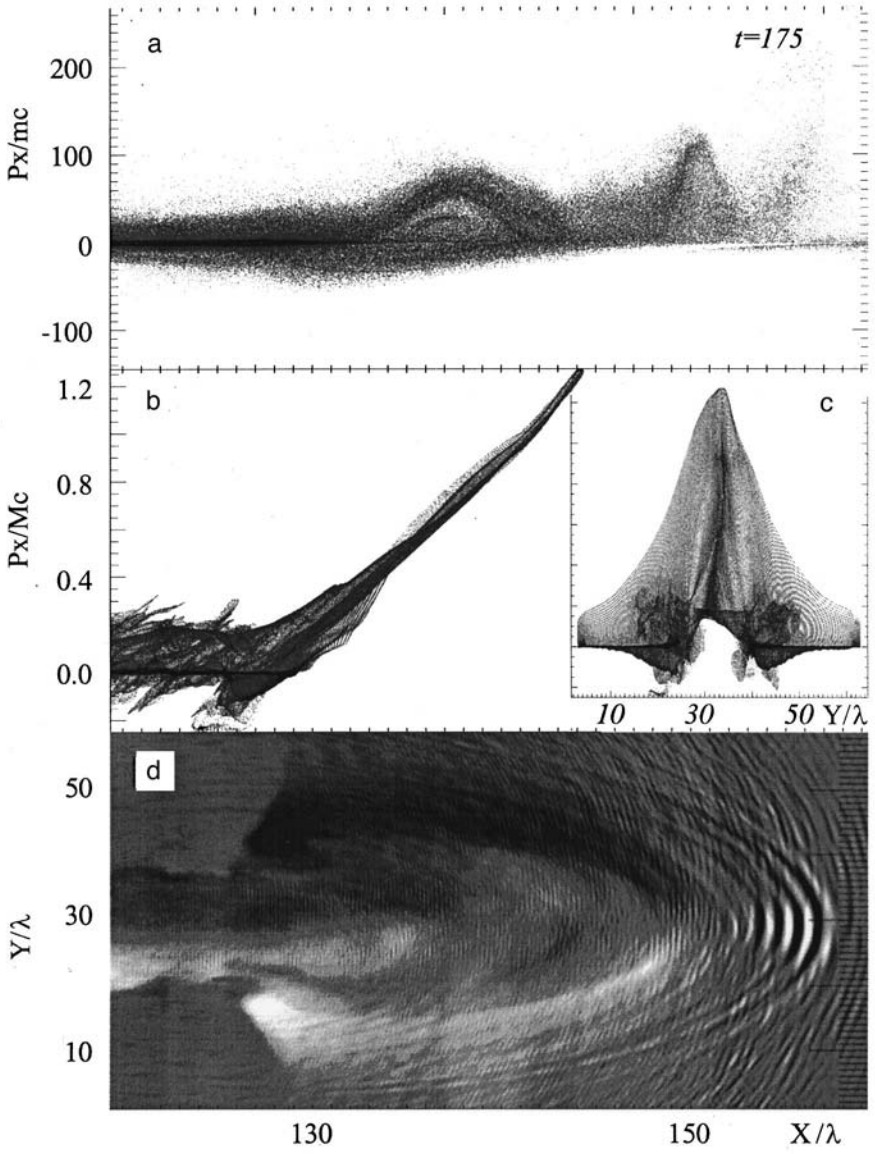

FIG. 2.

of the order of $\mathcal{E}_i \approx 8\pi n e^2 R^2$. Here we used the expression for the self-generated magnetic field $B = 4\pi n e R$ obtained in Ref. 9. We see that this energy is of the order of the energy gain during the Coulomb explosion.

Now we discuss the ion acceleration by an ultrarelativistic laser pulse interacting with a slab of overdense plasma. In this case the size of the simulation region is $12.4 \times 15\lambda^2$. The boundary conditions are periodic in the y direction for the particles and the electromagnetic field. The boundaries in the x direction are taken to be absorbing for

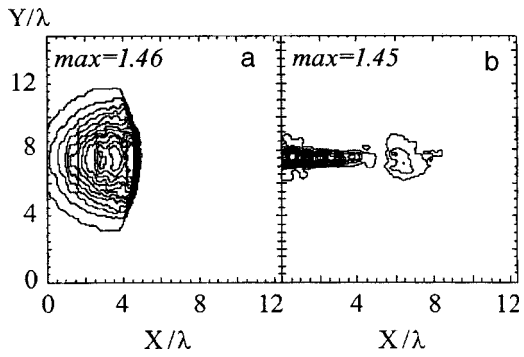

FIG. 3.

the electromagnetic waves, while the particles are reflected with the thermal velocity. The number of grid points and particles in the simulations is 850×1024 and 7.2×10^6. We performed PIC simulations for two different plasma configurations. In the first case a plasma slab (a thin foil) is localized initially at $5\lambda<x<7\lambda$. In the second case a foil of thickness 2λ in the central part is deformed into a parabola. The parabola is given (at $x<6\lambda$) by the formula $x=4\lambda+0.16(y-7.5\lambda)^2/\lambda$, and the curve is 2λ thick. In both cases the maximum plasma density is $n=30n_{\rm cr}$ and the plasma consists of protons (ion mass $M=1840\,$m) and electrons with an initial electron and ion temperature equal to 800 eV. We expect that in the case of the deformed foil, the high absorption of the obliquely incident *p*-polarized pulse and the additional focusing of the transmitted light should lead to a more effective ion acceleration than in the flat foil configuration.

An ultraintense *p*-polarized laser pulse is initiated at the left-hand side boundary. The pulse has a Gaussian profile both in the longitudinal and in the transverse direction. The pulse length and spot size (its width) are 5.5λ and 5λ, respectively. The normalized vector potential of the incident pulse is equal to $a_e=89$, and is larger than $\sqrt{M/m}\simeq43$. Thus we expect that the ions are accelerated to extremely high energy directly by the laser light. For a 1 μm laser, the intensity corresponds to $1.6\times10^{22}\,$W/cm^2 and the pulse length to 18 fs.

For the chosen parameters of the laser pulse and of the plasma the dimensionless parameter $\epsilon_0=\omega_{pe}^2 l_s/2\omega c$ [see (1)] is equal to 180. The normalized laser amplitude $a=89$ is smaller than ϵ_0. In this case, according to Ref. 7, the foil is not transparent to the laser radiation, and only a relatively small portion of the radiation can be transmitted through the foil.

The interaction of the laser pulse with the foil is shown in Fig. 3. Frame (a) shows the distribution of the electromagnetic energy density for $t=9(2\pi/\omega)$, and frame (b) shows it for $t=15(2\pi/\omega)$. The electromagnetic energy density is normalized by the peak value in the incident laser pulse. The contour levels vary from 0.1 to 1.2 with the interval 0.1. We see the deformation of the foil surface under the ponderomotive pressure, which pushes the electrons in the forward direction. A relatively small fraction of pulse is transmitted: the fraction of the transmitted and reflected energy is about 6.1% and 42.2%.

In Fig. 4 the phase plane of electrons with energies above 1.5 MeV is shown in frame (a) at $t=15(2\pi/\omega)$. We see that the electrons are accelerated in the forward

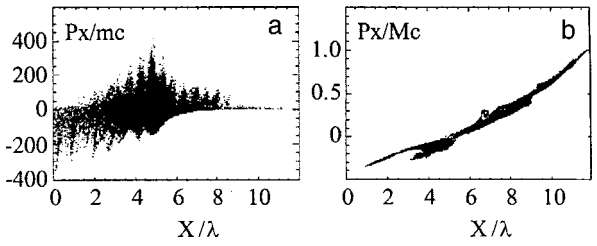

FIG. 4.

direction twice per laser period due to the $\mathbf{v}\times\mathbf{B}$ force,[10,11] and the energetic electrons are accelerated in the backward direction once per laser period, as was observed in Ref. 12. The phase plane of the fast ions is shown in Fig. 4b. We see that the ions are accelerated in both the backward and forward directions. The forward ion acceleration is predominant. The maximum momentum reached by the ions is $P_x/Mc\sim 1$, which corresponds to the GeV energy range. Also in this case the acceleration mechanism must be attributed to the Coulomb explosion, which gives a final ion energy of the order of $\mathcal{E}_C\approx 2\pi^2 e^2 n l_s l_\perp = 2\pi^3 mc^2(\omega_{pe}/\omega)^2(l_s l_\perp/\lambda^2)$. For the parameters of the simulations $\mathcal{E}_C\approx 2Mc^2$ i.e., ≈ 2 GeV.

The spatial distribution of the fast electrons and ions shown in Fig. 5, where we present the energy density of electrons (a) and ions (b) in the x,y plane at $t=15(2\pi/\omega)$. We see that the inside the plasma expanding in the forward direction the electron distribution is much less structured than the ion distribution. The ion density shows very clear filaments with a scale length of the order of the laser wavelength. In order to explain this structure we invoke the electromagnetic filamentation instability. In the expanding plasma the average energy of the electrons is approximately equal to the average ion energy. In this case the high-energy electrons move faster than the ions. As is well known, a plasma with relative motion of electrons and ions is unstable. This instability is similar to the electron filamentation instability considered in Ref. 13. It is easy to show that the growth rate of the filamentation instability is approximately equal to ω_{pi}.

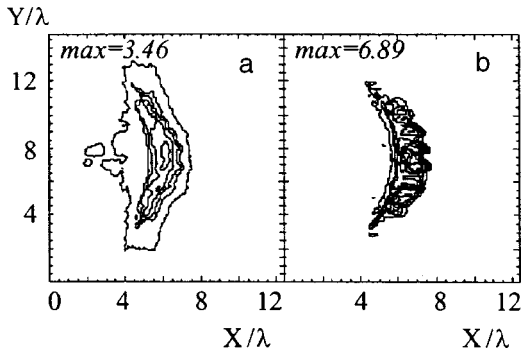

FIG. 5.

In summary, with the help of 2D3V-PIC simulations, we have investigated the ion acceleration during the interaction of petawatt laser pulses with underdense and overdense plasma slabs.

As to the ion acceleration in underdense plasmas, we emphasize that the ions are accelerated predominantly in the forward direction when the laser pulse reaches the end of the slab. In this case, the plasma filament formed at the channel axis begins to expand at the channel end. The high-energy electrons expand faster, and the ions that have been left behind form a well-collimated relativistically moving jet. The jet is confined in the transverse direction by the pinching in the self-generated magnetic field. In the longitudinal direction the ion jet expands because the electric charge is not neutralized inside the jet. We call this mechanism of ion acceleration ''anisotropic Coulomb explosion.'' For the parameters that are characteristic of the interaction of a petawatt laser pulse with a near critical plasma the ions gain a relativistic energy.

In the case of the interaction of petawatt laser with a thin slab of overdense plasma, the relativistic ions are also accelerated via the anisotropic Coulomb explosion. The magnetic pinching of the jet in the transverse direction can appear due to the electromagnetic filamentation instability.

The authors acknowledge helpful discussions with V. Yu. Bychenkov, H. Hojo, J. Koga, K. Nakajima, V. T. Tichonchuk and M. Yamagiwa. S. V. B and N. M. N. acknowledge the support of the Science and Technology Agency of Japan (STA).

[1] G. A. Mourou, C. P. J. Barty, and D. Perry, Phys. Today **51**(1), 22 (January 1998).
[2] A. V. Gurevich, L. V. Pariiskaya, and L. P. Pitaevskii, Zh. Éksp. Teor. Fiz. **49**, 647 (1965) [Sov. Phys. JETP **22**, 449 (1966)]; A. V. Gurevich and A. P. Meshcherkin, Zh. Eksp. Teor. Fiz. **80**, 1810 (1981) [Sov. Phys. JETP **53**, 937 (1981)].
[3] G. S. Sarkisov, V. Yu. Bychenkov, V. T. Tikhonchuk *et al.*, JETP Lett. **66**, 828 (1997).
[4] M. Lezius, S. Dobosz, D. Normand, and M. Schmidt, Phys. Rev. Lett. **80**, 261 (1998).
[5] F. N. Beg *et al.*, Phys. Plasmas **4**, 447 (1997); P. A. Norreys *et al.*, Plasma Phys. Controlled Fusion **40**, 175 (1998).
[6] V. Yu. Bychenkov, V. T. Tikhonchuk, and S. V. Tolokonnikov, JETP (1999), to be published.
[7] V. A. Vshivkov, N. M. Naumova, F. Pegoraro, and S. V. Bulanov, Phys. Plasmas **5**, 2727 (1998).
[8] G. A. Askar'yan, S. V. Bulanov, and I. V. Sokolov, Plasma Phys. Rep. **25**, 800 (1999).
[9] G. A. Askar'yan, S. V. Bulanov, F. Pegoraro, and A. M. Pukhov, JETP Lett. **60**, 251 (1994).
[10] S. C. Wilks, W. L. Kruer, M. Tabak, and A. B. Langdon, Phys. Rev. Lett. **69**, 1383 (1992).
[11] H. Ruhl, Y. Sentoku, K. Mima *et al.*, Phys. Rev. Lett. **82**, 743 (1999); Y. Sentoku, H. Ruhl, K. Mima *et al.*, submitted to Phys. Plasmas.
[12] Y. Sentoku, K. Mima, T. Taguchi *et al.*, Phys. Plasmas **5**, 4366 (1998).
[13] F. Califano, F. Pegoraro, S. V. Bulanov, and A. Mangeney, Phys. Rev. E **57**, 7048 (1998); F. Califano, R. Prandi, F. Pegoraro, and S. V. Bulanov, Phys. Rev. E **58**, 7837 (1998).

Published in English in the original Russian journal. Edited by Steve Torstveit.

Anomalous Hall effect in granular Fe/SiO_2 films in the tunneling-conduction regime

B. A. Aronzon, D. Yu. Kovalev, A. N. Lagar'kov, E. Z. Meilikhov, V. V. Ryl'kov, M. A. Sedova, N. Negre, M. Goiran, and J. Leotin

Kurchatov Institute Russian Science Center, 123182 Moscow, Russia; Scientific-Research Center for Applied Electrodynamics, 127412 Moscow, Russia; LPMC and SNCMP, 31077 Toulouse Cedex, France

(Submitted 21 May 1999)
Pis'ma Zh. Éksp. Teor. Fiz. **70**, No. 2, 87–92 (25 July 1999)

It is established that the Hall effect in Fe/SiO_2 nanocomposite films in the activational tunneling conduction range is anomalous, i.e., the Hall resistivity ρ_h is proportional to the magnetization and is due to the spin–orbit interaction. The parametric coupling of the Hall and longitudinal (ρ_{xx}) resistances $\rho_h \propto \rho_{xx}^m$ (with temperature as the parameter) is characterized by a much lower value of the exponent m than in a uniform ferromagnetic metal. This circumstance is attributed to the characteristic features of the Hall effect mechanism in the hopping regime — in our case, the interference of the amplitudes of tunneling transitions in a set of three granules. © *1999 American Institute of Physics.* [S0021-3640(99)00514-9]

PACS numbers: 73.50.Jt, 81.05.Ys, 61.43.Er

In recent years there has been appreciable interest in composites, based on ferromagnetic nanoparticles, in which a giant magnetoresistance (GMR)[1,2] and a giant Hall effect (GHE)[3,4] are observed. A specific feature of ferromagnetic metals is that their Hall resistivity

$$\rho_h = R_0 B + R_s 4\pi M \tag{1}$$

possesses two components, one of which (the normal part) is due to the Lorentz force and is proportional to the magnetic induction B, while the other (the anomalous part) is proportional to the magnetization M (R_0 and R_s are the corresponding normal and anomalous Hall effect constants). The latter is related with the influence of the spin–orbit interaction (SOI) on the scattering of spin-polarized electrons and is much greater than the normal component.[5] Specifically, it has been established[3,4] for the granular system $(NiFe)_x/(SiO_2)_{1-x}$ that the anomalous Hall effect (AHE) constant R_s is two orders of magnitude greater than R_0 and can be four orders of magnitude greater than its value for a uniform metal ($x=1$). However, even though the Hall effect in these materials is quite strong, the experiments performed thus far[3,4] have been concerned only with the GHE on the metallic side of the percolation transition.

Physically, it is of greatest interest to study the GHE in the range of compositions of the composite where the GMR effect is strongest,[1,2] i.e., in the insulating phase. On the

basis of an analogy with semiconductors, where the transition to hopping conduction is accompanied by a change in the Hall effect mechanism, a change in the AHE mechanism can also be expected in a nanocomposite. Indeed, Holstein[6] showed that the probability of a tunneling transition between two centers does not contain corrections which are linear in the magnetic field. Therefore to describe the Hall effect it is necessary to consider at least three centers and to take into account the possibility of indirect tunneling transitions.[6] As a result, the relation between the Hall and longitudinal resistances becomes weaker, $\rho_h \propto (\rho_{xx})^m$, where the exponent $m<1$. Specifically, the value $m=0.35$ is predicted for conduction with a variable hopping length, and $m=0.5$ is predicted for conduction with a constant activation energy,[7] which is appreciably less than for the ordinary band conduction $(m=1)$.

Tunneling conduction in magnetic composite materials likewise does not contain a term that is linear in the magnetic field. However, we know of no experimental works devoted to the description of the AHE under these conditions.

Therefore it is entirely appropriate and interesting to explore the question of whether or not an AHE can exist in the tunneling transport and how this effect would behave in real systems based on magnetic nanocomposites.

The absence of systematic experimental data on the Hall effect in magnetic nanocomposites in the insulating region is due to the high noise level characteristic of systems with percolation conduction and to the parasitic effect of the GMR that arises under these conditions and is associated with the asymmetry in the arrangement of the Hall probes. In the present work we investigated the characteristic features of the Hall effect in samples based on Fe/SiO_2 films with very small asymmetry of the Hall probes, using digital methods of signal acquisition and filtering, which made it possible to record the change in the asymmetry resistance in a magnetic field at the level $\sim 10^{-2}\%$.

The samples, fitted with a pair of current contacts and two pairs of potential (Hall) probes, were prepared in the standard double-cross geometry. The width of the conducting channel was $W=2$ mm, its length was $L=7$ mm, and the accuracy with which the Hall probes were combined was of the order of 10 μm.

The samples were obtained by combined ion-beam sputtering of Fe and SiO_2 using a composite target on Polikor substrates at room temperature. The characteristic size of the granules was several nanometers; the film thickness d was varied in the range $0.2-0.8\,\mu$m.[8] It is important to note that when the films were deposited on a heated substrate (up to $T=250\,^{\circ}$C), not only did the average granule size increase (by a factor of ~ 2), but the Fe content in the samples increased quite appreciably (severalfold according to data from electronic photographs). This indicated a variance in the granule sizes and the existence of small particles which cannot be resolved in an electron microscope. This circumstance is apparently inherent to a large class of granular systems, as is attested to by the results of recent investigations on films of $NiFe/SiO_2$ (Ref. 4), Co/AlO (Ref. 2), and Cu/SiO_2 (Ref. 9).

In Ref. 8 it was established that the transition to activational hopping conduction occurs in the samples with volume iron content $x<x_c\approx 0.6$. In this range the films demonstrate in the direct vicinity of the percolation transition a quite high negative GMR, reaching 5%,[8] which is appreciably greater than for the Ni/SiO_2 system[10] and close to the value 4.5% obtained in Ref. 1 for the system Co/SiO_2.

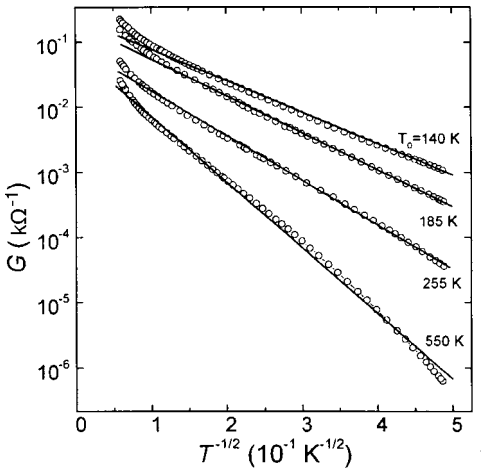

FIG. 1. Temperature dependences of the conductance G of insulating samples with various compositions close to the percolation threshold. T_0, K: *1* — 140, *2* — 185, *3* — 255, *4* — 550.

Hall effect measurements were performed in magnetic fields up to 10 kOe at temperatures $T=77-300$ K in the constant-voltage regime. Preliminary investigations showed that near the metal–insulator transition ($x\leqslant 0.6$) the Hall effect depends quite strongly on the Fe content. The accuracy ($\sim 10\%$)[8] with which the composition was determined is obviously inadequate for studying trends in the behavior of the Hall effect in the insulating region.

Figure 1 shows the temperature dependences $G(T)$ in the often used coordinates $\log(G)$ versus $T^{-1/2}$ for several samples with iron content $x\leqslant 0.6$. The strong decrease in G with decreasing temperature attests to activational conduction. In our case the relative decrease of G as T decreases from 300 to 4.2 K reaches four orders of magnitude, while for samples with metallic conduction, which were investigated in Refs. 3 and 4, it did not exceed 2. These dependences are close to linear right down to $T\approx 6$ K. According to Ref. 11 this is most likely due to the exponentially wide size distribution of the granules, for which the conductance follows the ''1/2 law'': $G(T)=G_0\exp[-(T_0/T)^{1/2}]$, where the parameter T_0 is determined by the metal content:

$$kT_0\approx(e^2/\epsilon\alpha_0)(a_0/\lambda)^{3/2}\psi(x), \quad \psi(x)=x^{-1/2}[1-(x/x_c)^{1/3}]. \tag{2}$$

Here ϵ is the dielectric constant, λ is the decay length of the electron wave function in the insulator, and a_0 is the characteristic size of granules. The values found for T_0 are presented in the caption to Fig. 1. Estimates based on Eq. (2) show that although the parameter T_0 changes appreciably, the variation of x in our case does not exceed 0.01, i.e., less than 5% for $x_c=0.6$. In other words, near a transition T_0 is a much more reliable characteristic of the closeness of samples to a percolation transition than x is, and therefore it is natural to characterize the samples additionally by the parameter T_0.

The Hall resistance R_h was determined according to the difference of the values of the transverse resistance $R_{xy}=V_y/I_x$ corresponding to positive (R_{xy}^+) and negative (R_{xy}^-)

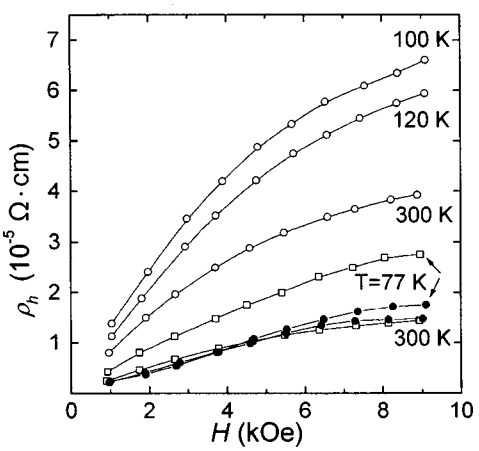

FIG. 2. Magnetic-field dependences of the Hall resistivity ρ_h of samples with dielectric [$T_0=255$ K(○) and $T_0=140$ K(□)] and metallic [$x\approx 0.7$ (●)] conduction at different temperatures T, K: *1* — 77, *2* — 100, *3* — 120, and *4* — 300.

directions of the magnetic field: $R_h=(R_{xy}^{+}-R_{xy}^{-})/2$. The sign of the Hall effect was established using a standard sample. For all samples it was positive, just as for single-crystal iron.[12]

Figure 2 shows the field dependences of the Hall resistivity $\rho_h(H)=R_h(H)d$ at various temperatures for an insulating sample with $T_0=255$ K (unfilled circles). The figure also shows for comparison the curves $\rho_h(H)$ for an insulating sample closest to the percolation transition ($T_0=140$ K, squares) and for a sample with metallic conduction ($x\approx 0.7$, filled circles). One can see that in the last two cases the forms of the dependences are close, and the curves $\rho_h(H)$ saturate appreciably in fields ≈ 10 kOe, as is typical for ferromagnetic materials with metallic conductance under conditions where the AHE is proportional to the magnetization.[3–5] However, ρ_h for an insulating sample grows much more strongly with decreasing temperature. That is, the fact that in these samples the values of ρ_h are the same at $T=300$ K is most likely accidental.

Another interesting fact is that as the Fe content decreases, the dependence $\rho_h(H)$ becomes more ''rounded'' (compare the $\rho_h(H)$ curves for insulating samples in Fig. 2 at $T=300$ K). It is important that the form of the magnetization curve $M(H)$ also changes analogously as the metal fraction decreases: It transforms into a more ''rounded'' Langevin function.[10] To establish the relation between $\rho_h(H)$ and $M(H)$ we prepared two identical samples ($T_0=150$ K), one of which (the Hall sample) served to study the field dependence $\rho_h(H)$ and the other for measuring the magnetization by the magnetooptic Kerr effect method.[10] The results of the measurements at $T=77$ and 300 K are presented in Fig. 3.[1)] It is seen from the figure that the field dependences $\rho_h(H)$ and $M(H)$ are identical, just as in ferromagnetic metals. However, we note that the anomalous Hall effect coefficient $R_s=\rho_h(H)/M(H)$ reaches at $T=77$ K the value (see inset) $1.6\times 10^{-7}\,\Omega\cdot$cm/G, which is five orders of magnitude greater than the value of R_s in bulk iron.[10] Since ρ_h increases (see Fig. 2) and M decreases as x decreases, R_s can be expected to be even greater in the more highly insulating samples. Such a strong increase is

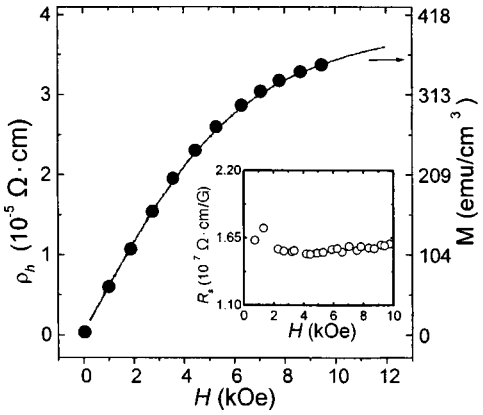

FIG. 3. Magnetic-field dependences of the Hall resistivity ρ_h (●) and magnetization M (solid curve) at $T=300$ K. Inset: Magnetic-field dependence of the anomalous Hall coefficient R_s at $T=77$ K.

impossible to explain by studying the Hall effect in individual granules.[3,4]

Finally, we consider the parametric dependence of the Hall resistance on the longitudinal resistance (with temperature as the parameter) for insulating samples (Fig. 4). It is evident that for all samples R_h increases with R_{xx} (i.e., with decreasing temperature). Approximating the dependence by a power-law function $R_h \propto R_{xx}^m$ we found $m=0.44-0.59$ with the average value $m\approx 0.5$, which is appreciably smaller than the value following from models of the AHE in ferromagnetic metals[5] ($m=1$ for asymmetric scattering, or $m=2$ in the case of lateral hops).

The fact that the sign of the Hall effect and the proportionality between $\rho_h(H)$ and $M(H)$ are preserved in the insulating region signifies that in our case the Hall effect is anomalous. At the same time the giant value of R_s and the appreciable difference ap-

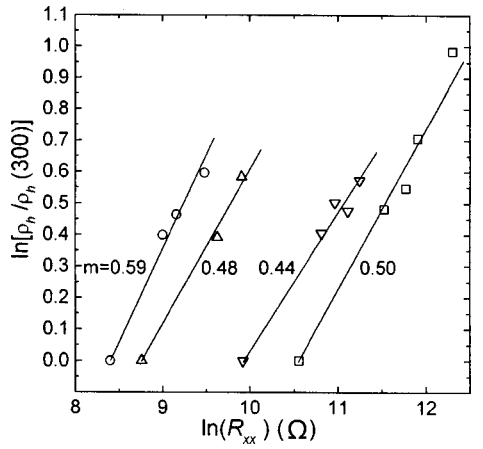

FIG. 4. Parametric dependences $\rho_h(R_{xx})$ for insulating samples for which the temperature dependences of the conductance are presented in Fig. 1. The parameter is the temperature, which varies in the range $T=77-300$ K.

pearing in the temperature dependences of the Hall and longitudinal resistances in the insulating phase indicate that the tunneling character of the conduction plays the determining role and, in consequence, that the mechanism of the Hall effect becomes qualitatively different. We assume that the Hall effect is due to interference of the amplitudes of tunneling transitions in a set of three or more granules, but it occurs not under the influence of the magnetic induction B, as in the case of semiconductors with hopping conduction, but rather under the influence of the magnetization under SOI conditions. The general approach developed in Ref. 6 to study the Hall effect remains in force, the only difference being that in our case the size variance of the granules must be taken into account. However, this circumstance can substantially alter the behavior of the Hall resistance as a function of temperature. We shall explain this for the simple example of the ordinary Hall effect. The extension to the case of the AHE presents no difficulties, if the formalism proposed in Ref. 13 is followed and the fact that the ordinary and anomalous Hall effects additively determine the Hall resistance [see Eq. (1)] is taken into account.

In Ref. 6 it is shown that a configuration consisting of three centers must be considered (in our case — a configuration of three granules) in order to describe the Hall effect. It turns out that the correction linear in the magnetic field to the probability of electron tunneling between two centers ($i \rightarrow j$) appears only as a result of interference effects which arise when the two-stage tunneling transition through a third center ($i \rightarrow p \rightarrow j$) is taken into account. Averaging over all possible ''triangular'' configurations shows that a Hall current $\mathbf{j}_H = [\mathbf{E} \times \mathbf{h}]/\rho_h$, where $\mathbf{h} = \mathbf{B}/B$ is a unit vector in the direction of the magnetic field, appears in a nonzero electric field.

In Ref. 6 it was also shown that triangular configurations of centers (granules) in the form of an equilateral triangle make the main contribution to the Hall conductance. By analogy to Ref. 11 it can be assumed that for a large variance of the granule sizes, only granules of approximately the same (optimal) size a_H participate in Hall current transport. Then only triangular configurations with a definite edge length l, equal in order of magnitude to the average distance between granules with sizes close to a_H, are important. In this approximation the Hall resistivity ρ_h can be represented as[14]

$$\rho_h \propto \frac{\rho_{ip}\rho_{pj}\rho_{ji}}{\rho_{ip}+\rho_{pj}+\rho_{ji}} W_{ipj}, \tag{3}$$

where

$$\rho_{ip} \propto \exp(2l_H/\lambda + w_H/kT) \tag{4}$$

is the resistivity of the tunneling transition $i \rightarrow p$, $W_{ipj} \propto \exp(-3l_H/\lambda - w_H/kT)$ is the interference amplitude in a unit magnetic field, and $w_h = (e^2/\epsilon a_H)[1-(x/x_c)^{1/3}]$ is the activation energy of the electronic transition between two initially neutral granules.[11] Therefore

$$\rho_H \propto \exp(l_H/\lambda + w_H/kT). \tag{5}$$

Analysis of a system with a wide variance of granule sizes shows[11] that when the impedance of an individual tunneling transition is given by the relation (4), the tempera-

ture dependence of the resistance of a nanocomposite can be described by the ''1/2 law'' with characteristic temperature $T_0 \propto \lambda^{-3/2}$. The temperature dependence of the Hall resistivity is described by the same law

$$\rho_H \propto \exp[(T_H/T)^{1/2}], \tag{6}$$

where, however, the characteristic temperature must be ''corrected'' for the difference between the relations (4) and (5): $T_H = 2^{-3/2} T_0 \approx T_0/3$. This leads to the scaling relation $\rho_H \propto \rho_{xx}^m$, $m \approx 0.6$, which agrees with the relation found experimentally (see Fig. 4).

In summary, in the present work the anomalous Hall effect in the insulating phase of a magnetic nanocomposite with tunneling conduction was investigated experimentally and qualitative arguments explaining its nature were presented. The similarity of the magnetic field dependences of the Hall effect and of the magnetization proves the anomalous nature of the effect, and the form of its temperature dependence proves that the tunneling mechanism plays the governing role.

This work was supported by the Russian Fund for Fundamental Research (Grants 99-02-16955 and 98-02-17628) and by the Russian-French Fund PICS.

[1)]The relative magnetooptic measurements were calibrated by ''matching'' with the results of absolute SQUID measurements in ≈ 5 T fields.

[1] A. Milner, A. Gerber, B. Groisman *et al.*, Phys. Rev. Lett. **76**, 475 (1996).
[2] S. Mitani, S. Takahashi, K. Takanashi *et al.*, Phys. Rev. Lett. **81**, 2799 (1998).
[3] A. B. Pakhomov, and X. Yan, Solid State Commun. **99**, 139 (1996).
[4] A. B. Pakhomov, X. Yan, N. Wang *et al.*, Physica A **241**, 344 (1997).
[5] A. V. Vedyaev, A. B. Granovskiĭ, and O. A. Kotel'nikova, *Transport Phenomena in Disordered Ferromagnetic Alloys* [in Russian] (Moscow State University Press, Moscow, 1992).
[6] T. Holstein, Phys. Rev. **124**, 1329 (1961).
[7] R. Nemeth and B. Ṃuhlshlegel, Solid State Commun. **66**, 999 (1988); Yu. M. Gal'perin, E. P. German, and V. G. Karpov, Zh. Éksp. Teor. Fiz. **99**, 343 (1991) [Sov. Phys. JETP **72**, 193 (1991)].
[8] B. A. Aronzon, A. E. Varfolomeev, D. Yu. Kovalev *et al.*, Fiz. Tverd. Tela (St. Petersburg) **41**(6), 944 (1999) [Phys. Solid State **41**, 857 (1999)].
[9] S. A. Gurevich, T. A. Zaraĭskaya, S. G. Konnikov *et al.*, Fiz. Tverd. Tela (St. Petersburg) **39**(10), 1889 (1997) [Phys. Solid State **39**, 1691 (1997)].
[10] J. L. Gittleman, Y. Goldstein, and S. Bozovski, Phys. Rev. B **5**, 3609 (1972).
[11] E. Z. Meĭlikhov, Zh. Éksp. Teor. Fiz. **115**, 1484 (1999) [JETP **88**, 819 (1999)].
[12] *Handbook of Physical Quantities*, edited by I. S. Grigoriev and E. Z. Meilikhov (CRC Press, Boca Raton, 1997), p. 902.
[13] A. V. Vedyaev and A. B. Granovskiĭ, Fiz. Tverd. Tela (Leningrad) **28**, 2310 (1986) [Sov. Phys. Solid State **28**, 1293 (1986)].
[14] M. Gruenewald, H. Mueller, P. Thomas, and D. Wuertz, Solid State Commun. **38**, 1011 (1981); M. Nissim, and R. L. Rosenbaum, Phys. Rev. B **40**, 10629 (1989).

Translated by M. E. Alferieff

Two-dimensional quantum interference contributions to the magnetoresistance of $Nd_{2-x}Ce_xCuO_{4-\delta}$ single crystals

G. I. Harus, A. N. Ignatenkov, A. I. Ponomarev, L. D. Sabirzyanova, and N. G. Shelushinina

Institute of Metal Physics, Urals Branch of the Russian Academy of Sciences, 620219 Ekaterinburg, Russia

N. A. Babushkina

RSC Kurchatov Institute, 123182 Moscow, Russia

(Submitted 23 December 1998; resubmitted 8 June 1999)
Pis'ma Zh. Éksp. Teor. Fiz. **70**, No. 2, 93–99 (25 July 1999)

Two-dimensional (2D) weak localization effects at low temperatures $T=0.2$–4.2 K are investigated in a nonsuperconducting sample $Nd_{1.88}Ce_{0.12}CuO_{4-\delta}$ and in the normal state of a superconducting sample $Nd_{1.82}Ce_{0.18}CuO_{4-\delta}$ for $B>B_{c2}\simeq 3$ T. The phase coherence time τ_φ ($\simeq 5\times 10^{-11}$ s at 1.9 K) and the effective thickness d of a conducting CuO_2 layer ($\simeq 1.5$ Å) are estimated by fitting the expressions from the 2D weak localization theory to the magnetoresistivity data for the normal-to-plane and in-plane magnetic fields. The estimated value of the parameter d ensures the condition of strong carrier confinement and justifies a model of almost decoupled 2D metallic sheets for the $Nd_{2-x}Ce_xCuO_{4-\delta}$ single crystals. © *1999 American Institute of Physics.* [S0021-3640(99)00614-3]

PACS numbers: 74.25.Ha, 74.72.Jt, 72.15.Rn, 72.15.Gd

INTRODUCTION

The crystallographic structure T' of $Nd_{2-x}Ce_xCuO_{4-\delta}$ is the simplest among the superconducting cuprates: each copper atom is coordinated to four oxygen atoms in a planar structure without apical oxygen. The Nd_2CuO_4 crystal is an insulator, with the valence band being mainly of O $2p$ character and the empty conduction band being the upper Hubbard Cu $3d$ band. The $3d$–$3d$ Coulomb repulsion U at the Cu site is strong ($\simeq 6$–7 eV) and is larger than the oxygen-to-metal charge-transfer energy D($\simeq 1$–2 eV). Thus these cuprates are classified as charge-transfer semiconductors.

The combination of Ce doping and O reduction results in *n*-type conduction in the CuO_2 layers. The energy band structure calculation[1] shows that the Fermi level is located in a band of the $pd\sigma$ type formed by the $3d(x^2-y^2)$ orbitals of Cu and the $p_\sigma(x,y)$ orbitals of oxygen. The $pd\sigma$ band appears to be of highly 2D character with almost no dispersion in the z direction, which is normal to CuO_2 planes. The electrons are concen-

trated within the confines of conducting CuO_2 layers separated from each other by a distance $c \simeq 6$ Å.

Due to the layered crystal structure the high-T_c copper oxide compounds have highly anisotropic electrical properties in the normal state. The electron-doped systems $Nd_{2-x}Ce_xCuO_{4-\delta}$ exhibit a very large anisotropy factor, $\rho_c/\rho_{ab} \geqslant 10^4$ (Refs. 2 and 3), which is somewhat lower than in the Bi systems ($\rho_c/\rho_{ab} \sim 10^5$) but substantially higher than in the La and Y systems ($\rho_c/\rho_{ab} \sim 10^2$). For the underdoped and optimally doped compounds the *c*-axis resistivity ρ_c is usually nonmetallic ($d\rho_c/dT \leqslant 0$) at low enough temperatures.[4] In contrast, the magnitude and the temperature dependence of the resistivity in the CuO_2 plane, ρ_{ab}, are in general metallic near optimum doping.

A 2D metallic state in a system with random disorder should exhibit weak localization of the charge carriers at low temperatures.[5] Weak localization behavior of the in-plane resistivity has been clearly observed and perfectly analyzed for the $Bi_2Sr_2CuO_6$ systems, which were investigated with high precision at T down to 0.5 K in magnetic fields of up to 8 T normal to and perpendicular to the CuO_2 planes.[6] As to the $La_{2-x}Sr_xCuO_{4-\delta}$ and $La_{2-x}Ba_xCuO_{4-\delta}$ systems, the concentration range between the hopping regime at low x and the superconducting regime at $x > 0.05$ seems to be so narrow that a well-defined weak localization behavior is difficult to observe.[7,8] Only in the close proximity to $x = 0.05$ do the nonsuperconducting sample $La_{2-x}Ba_xCuO_{4-\delta}$ (Ref. 7) and the superconducting sample $La_{2-x}Sr_xCuO_{4-\delta}$ ($T_c = 4$ K) display some signs of weak localization ($\ln T$ dependence of ρ_{ab}) in fields $B > 8$ T.

Due to their T' structure the Nd systems should be particularly advantageous for the observation of 2D effects in conduction process. Indeed, there are several reports on the manifestation of 2D weak localization in the in-plane conductance of $Nd_{2-x}Ce_xCuO_{4-\delta}$ single crystals and films. Thus a linear dependence of resistivity on $\ln T$ comes about at $T < T_c$ for samples with $x \cong 0.15$, in which the superconducting state is destroyed by a magnetic field.[9] Furthermore, a highly anisotropic (with regard to the magnetic field direction) negative magnetoresistance, predicted for 2D weak localization, has been observed in the nonsuperconducting state at low temperatures: in a highly underdoped sample with $x = 0.01$ (Ref. 10) and in unreduced samples with $x = 0.15$ (Ref. 11) or $x = 0.18$ (Ref. 12). Measurements in a superconducting $x = 0.15$ sample with high T_c ($T_c = 20$ K) has shown a similar negative magnetoresistance in high (up to 30 T) transverse magnetic fields and an upturn in the normal state resistance as T is lowered.[11]

In our previous investigation of the sample with $x = 0.18$ ($T_c = 6$ K) a negative magnetoresistance was observed after the destruction of superconductivity by a magnetic field up to 5.5 T at $T \leqslant 1.4$ K.[11] We report here the results of measurements at much lower temperatures (down to 0.2 K) and in higher dc magnetic fields (up to 12 T). A drastic dependence of the magnitude of the magnetoresistance on the direction of the magnetic field is the most important experimental test for the 2D character of a conducting system. For investigation of the magnetoresistance anisotropy we have used here the measurements on a nonsuperconducting sample with an x value ($x = 0.12$) close to the boundary value $x = 0.14$ for the superconductivity in a $Nd_{2-x}Ce_xCuO_{4-\delta}$ system.

RESULTS

High-quality single-phase $Nd_{2-x}Ce_xCuO_{4-\delta}$ ($x = 0.12$–0.20) thin films were produced by a modified laser deposition technique with flux separation.[14] Films with thick-

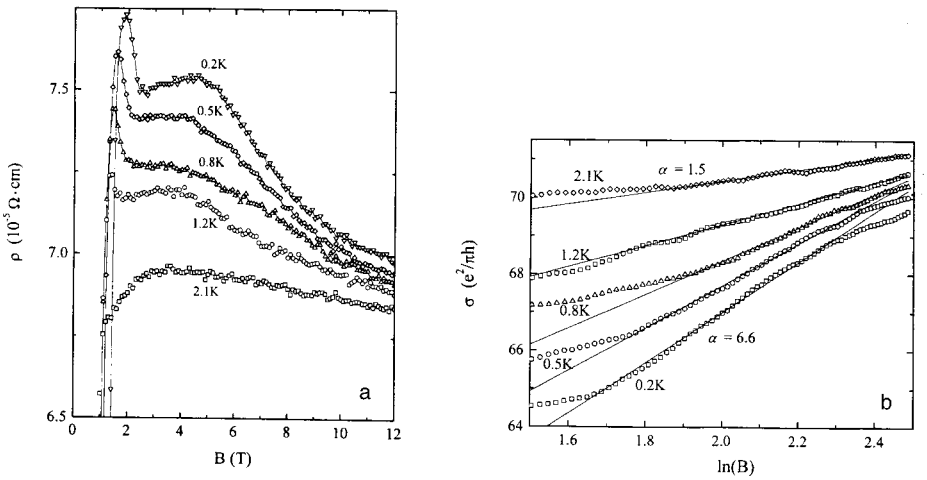

FIG. 1. a: Resistivity as a function of magnetic field at different temperatures for the sample with $x=0.18$. b: Surface conductivity as a function of ln$B$ for the sample with $x=0.18$.

nesses of around 5000 Å were deposited onto a hot $SrTiO_2$ single-crystal substrate having the (100) surface orientation. It was necessary to anneal the films subsequently at 800 °C for 40 min in a vacuum $< 10^{-2}$ torr to form the superconducting phase. The x-ray diffraction study has revealed the existence of the tetragonal phase only with the c axis perpendicular to the film plane. We report here the data for $Nd_{2-x}Ce_xCuO_{4-\delta}$ films with $x=0.12$ and 0.18 only.

The in-plane resistivity ρ_{ab} and Hall coefficient R ($\mathbf{j}\|ab, \mathbf{B}\|c$) were investigated in a single-crystal superconducting film $Nd_{1.82}Ce_{0.18}CuO_{4-\delta}$ ($T_c=6$ K) at $T=(0.2–20)$ K in a magnetic field up to $B=12$ T. In the superconducting sample the normal-state transport at low T is hidden unless a magnetic field B higher than the second critical field B_{c2} is applied (for $B\perp ab$ one has $B_{c2}\cong 3$ T at $T=4.2$ K). We destroyed the superconductivity by a magnetic field perpendicular to the CuO_2 planes and observed a negative magnetoresistance in fields higher than B_{c2} (Fig. 1) with a logarithmic temperature dependence of the resistivity at $T<4.5$ K (Fig. 2). Figure 3 shows the results of measurements of the in-plane conductivity in a nonsuperconducting sample $Nd_{1.88}Ce_{0.12}CuO_{4-\delta}$ at $T=1.9$ K and 4.2 K for magnetic fields perpendicular $B_\perp$ and parallel $B_\|$ to the CuO_2 planes, with inductions up to $B=5.5$ T.

DISCUSSION

The logarithmic low-temperature dependence of the conductivity is one of the indications of the interference quantum correction due to weak localization or electron–electron interaction in a 2D system. A magnetic field normal to the motion of a carrier destroys the interference leading to localization. In a 2D system it causes negative magnetoresistance in the case when the field is perpendicular to the plane, but there is no effect for the parallel configuration. In the 2D weak localization theory the quantum correction to the Drude surface conductivity in a perpendicular magnetic field is given by[15]

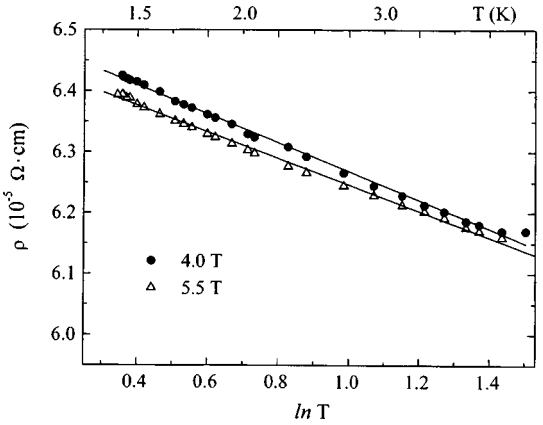

FIG. 2. Logarithmic temperature dependence of the resistivity at $B > B_{c2}$ ($x = 0.18$).

$$\Delta\sigma_s(B_\perp) = \alpha\frac{e^2}{\pi h}\left\{\Psi\left(\frac{1}{2}+\frac{B_\varphi}{B_\perp}\right)-\Psi\left(\frac{1}{2}+\frac{B_{\rm tr}}{B_\perp}\right)\right\}, \tag{1}$$

where α is a prefactor of the order of unity, Ψ is the digamma function, $B_\varphi = c\hbar/4eL_\varphi^2$, and $B_{\rm tr} = c\hbar/2e\ell^2$. Here $L_\varphi = \sqrt{D\tau_\varphi}$ is the phase coherence length (D is the diffusion coefficient and τ_φ is the phase breaking time) and ℓ is the mean free path. At low temperature the inequality $B_\varphi \ll B_{\rm tr}$ ($L_\varphi \gg \ell$) is valid, and thus the weak localization effects are almost totally suppressed for $B \cong B_{\rm tr}$. Let us compare the equation for the transport field, presented in the form

$$2\pi B_{\rm tr}\ell^2 = \Phi_0, \tag{2}$$

where $\Phi_0 = \pi c\hbar/e$ is the elementary flux quantum, with the relation between the coherence length ξ and the second critical field in the so called ''dirty'' limit ($\xi \gg \ell$):

$$2\pi B_{c2}\ell\xi = \Phi_0. \tag{3}$$

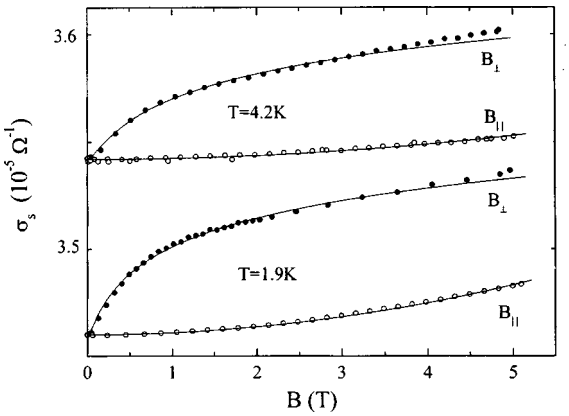

FIG. 3. Surface conductivity as a function of magnetic field ($x = 0.12$).

From Eqs. (2) and (3) one has $B_{tr}/B_{c2}=\xi/\ell$, and thus the inequality $B_{tr}\gg B_{c2}$ should be valid for any dirty superconductor.

SUPERCONDUCTING SAMPLE ($x=0.18$)

From the experimental values of ρ_{ab} and Hall constant R in the normal state we have obtained the Drude conductivity of a CuO_2 layer $\sigma_s=(\rho_{ab}/c)^{-1}$ and the bulk $n=(eR)^{-1}$ and surface $n_s=nc$ electron densities ($c=6$ Å is the distance between CuO_2 layers). We have $\sigma_s=10^{-3}\,\Omega^{-1}$, $n=1.1\times10^{22}\text{cm}^{-3}$, and $n_s=6.6\times10^{14}\text{cm}^{-2}$ at $T=4.2$ K and $B>B_{c2}$. Using the relation $\sigma_s=(e^2/h)k_F\ell$, with k_F the Fermi wave vector, we have estimated the parameter $k_F\ell\cong25$. Since $k_F\ell\gg1$, a true metallic conduction in the CuO_2 layers takes place.

Since $k_F=(2\pi n_s)^{1/2}\cong6\times10^7\ \text{cm}^{-1}$, we have found that the mean free path $\ell\cong4\times10^{-7}$cm, and according to Eq. (2), the transport field $B_{tr}\simeq20$ T. In the investigated sample the second critical field $B_{c2}\simeq3$ T at $T=4.2$ K (Ref. 13) and $B_{c2}\simeq5\,T$ at $T=0.2$ K. Thus we have $B_{tr}\gg B_{c2}$, and it turns out to be possible to observe the negative magnetoresistance owing to 2D weak localization in the interval of magnetic fields $B_{c2}<B_\perp<B_{tr}$ (Fig. 1a).

In the field range $B_\varphi\ll B\ll B_{tr}$ the expression (1) may be written as

$$\Delta\sigma_s(B_\perp)=\alpha\frac{e^2}{\pi h}\left\{-\Psi\left(\frac{1}{2}\right)-\ln\frac{B_\perp}{B_{tr}}\right\}. \tag{4}$$

Figure 1b shows the surface conductivity σ_s as a function of $\ln B$. It is seen that at $B>B_{c2}$ the experimental data can be described by simple formula (4) with the prefactor α as the only fitting parameter. At $T=2$ K we have $\alpha=1.5$, but as the temperature is lowered the α value becomes substantially greater than unity: $\alpha=6.6$ at $T=0.2$ K. Thus the negative magnetoresistance effect at the lowest temperature is too large to be caused solely by the suppression of weak localization.

In the case of effective electron attraction there exists another orbital contribution to the negative magnetoresistance, namely, the contribution due to the disorder-modified electron–electron interaction in the so-called Cooper channel (the interaction of electrons with opposite momenta).[16] A contribution such as that may be the cause of the extra negative magnetoresistance in our *in situ* superconducting sample at very low temperatures. The magnitudes of the coefficient of $\ln B$ in superconducting aluminum films at $T>T_c$ have been quantitatively explained in just this way.[17]

When the magnetic field is applied parallel to the ab plane, it turns out that the upper critical field, $B_{c2}^{\parallel}$, is too high and is not reached in our sample with $x=0.18$ in fields up to $B=12$ T. This result is in accordance with the observation of a large anisotropy of B_{c2} for $Nd_{2-x}Ce_xCuO_{4-\delta}$ single crystals with $x=0.16$ ($B_{c2}^{\perp}=6.7$ T, $B_{c2}^{\parallel}=137$ T).[18] Thus in order to investigate the dependence of magnetoresistance on the direction of the magnetic field relative to the CuO_2 plane, a study of an *in situ* nonsuperconducting sample is needed.

NONSUPERCONDUCTING SAMPLE ($x=0.12$)

The positive magnetoconductivity (negative magnetoresistance) observed for this sample is obviously anisotropic with respect to the direction of magnetic field (see Fig.

3). From the fit of the curves $\sigma_s(B_\perp)$ by the functional form (1) (solid curves in Fig. 3) we have found the inelastic scattering length $L_\varphi = 550$ Å at $T = 1.9$ K and $L_\varphi = 770$ Å at $T = 4.2$ K. For the in-plane diffusion coefficient $D_\parallel = (\pi\hbar^2/me^2)\sigma_s$ we have $D_\parallel = 1.1\,\mathrm{cm}^2/\mathrm{s}$, so that $\tau_\varphi = 5.4\times10^{-11}$ s at $T = 1.9$ K and $\tau_\varphi = 2.7\times10^{-11}$ s at $T = 4.2$ K. These values are of the same order of magnitude as that obtained by Hagen *et al.*[10] for an $x \simeq 0.01$ crystal ($\tau_\varphi = 1.2\times10^{-11}$ s at $T = 1.6$ K), but in contrast to their unusual $\tau_\varphi \sim T^{0.4}$ dependence at $T < 10$ K our data at $T = 1.9$ K and $T = 4.2$ K are compatible with the $\tau_\varphi \sim T^{-1}$ dependence predicted for electron–electron inelastic scattering in a disordered 2D system.[19]

The much weaker negative magnetoresistance for the parallel configuration ($B \| ab$) is quadratic in B up to $B_\parallel = 5.5$ T (see the solid curves in Fig. 3). It is of the same order of magnitude as that of Hagen *et al.*[10] at $T < 5$ K or Kussmaul *et al.*[11] at $T \leqslant 4.2$ K, but we haven't seen any sign of the positive kink at $B = (1-1.5)$ T observed in Ref. 10.

Longitudinal magnetoresistance in a strictly 2D system may be caused only by the influence of the field on the spin degrees of freedom. One of the most obvious causes of negative magnetoresistance is the scattering of electrons on some spin system: the system of Cu spins or partially polarized Nd spins. For any source of spin scattering the field scale for the B^2 dependence ($B \ll B_s, B_s = kT/g\mu_B$) is too low to explain our experimental data. For $g = 2$ one has $B_s = 1.5$ T at $T = 1.9$ K and $B_s = 3$ T at $T = 4.2$ K, but we observe no deviations from a B^2 dependence up to $B = 5.5$ T.

In the standard theory of quantum interference effects in disordered conductors[20,21] there is also an isotropic contribution to the magnetoconductivity from the spin degrees of freedom. When the Zeeman energy of electrons $g_e\mu_B B$ exceeds kT, the magnetic field suppresses the contribution to conductivity originating from the electron–electron interaction and thus leads to a magnetoresistance effect. But this magnetoresistance is always positive and, with the value $g_e = 2$ for the electronic g factor, has the same characteristic field as that for spin scattering: $B = B_s$. Thus it apparently is not related to the effect in question, but it may be the cause of the positive kink on the magnetoresistance curves of Hagen *et al.*[10]

It is very important that in quasi-2D systems with finite thickness $d \ll L_\varphi$ there exists an orbital contribution to the longitudinal magnetoresistance. It is the usual explanation for the parabolic negative magnetoresistance observed in the parallel configuration in semiconducting 2D systems: in GaAs/AlGaAs heterostructures[22] or in silicon inversion layers.[23] The finite-thickness correction to the strictly 2D theory is given by the expression:[24]

$$\Delta\sigma_s(B_\parallel) = \frac{e^2}{\pi h}\ln\left[1 + \left(\frac{B}{B^*}\right)^2\right], \tag{5}$$

where $B^* = \sqrt{3}c\hbar/edL_\varphi$. It is seen from Eq. (5) that $\sigma_s(B_\parallel)$ should be quadratic in B at fields $B \ll B^*$, where the characteristic field $B^* \cong (L_\varphi/d)B_\varphi \gg B_\varphi$.

For a preliminary estimation of B^* let us assume that $d < c$ ($c = 6$ Å is the distance between adjacent CuO_2 planes); then we have $B^* > 25$ T at $T = 1.9$ K and $B^* > 35$ T at $T = 4.2$ K. Thus we think (as do Kussmaul *et al.*[11]) that the finite-thickness correction to the 2D weak localization effect can reasonably explain the observed negative magnetoresistance for the parallel configuration. In the parallel configuration there also exists a

finite-thickness correction to the basic effect in a perpendicular magnetic field (see p. 109 of Ref. 20). We believe that it is just the cause of the upturn of the experimental points for $\sigma_s(B_\perp)$ at $B>(3.5–4)$ T in Fig. 3. By fitting the theoretical expression (5) to the curves for $\sigma_s(B_\parallel)$ and taking into account the values of L_φ obtained earlier, we have found for the effective thickness of a conducting CuO_2 layer $d=(1.5\pm 0.5)$ Å.

The value of d gives an estimate for the dimension of the electron wave function in the direction normal to a CuO_2 plane and ensures the condition of strong carrier confinement: $d<c$. It is in accordance with the proposed highly 2D character of the actual electron band of the $pd\sigma$ type with almost no dispersion along the c axis.[1] The x-ray investigations also show that the electron density is concentrated within the limits of ± 1 Å above and below a Cu atom in the c direction.[25] Single-crystal NdCeCuO may therefore be regarded as multi-quantum-well system (1.5 Å wells and 4.5 Å barriers) or as an analog of a multilayered heterostructure. A theoretical description of high-T_c superconductors as heterostructures has recently been proposed.[26]

As the 2D version of weak localization theory is able to describe the behavior of $\sigma_s(B,T)$ in our sample, the inequality $\tau_{\rm esc}>\tau_\varphi$ should be valid for the escape time of electron from one CuO_2 plane to another. The escape time between adjacent quantum wells in multilayered heterostructures can be estimated from the value of the normal diffusion constant, $\tau_{\rm esc}=c^2/D_\perp$. For our sample we have the anisotropy factor $D_\parallel/D_\perp \cong 10^4$ and $D_\parallel=0.8\,{\rm cm}^2\cdot{\rm s}^{-1}$ at 300 K. Then $\tau_{esc}\cong 4\times 10^{-11}$ s even at room temperature, so that the condition $\tau_{\rm esc}>\tau_\varphi$ may really be fulfilled at low temperatures.

This research is supported by the Russian Program ''Topical Problems of Condensed Matter Physics,'' Grant 98004.

[1] S. Massidda, N. Hamada, J. Yu *et al.*, Physica C **157**, 571 (1989).
[2] Z. Z. Wang, T. R. Chien, N. R. Ong *et al.*, Phys. Rev. B **43**, 3020 (1991).
[3] A. I. Ponomarev, V. I. Tsidilkovski, K. R. Krylov *et al.*, J. Supercond. **9**, 27 (1996).
[4] T. Ito, H. Takagi, S. Ishibashi *et al.*, Nature (London) **350**, 596 (1991).
[5] P. A. Lee and T. V. Ramakrishnan, Rev. Mod. Phys. **57**, 287 (1985).
[6] T. W. Jing, N. P. Ong, T. V. Ramakrishnan *et al.*, Phys. Rev. Lett. **67**, 761 (1991).
[7] K. Schlenga, H. Bach, and K. Westerholt, Physica C **221**, 161 (1994).
[8] K. Karpinska, A. Malinowski, M. Z. Cieplak *et al.*, Phys. Rev. Lett. **77**, 3033 (1996).
[9] Y. Hidaka, Y. Tajima, K. Sugiama *et al.*, J. Phys. Soc. Jpn. **60**, 1185 (1991).
[10] S. J. Hagen, X. Q. Xu, W. Jiang *et al.*, Phys. Rev. B **45**, 515 (1992).
[11] A. Kussmaul, J. S. Moodera, P. M. Tedrow *et al.*, Physica C **177**, 415 (1991).
[12] S. Tanda, M. Honma and T. Nakayama, Phys. Rev. B **43**, 8725 (1991).
[13] G. I. Harus, A. N. Ignatenkov, N. K. Lerinman *et al.*, JETP Lett. **64**, 444 (1996).
[14] A. A. Ivanov, S. G. Galkin, A. V. Kuznetsov, and A. P. Menushenkov, Physica C **180**, 69 (1991).
[15] S. Hikami, A. Larkin, and Y. Nagaoka, Prog. Theor. Phys. **63**, 707 (1980).
[16] B. L. Altshuler, A. G. Aronov, A. P. Larkin, and D. E. Khmelnitskiĭ, Zh. Éksp. Teor. Fiz. **81**, 768 (1981) [Sov. Phys. JETP **54**, 411 (1981)].
[17] B. Shinozaki, H. Fujiki, T. Kawaguti *et al.*, Physica C **273**, 1 (1996).
[18] Y. Hidaka and M. Suzuki, Nature (London) **338**, 635 (1989).
[19] B. L. Altshuler, A. G. Aronov, and D. E. Khmel'nitskii, J. Phys. C: Solid State Phys. **15**, 7367 (1982).
[20] B. L. Altshuler and A. G. Aronov, in *Electron-Electron Interactions in Disordered Systems*, edited by A. L. Efros and M. Pollak, Elsevier Science Publishers, B. V., 1985, p. 4.
[21] P. A. Lee and T. V. Ramakrishnan, Phys. Rev. B **26**, 4009 (1982).
[22] H. Zheng and H. Zhou, Phys. Rev. B **41**, 1140 (1990).
[23] P. M. Mensz and R. G. Wheeler, Phys. Rev. B **35**, 2844 (1987).

[24] B. L. Altshuler and A. G. Aronov, JETP Lett. **33**, 499 (1981).
[25] I. P. Makarova and K. V. Gamayunov, Kristallografiya **43**, 197 (1998) [Crystallogr. Rep. **43**, 163 (1998)].
[26] V. V. Kapaev and Yu. V. Kopaev, *XXXI Conference on Low-Temperature Physics*, Moscow, 1998.

Published in English in the original Russian journal. Edited by Steve Torstveit.